

**DESIGN AND EVALUATION OF AN ACTIVE YAW AND TURBULENCE  
GENERATION SYSTEM TO PRODUCE UNSTEADY FLOW IN AUTOMOTIVE WIND  
TUNNELS**

GERMIEL A. CACHO

A THESIS SUBMITTED TO THE FACULTY OF GRADUATE STUDIES  
IN PARTIAL FULFILMENT OF THE REQUIREMENTS  
FOR THE DEGREE OF

MASTER OF APPLIED SCIENCE

GRADUATE PROGRAM IN MECHANICAL ENGINEERING  
YORK UNIVERSITY  
TORONTO, ONTARIO  
FEBRUARY 2023

## Abstract

This thesis summarizes the research, development, and testing of a novel unsteady yaw and turbulence generation system (TGS) for automotive wind tunnels that replicates on-road conditions using three combined subsystems. The focus of this thesis is primarily on one of the TGS subsystems, the unsteady yaw generation subsystem, which was made up of an airfoil-flap cascade. Tests were conducted in a 1/10th scale, 3/4 open-jet, wind tunnel and velocity data were obtained using two-component hotwire anemometry measurements that were spatially averaged. Yaw performance under different operating conditions, such as flap oscillation frequency and amplitude, was evaluated in terms of the phase-averaged flow behavior, the shape of the yaw angle distribution, and spectral distribution of velocity fluctuations. It is shown that the active yaw subsystem can generate bespoke yaw angle distributions. For example, the generated flows can mirror a variety of on-road flow conditions including the effect of traffic and vehicle wakes at highway speeds. The active system can also input a range of low frequency scales into the flow that are typical of those observed on-road. Preliminary tests indicate that the active yaw subsystem can operate in parallel with gust and turbulence subsystems to enhance flow spectrum designed to model on-road flows, however, future research is required to further optimize the TGS performance.

## Acknowledgements

I would like to express my sincere gratitude to my supervisor, Professor Ronald Hanson, for his guidance and support throughout this project. His expertise and insights were invaluable for the completion of this work. I am also grateful to David Van Every and Peter Waudby-Smith from Aiolos Engineering Corp., who donated the wind tunnel and provided me with helpful feedback. Their insights were very helpful for improving the quality of my research. I would also like to thank all the members of the FMFC laboratory for their assistance and friendship during my time in the lab. They made the research environment enjoyable and offer their help whenever they could. Finally, I would like to thank my friends and family for their constant support and always being there for me when I needed them.

# Table of Contents

<b>Abstract</b>	<b>ii</b>
<b>Acknowledgements</b>	<b>iii</b>
<b>Table of Contents</b>	<b>iv</b>
<b>List of Tables</b>	<b>viii</b>
<b>List of Figures</b>	<b>ix</b>
<b>1 Introduction</b>	<b>1</b>
<b>2 Literature Review</b>	<b>4</b>
2.1 On-Road Flow Conditions . . . . .	4
2.2 Turbulence Generation Systems . . . . .	10
<b>3 Conceptual Design and Analysis</b>	<b>15</b>
3.1 System Objectives and System Specifications . . . . .	15
3.1.1 Objectives . . . . .	15
3.1.2 Requirements . . . . .	16
3.2 Conceptual Design . . . . .	17
3.3 Theory and System Modeling . . . . .	18
3.3.1 Airfoil Wakes . . . . .	18

3.3.2	Flow Yaw . . . . .	19
3.3.3	System Blockage . . . . .	20
3.3.4	Baseline Model . . . . .	20
3.4	Simulations . . . . .	21
3.4.1	Setup and Results . . . . .	21
3.4.2	Mesh Refinement . . . . .	23
3.4.3	Additional Simulation Considerations . . . . .	24
3.5	Yaw System Specifications . . . . .	25
3.6	Motor Selection and Testing . . . . .	26
3.6.1	Motor Selection . . . . .	26
3.6.2	Motor Movement Cases . . . . .	27
3.6.3	Motor Testing . . . . .	28
<b>4</b>	<b>Mechanical and Electrical/Software Design</b>	<b>31</b>
4.1	TGS Mechanical Assembly and Installation . . . . .	31
4.1.1	Fixed Airfoil Body . . . . .	32
4.1.2	Airfoil Flaps . . . . .	33
4.2	TGS Electrical and Software Design . . . . .	33
4.2.1	Communication and Power . . . . .	33
4.2.2	Motor Control . . . . .	34
4.2.3	System/Software Limits, Motor I/O and the Encoder . . . . .	36
<b>5</b>	<b>Experimental Setup and Methods</b>	<b>38</b>
5.1	Wind Tunnel . . . . .	38
5.2	Coordinate System . . . . .	39
5.3	Measurement Equipment . . . . .	39
5.3.1	Temperature Probe . . . . .	40

5.3.2	Differential Pressure Probe . . . . .	40
5.3.3	Hot-wire Anemometry . . . . .	40
5.3.4	Data Acquisition System (DAQ) . . . . .	41
5.4	Traverse System . . . . .	42
5.4.1	Assembly . . . . .	42
5.4.2	Control . . . . .	43
5.5	Control System and Program Flow . . . . .	44
5.5.1	Overview . . . . .	44
5.5.2	Run Preparation . . . . .	44
5.5.3	Calibration . . . . .	45
5.5.4	Conducting Measurements . . . . .	46
5.5.5	Data Conversion and Drift . . . . .	46
5.6	Measurement Positions . . . . .	47
5.7	Baseline and Test Parameters . . . . .	49
5.8	Test Cases . . . . .	50
5.9	Analysis Methods and Notes . . . . .	51
5.9.1	Time Series and Time-Averaging . . . . .	51
5.9.2	Shape of Yaw Distributions . . . . .	52
5.9.3	Phase-Averaging . . . . .	53
5.9.4	Spectra . . . . .	56
5.10	Measurement Uncertainties . . . . .	56
5.10.1	Cross-Wire Measurement Uncertainty . . . . .	56
5.10.2	Phase-Averaging Uncertainty . . . . .	58
<b>6</b>	<b>Results and Discussion</b>	<b>59</b>
6.1	Test Parameter Validation . . . . .	59

6.1.1	Sampling Time Validation . . . . .	59
6.1.2	6-Point Measurement Validation . . . . .	61
6.2	Static Yaw Performance . . . . .	63
6.3	Dynamic Simultaneous Yaw Performance . . . . .	64
6.3.1	Static, Dynamic and Simulation Oscillation Comparisons . . . . .	65
6.3.2	Effect of Oscillation Amplitude . . . . .	66
6.3.3	Effect of Oscillation Frequency . . . . .	69
6.3.4	Effect of Freestream Velocity . . . . .	71
6.3.5	Effect of Special Oscillation Cases . . . . .	73
6.3.6	Effect of the Active Grid . . . . .	76
6.3.7	Frequency Scanning . . . . .	81
6.4	Summary of Results . . . . .	83
6.5	Comparison to On-Road Measurements . . . . .	86
<b>7</b>	<b>Conclusions and Recommendations</b>	<b>91</b>
7.1	Conclusions . . . . .	91
7.2	Recommendations . . . . .	92
	<b>Bibliography</b>	<b>93</b>
<b>A</b>	<b>Assessment of Effects on Turning Vane Performance</b>	<b>97</b>
<b>B</b>	<b>Select Mechanical Diagrams</b>	<b>102</b>
<b>C</b>	<b>Select Electrical Diagrams</b>	<b>103</b>
<b>D</b>	<b>Select Codes</b>	<b>105</b>

## List of Tables

2.1	A summary of on-road flow conditions including turbulence intensity, length scales and yaw angles for three specification ranges (low, medium and high TGS capability). . . . .	9
2.2	Summary of existing TGS in literature. . . . .	10
3.1	Summary of recommended performance specifications based on results summarized in Table 2.1 [1]. <i>TI and TLS values represent streamwise (<math>u</math>), spanwise (<math>v</math>) and vertical (<math>w</math>) components respectively.</i> . . . . .	16
3.2	Overview of the various airfoil configurations and details pertaining to the simulations. . . . .	23
3.3	Summary of the mesh refinement study results. . . . .	23
3.4	Chosen yaw system and airfoil (AF) specifications. . . . .	25
4.1	Motor control parameters . . . . .	35
4.2	Q-Program descriptions. . . . .	36
5.1	DAQ Input Descriptions . . . . .	41
5.2	Baseline testing parameters . . . . .	49
5.3	Summary of test cases. . . . .	51
6.1	Summary of results. . . . .	83
D.1	Description of internal motor registers used for Q-programs. . . . .	108
D.2	Full breakdown of Q-Program 1. . . . .	109

## List of Figures

1.1	Visualization of a simulated unsteady flow occurring over a vehicle on the road [2]. Reproduced or adapted from Ref. [2] with permission. . . . .	1
1.2	Example of steady flow wind tunnel testing on a vehicle [3]. . . . .	2
2.1	Diagram of multi-hole probe array attached to a vehicle for obtaining on-road flow data [4]. Reproduced or adapted from Ref. [4] with permission. . . . .	4
2.2	Range of turbulence intensity and length scale data collected from on-road measurements in different terrain conditions [4]. Reproduced or adapted from Ref. [4] with permission. . . . .	6
2.3	Turbulence intensity and length scale data collected behind a leading vehicle at different distances [5]. Reproduced or adapted from Ref. [5] with permission. . . . .	6
2.4	Diagram of on-road flow yaw for a vehicle traveling at ( $V_{car}$ ), showing the instantaneous vectors for wind velocity ( $V_{wind}$ ), car velocity ( $V_{wind,car}$ ), the angle between ( $\beta$ ) and the resultant vector ( $V_{wind,total}$ ) experienced. . . . .	7
2.5	Typical yaw distribution measured from on-road measurements [6]. Reproduced or adapted from Ref. [6] with permission. . . . .	7
2.6	Different yaw distributions taken at different traffic densities [5]. Reproduced or adapted from Ref. [5] with permission. . . . .	7
2.7	Different yaw distributions taken at different trailing distances [5]. Reproduced or adapted from Ref. [5] with permission. . . . .	8

2.8	Power spectra (u-component) taken at different traffic densities. “Wake” refers to an area directly behind a leading vehicle [7]. Reproduced or adapted from Ref. [7] with permission. . . . .	9
2.9	Range of $u$ and $v$ power spectra at a combination of driving terrains (smooth, RSO, highway) [4]. Reproduced or adapted from Ref. [4] with permission. . . . .	9
2.10	NRC Road Turbulence System (RTS) with passive bars for turbulence generation [8]. Reproduced or adapted from Ref. [8] with permission. . . . .	11
2.11	Pininnfarina TGS nozzle and vortex generators [9]. Reproduced or adapted from Ref. [9] with permission. . . . .	11
2.12	Power spectra comparisons of different existing TGS and collected on-road data [8]. Reproduced or adapted from Ref. [8] with permission. . . . .	12
2.13	Picture of the Toyota NWG [10]. Reproduced or adapted from Ref. [10] with permission. . . . .	13
2.14	3D model of the FKFS Swing [6]. Reproduced or adapted from Ref. [6] with permission. . . . .	13
2.15	Model of the FKFS Active Flaps showing the passive bars (green) and the active airfoil cascade (red) [11]. Reproduced or adapted from Ref. [11] with permission. . . . .	13
2.16	Schematic of the Honda TGS design [12]. . . . .	13
3.1	Miniature TGS used as a proof of concept. . . . .	17
3.2	Centerline ( $U_c$ ) and the freestream velocity ( $U_e$ ) of an airfoil wake at zero angle of attack. . . . .	18
3.3	Dimensional diagram of the fixed airfoil (blue) and flap (red). The diagram above shows a single airfoil only. . . . .	19
3.4	Split airfoil (blue, chord $c_s$ ) and flat plate extension (red, length $x$ ). . . . .	20
3.5	Top view of the simulation domain with simulation setup labels. Data is taken at 5 chord lengths ( $c$ ) away (x-direction, dashed black line) and at the core of the flow (red line). . . . .	21
3.6	Isometric view of the simulation domain. . . . .	22

3.7	3D airfoil cascade (top) and airfoil (bottom) model used for the simulations. The TGS CAD model does not include the active grid between the airfoils and uses a simplified airfoil body model with a truncated trailing edge. . . . .	25
3.8	Final TGS assembled and installed in the test section (top) and the 3D airfoil model (bottom) used for the experiments. The physical TGS model includes the active grid (black elements and shafts) between the airfoils. . . . .	25
3.9	Motor spring and mass testing assembly with an encoder shown on top. . . . .	29
3.10	Equivalent MOI test mass (left) and the 4x MOI test mass (right). . . . .	30
3.11	Schematic diagram of motor spring assembly. The springs replicated torques acting on the flap during the planned experiments ( $\tau_{flow} = \tau_{spring} = kr^2\theta$ ). . . . .	30
4.1	TGS assembly prior to wind tunnel installation. . . . .	31
4.2	Close up view of the fixed airfoils and active grid elements. . . . .	31
4.3	Yaw system fixed airfoil bodies during assembly (final, full-sized). A full airfoil assembly (fixed body, flap, flap support) is shown at the bottom. . . . .	32
4.4	Prototype (early mini design) airfoil assembly with labeled parts. . . . .	32
4.5	TGS motor power and COM lines. . . . .	34
4.6	Example Q-Program (QP1) within the motor memory. . . . .	36
4.7	Example MPS parameter matrix. . . . .	36
4.8	Motor limit switches and cams. . . . .	37
5.1	TGS installed onto the wind tunnel nozzle. . . . .	38
5.2	Coordinate system shown on the installed TGS. . . . .	39
5.3	Coordinate system shown on the wind tunnel CAD model. . . . .	39
5.4	Pitot static tube and the cross-wire probe assembled onto the traverse. . . . .	40
5.5	Dantec Streamline Pro used for setting up and conducting hotwire measurements. . . . .	41
5.6	National Instruments data acquisition system used for data collection. . . . .	41

5.7	Traverse system installed inside the wind tunnel test section. Traverse labels are shown. . . .	42
5.8	Measurement program steps. . . . .	44
5.9	(a) Example flow velocity (magnitude) calibration surface. (b) Example flow yaw ( $\beta$ ) calibration surface. The black dots represent the data collected at all set probe angles and freestream velocities. The surface resolution is reduced in this image for clarity. . . . .	46
5.10	Front view of the TGS nozzle area with a to-scale vehicle for reference. . . . .	48
5.11	Zoomed in view of the vehicle with color coded measurement ranges. . . . .	48
5.12	6-points superimposed between a pair of airfoils. Symmetric pairs (across the middle vertical in Fig. 5.11) are color coded (Outer - red, Inner - black, Middle - green). . . . .	48
5.13	Depiction of flow yaw distributions with different standard deviation values and a constant kurtosis value of $K = 3$ . . . . .	53
5.14	Depiction of flow yaw distributions with different kurtosis values and a constant standard deviation value of $\sigma = 2.5$ . . . . .	53
5.15	Depiction of a raw time series (2 cycles) from an oscillating yaw case. A red line shows where data is cut (zero-crossing) for phase-averaging. The individual cycles are stacked to perform phase-averaging. . . . .	54
5.16	Depiction of phase-averaged data over a single phase. The black line represents the phase-average of the stacked time series data shown in gray. The red dots represent windowed phase-averaging data at discrete points. . . . .	54
5.17	Phase-averaged flow angle data with (red) and without (black) cross-correlation shifting compared to the reference phase provided by the encoder. . . . .	55
6.1	Baseline oscillation (MP2, sinusoidal flap oscillation at 1 Hz and $\pm 10^\circ$ ) plots taken at different sampling times from 30 to 150 seconds as shown in the legend. The results shown are the spatially averaged using 6 points and with a freestream velocity of $U = 15$ m/s. . . . .	60

6.2	The error due to taking an average over cycles shown with baseline oscillation case (MP2, sinusoidal flap oscillation at 1 Hz and $\pm 10^\circ$ ) taken at different sampling times. The equation of the fit is also provided. . . . .	61
6.3	Contour plot of the phase-averaged flow angle, $\beta$ , at the LR measurement plane (black dots) located at $X = 250$ mm from the grid. The baseline yaw oscillation case (MP2, sinusoidal flap oscillation at 1 Hz and $\pm 10^\circ$ ) and a freestream velocity of $U = 15$ m/s was tested. An instantaneous flap angle of $10^\circ$ is shown in this figure. . . . .	62
6.4	Comparison of the flow angle, $\beta$ , versus the phase of the turning vanes for the 6-point and LR/HR reference plane measurement point configurations. All configurations use a baseline oscillation case (MP2, sinusoidal flap oscillation at 1 Hz and $\pm 10^\circ$ ) with a freestream velocity of $U = 15$ m/s. . . . .	63
6.5	Comparison of the flow angle, $\beta$ , and flap angle, $\phi$ , for the static simulations and the experimental static test cases. . . . .	63
6.6	Variation of the measured flow angle with respect to the yaw system flap angle. The dashed line shows the result from the simulation. Data markers show the results from the static experiment and one representative experiment having oscillating yaw (sinusoidal flap oscillation at 1 Hz and $\pm 10^\circ$ ). . . . .	65
6.7	Selected sinusoidal flap oscillation amplitude cases ( $\phi = \pm 5^\circ, \pm 10^\circ, \pm 15^\circ$ ) at $f = 1$ Hz. Subfigures are explained in the text of the corresponding section. . . . .	68
6.8	Selected sinusoidal flap oscillation frequency cases ( $f = 0.5, 1, 5, 10, 15$ Hz) at $\phi = \pm 10^\circ$ . Subfigures are explained in the text of the corresponding section. . . . .	70
6.9	Selected freestream velocity cases ( $U = 12.5, 15, 17.5$ m/s) at $f = 1$ Hz and $\phi = \pm 10^\circ$ . Subfigures are explained in the text of the corresponding section. . . . .	72
6.10	Phase-averaged flap position example for three different oscillation shape cases. . . . .	73
6.11	Spectra of $v'$ normalized by the mean flow velocity $U$ the three different oscillation wave shapes (spectra is shifted vertically by a decade for clarity). . . . .	74

6.12	Selected oscillation shape cases at $f = 1$ Hz and $\phi = \pm 10^\circ$ . Subfigures are explained in the text of the corresponding section. . . . .	75
6.13	Comparison of a combination of yaw, gusting and active grid cases at $U = 15$ m/s. The subfigures and operating parameters are explained in the text of the corresponding section. . . . .	78
6.14	Selected flap frequency cases ( $f = 0.5, 1, 5, 10$ Hz) at $\phi = \pm 10^\circ$ with the gusting and active grid system. Subfigures are explained in the text of the corresponding section. . . . .	79
6.15	Selected gusting frequency cases ( $f = 0.5, 1, 5, 10$ Hz) at $\phi = \pm 10^\circ$ with the yaw and active grid system. Subfigures are explained in the text of the corresponding section. . . . .	80
6.16	Example encoder time series used to show the flap angle as function of time for a frequency scanning test. . . . .	81
6.17	Comparison of a combination of yaw, gusting and active grid cases at $U = 15$ m/s with frequency scanning. The subfigures and operating parameters are explained in the text of the corresponding section. . . . .	82
6.18	Comparison of on-road yaw distributions at different traffic conditions from Jessing et al. [5] and four selected TGS test cases. . . . .	86
6.19	Comparison of on-road yaw distributions at different trailing distances from a leading box truck from Jessing et al. [5] and four selected TGS test cases. . . . .	88
6.20	Comparison of the streamwise power spectra of different systems and on-road traffic from McAuliffe et al. [8] and select TGS test cases. . . . .	89
6.21	Comparison of the TGS and the envelope of on-road flow power spectra at different terrain types from Wordley et al. [4]. . . . .	90
A.1	Red arrows show the location of the fixed vertical active grid shaft elements. . . . .	97
A.2	Close up of the TGS in the fully open position. The fixed vertical active grid elements are shown to be in parallel to the airfoils. These elements remained fixed during the original tests. . . . .	97

A.3	Phase-averaged plots for the vertical grid tracking test compared against the original testing configuration. Comparison with the simulated results are also shown. . . . .	98
A.4	Top view of the airfoil assembly with the gap (approx. 0.5 mm) circled in red. . . . .	98
A.5	Images of tufts at different flap angles without tape across the airfoil gaps. . . . .	99
A.6	Images of tufts at different flap angles with tape across the airfoil gaps. . . . .	100
A.7	Flap versus flow angle plot of flaps held at static flap angles with and without tape over the gaps. . . . .	101
B.1	Mechanical assembly of a single airfoil with important dimensions only. The diagram includes the flap (blue), fixed airfoil body (gray), flap shaft support (red), backplate (brown), 2 airfoil body support/installation threaded rods, 1 flap shaft, and fasteners (threaded inserts and screws). . . . .	102
C.1	General electrical diagrams for a single motor with optional connections. . . . .	103
C.2	Power supply daisy chain diagram. . . . .	104
C.3	Motor power supply and COM line assignments divided by groups. . . . .	104
D.1	Timing diagram of half a motor oscillation cycle. The time subscripts refer to time stopped (S), time accelerating (A), time moving at constant velocity (V) and time decelerating (D) within half a cycle. . . . .	105
D.2	Diagram of the MATLAB and motor interface. MATLAB is used to send angular velocity (VE), deceleration (DE), acceleration (AC) and other commands (timing and positioning) to each motor with addresses 1 to m. Each command is preceded by an address character, $i = 1$ to m, indicating which motor to send the command. Each command is succeeded by its value (i.e. $VE = \omega$ , $DE = AC = \alpha$ ). Each motor contains registers R1 to Rn in which data from MATLAB can be stored. Registers are then used as an input for each Q-Program. . . . .	107

## Abbreviations

**AF** - Airfoil

**DAQ** - Data Acquisition System

**HR** - High Resolution

**LR** - Low Resolution

**MOI** - Moment of Inertia

**MP(S)** - Motor Program (Set)

**PDF** - Probability Density Function

**PIV** - Particle Image Velocimetry

**PSD** - Power Spectral Density

**RMS** - Root Mean Square

**RMSE** - Root Mean Square Error

**RSO** - Road Side Obstacle Terrain

**SO** - Smooth-Open Road Terrain

**TGS** - Turbulence Generation System

**TI** - Turbulence Intensity

**TLS** - Turbulence Length Scale

## Symbols

$B$  - Nozzle blockage

$c$  - Airfoil chord length

$c_s$  - Split airfoil chord length

$f$  - Flap operating frequency

$f_r$  - Reduced frequency

$f_s$  - Flow frequency ( $f_r$ )

$K$  - Distribution kurtosis

$l_a$  - Airfoil body length

$l_f$  - Flap length

$L_r$  - Characteristic car length ( $f_r$ )

$N_i$  - Number of independent samples (error)

$N_{af}$  - Number of airfoils

$P$  - Differential pressure

$P_{atm}$  - Atmospheric pressure

$rps$  - Revolutions per second

$R$  - Gas constant

$R_a$  - Airfoil body length relative to chord

$R_f$  - Airfoil flap length relative to chord

$s$  - Airfoil spacing

$t_{af}$  - Airfoil thickness

$T$  - Temperature

$TI_i$  - Turbulence intensity ( $i = u, v, w$ )

$TLS_i$  - Turbulence length scale ( $i = u, v, w$ )

$u$  - Streamwise flow velocity component

$\bar{u}$ - Streamwise mean velocity	$W$ - Wind tunnel nozzle width
$u'$ - Streamwise velocity fluctuations	$z$ - Z-factor (error)
$u'_{rms}$ - RMS of Streamwise velocity fluctuations	
$U$ - Flow velocity magnitude	$\beta$ - Flow yaw angle
$U_c$ - Wake centerline velocity	$\delta\beta_i$ - Flow yaw error
$U_e$ - Wake edge velocity	$\phi$ - Flap angle
$U_r$ - Reference freestream velocity ( $f_r$ )	$\phi_A$ - Flap amplitude
$v$ - Spanwise flow velocity component	$\phi_{max}$ - Maximum flap range
$\bar{v}$ - Spanwise mean velocity	$\rho$ - Fluid Density
$v'$ - Spanwise velocity fluctuations	$\sigma_i$ - Standard Deviation
$v'_{rms}$ - RMS of spanwise velocity fluctuations	
$w$ - Vertical flow velocity component	

# 1 Introduction

Vehicles driven on the road are subjected to a wide range of complex oncoming flow behavior. The complex flow is often subdivided into three main classifications: broadband turbulent flow, unsteady or gusting flow, and time varying flow yaw. Previous on-road measurements have shown that the composition or nature of the flow experienced by a vehicle traveling on the road depends on a variety of environmental conditions, such as wind intensity, direction, weather conditions, traffic density, road terrain or even types of the surrounding vehicles [4, 5, 7, 13]. For demonstration, one example of a simulated turbulent flow over a vehicle by Duncan et al. [2] is shown in Fig. 1.1. Aerodynamic and aeroacoustics performance measures of vehicles have been shown to depend on effects such as turbulence, shown in Fig. 1.1, unsteady flow fluctuations and yaw [2, 10, 13, 14, 15]. Replicating realistic on-road conditions in controlled wind tunnel tests is important to provide realistic testing for vehicle development.

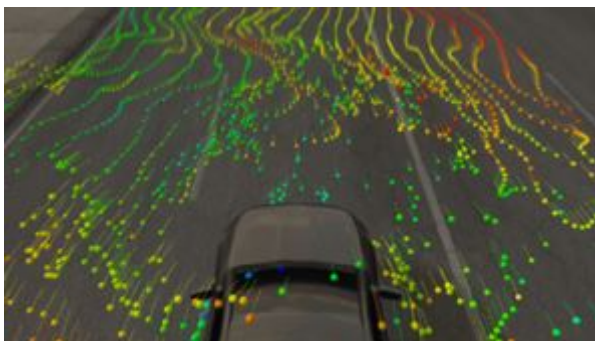


Figure 1.1: Visualization of a simulated unsteady flow occurring over a vehicle on the road [2]. Reproduced or adapted from Ref. [2] with permission.

Differences between traditional wind tunnel testing and on-road flow conditions have been observed in literature. Traditional automotive wind tunnels are typically used to model a vehicle passing through a low turbulence environment or with some mild cross flow achieved by rotating the vehicle in the test section [16]. In general, vehicles were tested in steady flow wind tunnels, as shown in Fig. 1.2, to obtain controlled and

repeatable results due to the unpredictability and unreliability of on-road testing [17]. However, this type of wind tunnel testing is heavily in contrast to the unsteady on-road flow behaviors as discussed previously. As such, current wind tunnels do not replicate the turbulent and unsteady on-road flow conditions making it difficult to optimize vehicles for real world driving environments.

Attempts to replicate on-road flow in controlled wind tunnel tests have resulted in novel turbulence generation systems (TGS). The term, TGS, is often used as a blanket term that can be used to describe any system that generates unsteady flows, such as broadband turbulence and yaw, in a wind tunnel.



Generally, such systems aim to generate a wide and controllable range of unsteady flow behaviors within

Figure 1.2: Example of steady flow wind tunnel testing on a vehicle [3].

the test section of the wind tunnel. Many unsteady turbulence and yaw generation methods have been discussed in previous literature. In many fields, including automotive engineering, wind engineering or turbomachinery, it is possible to generate appropriate flow scales using grids, bluff body arrays or airfoil cascades upstream of the wind tunnel test section. While there are numerous examples of passive and active turbulence or yawed flow generation, replicating the complete range of flow scales occurring on the road remains an open and challenging task. Replicating the range of naturally occurring on-road flow conditions in the wind tunnel is thought to translate into impacts spanning improved automobile aerodynamics (for performance and economy) to driver experience and safety, for traditional and autonomously controlled vehicles. Therefore, there is a need to better replicate the range of on road flow conditions in wind tunnels to support testing needed to advance the design of the next generation of vehicles.

The motivation for this research is to better simulate on-road wind conditions in automotive wind tunnels. This will be achieved through the research, development and characterization of a novel unsteady yaw and turbulence generation system. This thesis is focused on a subset of this overarching objective; the primary objective considered within this thesis is to replicate time varying flow yaw experienced by vehicles on the

road within the scaled version of an automotive wind tunnel. However, the yaw system is designed to work as a part of complete system, which includes gust and turbulence generation. As such, this thesis is biased towards the unsteady yaw generation aspect of the system research, development, and testing, but overlaps with some related aspects to the complete system where it was warranted. The objectives of the research are listed below.

1. Determine the functional and performance requirements to replicate on-road conditions through a literature review.
2. Design, construct and validate a physical TGS. This includes it's mechanical, electrical and control system design.
3. Characterize the TGS yaw performance through hotwire and pressure based measurement methods.

The structure of this thesis is as follows. Chapter 2 provides an overview of the related literature followed by Chapter 3 that focuses on the preliminary design of the novel system. Next, discussion of the final physical and operational systems are found in Chapter 4. The experimental methods and procedures are found in Chapter 5. Results and discussion of are found in Chapter 6 followed by the conclusions of this research in Chapter 7.

## 2 Literature Review

In the following chapter, a review of relevant literature related to on-road flow conditions and existing TGS designs is presented. The review supports the establishment of system specifications and conceptual designs of the novel TGS that is later discussed in Chapter 3.

### 2.1 On-Road Flow Conditions

Numerous studies have collected data concerning on-road flow conditions. A common method of obtaining on-road flow measurements is through the use of an array of multi-hole probes fixed to the front of the vehicle as shown in Fig. 2.1 [4, 7]. Other methods of obtaining on-road measurements in literature include hot-wire and sonic anemometry [10, 18]. The test vehicle was usually driven at a reference velocity of 100 km/h in different types of terrain (open roads, roads with roadside obstacles and highway terrains), weather (i.e. winds or gusts) and traffic conditions (light to heavy) [4, 7, 13, 19]. For example, Wordley et al. often characterizes these different road conditions as smooth terrains with completely open roads, road side obstacle (RSO) terrains with light traffic and objects along the sides of the road, such as trees or buildings, and highway terrains with heavy traffic [4]. Other works also consider the flow behaviors of different on-road vehicle maneuvers, such as

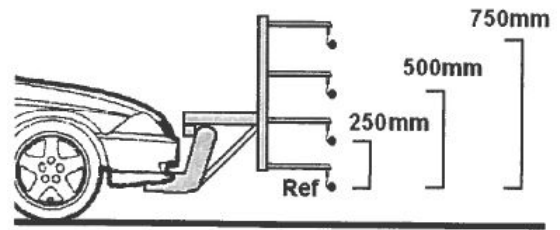


Figure 2.1: Diagram of multi-hole probe array attached to a vehicle for obtaining on-road flow data [4]. Reproduced or adapted from Ref. [4] with permission.

trailing behind or overtaking a leading vehicle [5, 11]. The many factors that affect on-road flow conditions result in a wide range of possible unsteady on-road flow parameters such as turbulence and unsteady flow yaw. To better understand the range of flow conditions and existing parameterizations or ranges used to quantify on-road flows, 12 different papers (believed to be the core available and most commonly cited in the literature) were examined with over 63 distinct data points (parameters and values with associated conditions such as traffic/wind intensity, terrain type and more). Common data points were collected and averaged in a spreadsheet that was omitted for brevity but was used to obtain the conclusions below. Furthermore, the data collected for different on-road conditions are summarized in Table 2.1.

1. **Turbulence Intensity (TI)** - The turbulence intensity is defined by normalizing the rms of flow fluctuations ( $u'_{rms}, v'_{rms}, w'_{rms}$ ) by a reference velocity,  $U$ . Average values for streamwise, lateral and vertical TI ranges from 4 – 7% with a ratio of 1.0, 1.0 and 0.4 - 0.6, respectively, compared to the streamwise TI. The range of values depended on the conditions present on the road. For example, TI values increase significantly when going from smooth/open to RSO to highway terrains, or for conditions with high traffic or intense winds as shown in Fig. 2.2. Additionally, Fig. 2.3 shows extreme TI values of over 20% for trailing and overtaking maneuvers but represent only an extreme point from the data surveyed.

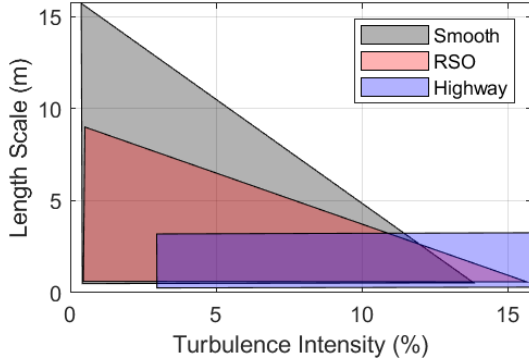


Figure 2.2: Range of turbulence intensity and length scale data collected from on-road measurements in different terrain conditions [4]. Reproduced or adapted from Ref. [4] with permission.

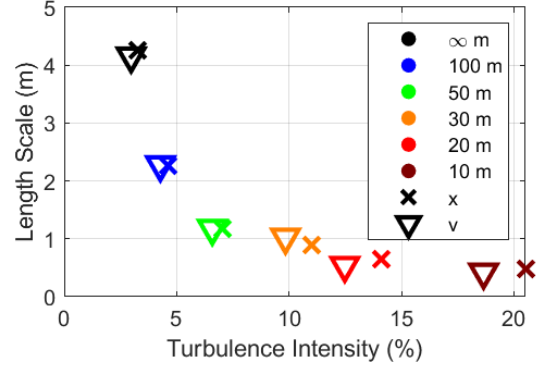


Figure 2.3: Turbulence intensity and length scale data collected behind a leading vehicle at different distances [5]. Reproduced or adapted from Ref. [5] with permission.

2. **Turbulence Length Scales (TLS)** - Average values for streamwise, lateral and vertical TLS ranges from 2 to 5 m with a ratio of 1.0, 1.0 and 0.1 - 0.2, respectively, compared to the streamwise TLS. The largest length scales measured on the road decreases from SO to RSO to HW terrains as shown in Fig. 2.2, or during conditions with high traffic or wind intensity. Trailing vehicles also show significant decreases in turbulent scales as evident in Fig. 2.2 and 2.3.
3. **Flow Yaw** - Flow yaw, as shown by angle  $\beta$  in Fig. 2.4, describes the angle at which the flow goes over a vehicle, considering both the instantaneous unsteady flow velocity fluctuations ( $V_{wind}$ ) and the vehicle velocity ( $V_{wind,car}$ ). Flow yaw was typically observed to follow a normal distribution in which most data is measured to be between  $\beta = \pm 10^\circ$  as shown in Fig. 2.5. However, flow yaw has also been observed to be dependent on the previously discussed on-road factors; traffic intensity (see Fig. 2.6) and the distance to the leading vehicles (see Fig. 2.7) can drastically change the shape of the distribution. For example, high traffic or intense weather conditions often result in yaw distributions with reduced peaks and widened bases. Previous works from Jessing et al. have shown that the standard deviation of measured on-road yaw distributions,  $\sigma$ , range from  $\sigma = 1.9 - 11.1^\circ$  [5].

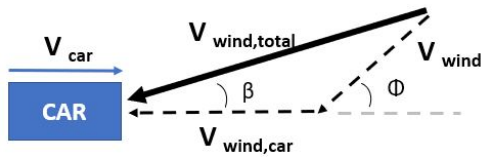


Figure 2.4: Diagram of on-road flow yaw for a vehicle traveling at ( $V_{car}$ ), showing the instantaneous vectors for wind velocity ( $V_{wind}$ ), car velocity ( $V_{wind,car}$ ), the angle between ( $\beta$ ) and the resultant vector ( $V_{wind,total}$ ) experienced.

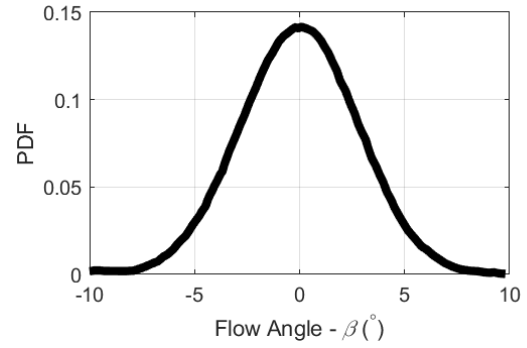


Figure 2.5: Typical yaw distribution measured from on-road measurements [6]. Reproduced or adapted from Ref. [6] with permission.

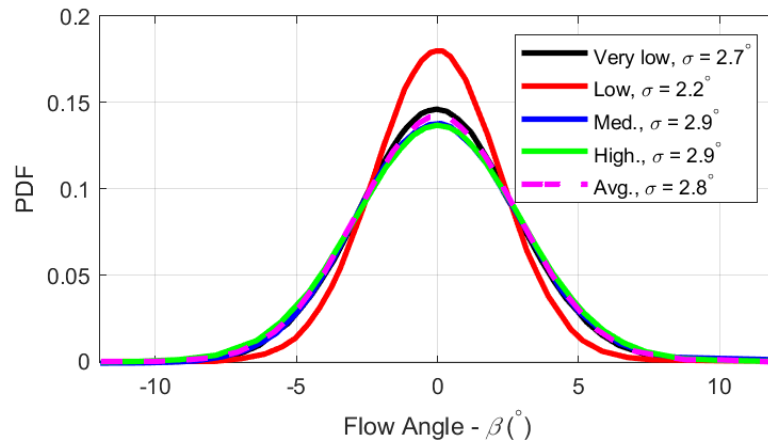


Figure 2.6: Different yaw distributions taken at different traffic densities [5]. Reproduced or adapted from Ref. [5] with permission.

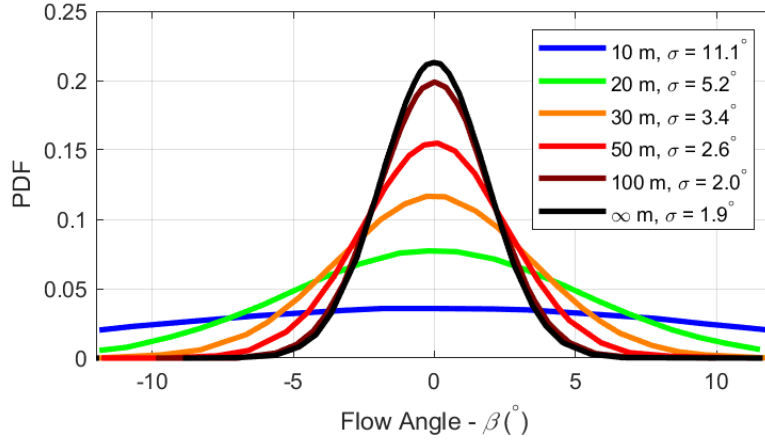


Figure 2.7: Different yaw distributions taken at different trailing distances [5]. Reproduced or adapted from Ref. [5] with permission.

4. **Flow Spectra** - Power spectral data is often plotted with the reduced frequency defined by  $f_r = 2\pi f_s L_r / U_r$ , where  $f_s$  is the flow frequency (Hz),  $L_r$  is the characteristic car length (approx. 4 m) and  $U_r$  is the reference freestream velocity. Reduced frequencies of less than 0.1 can be considered as quasi-steady because the large length scales fully engulf a vehicle in bulk flow yaw [20]. On the other hand, reduced frequencies greater than 1 indicate a fully unsteady flow [20].

An example of a streamwise power spectra, is shown in Fig. 2.8. This figure shows that the resulting power spectra is dependent on environmental factors such as traffic density [7]. In general, increases in turbulent energy are observed for increasing traffic density, terrain roughness or wind speed [4, 7, 18]. A general envelope or range of on-road flow spectra that considers a variety of driving conditions is shown in Fig. 2.9. These plots show that while on-road flow contains a significant portion of energy at lower frequencies (bulk on-road flow), unsteady med-high frequency flow structures have still been observed.

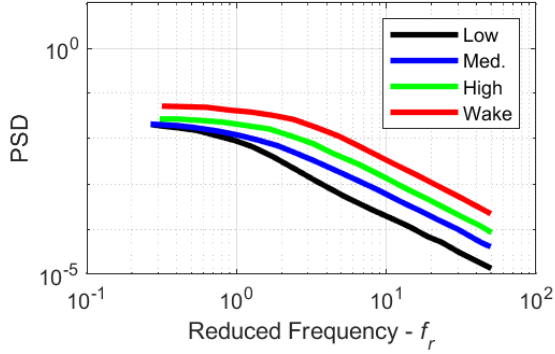


Figure 2.8: Power spectra (u-component) taken at different traffic densities. “Wake” refers to an area directly behind a leading vehicle [7]. Reproduced or adapted from Ref. [7] with permission.

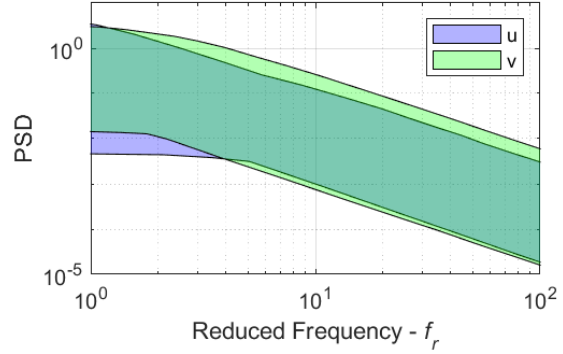


Figure 2.9: Range of  $u$  and  $v$  power spectra at a combination of driving terrains (smooth, RSO, highway) [4]. Reproduced or adapted from Ref. [4] with permission.

Table 2.1: A summary of on-road flow conditions including turbulence intensity, length scales and yaw angles for three specification ranges (low, medium and high TGS capability).

Spec	TI u:v:w (%)	TLS u:v:w (m)	Yaw ( $\pm$ ( $^\circ$ ))	Operating Frequency (Hz)	Description
Low	4:4:2	5:5:0.5	6	5	Smooth open roads with light traffic/wind
Med.	6:6:4	2.5:2.5:0.5	8	10	Low + RSO/highway terrains with moderate wind/traffic
High	9*:9*:7	1:1:0.5	10*	30	Med. + with high wind/traffic + some trailing/overtaking maneuvers

\* *Minimum values—Actual on-road values can significantly exceed these values based on different road conditions*

In addition to these parameters, on-road flow can be generally described to have three main forms of unsteady flow behaviors. First, the presence of unsteady yaw has been observed on the road and tends to generate low frequency spanwise turbulence. Secondly, low frequency streamwise turbulence, or gusting, was also observed during the on-road measurements. Finally, on-road flow was shown to contain turbulent

energy at medium to higher frequencies. Therefore, these three behaviors guide functional and performance requirements for a TGS design.

## 2.2 Turbulence Generation Systems

Several existing TGS designs have been examined in this review. As discussed previously, the main function of TGS is to replicate the unsteady flow behavior inside automotive wind tunnel test sections. To achieve this, existing TGS designs utilize certain configurations or methods that produce varying levels of turbulence generation. The configurations and methods will be discussed in the following section. A brief summary of existing TGS designs considered are given in Table 2.2.

Table 2.2: Summary of existing TGS in literature.

<b>TGS</b>	<b>Description/Methods</b>
<b>NRC TGS (RTS)</b>	Passive bars (bluff body) are used to generate turbulence.
<b>Pininfarina TGS</b>	Turbulence generation is generated with active spires (bluff body) while unsteady bulk yaw is achieved through separate vehicle turntable.
<b>FKFS Swing</b>	Turbulence generation and unsteady yaw is achieved through an active airfoil cascade.
<b>FKFS Active Flaps</b>	Turbulence generation and unsteady yaw are primarily generated using an airfoil cascade equipped with actively controlled trailing edge flaps. Additional turbulence is generated using a set of passive bars separate from the airfoil cascade.
<b>Toyota NWG</b>	Turbulence generation and unsteady yaw are primarily achieved using an active airfoil cascade. Additional turbulence is generated using dampers across the top of the nozzle. The dampers modify the opening area of the nozzle to create streamwise pulsations.
<b>Honda TGS</b>	Unsteady flow yaw is generated using 2 large active airfoils at the sides of the nozzle. Meanwhile, turbulence generation is primarily achieved through active spires inside the nozzle. Finally, upwash/downwash flow behaviors found on the road are replicated with active horizontal airfoils.

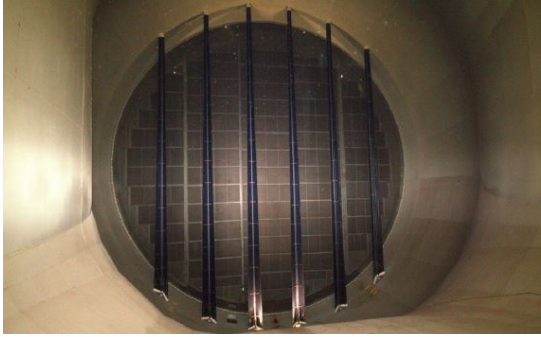


Figure 2.10: NRC Road Turbulence System (RTS) with passive bars for turbulence generation [8]. Reproduced or adapted from Ref. [8] with permission.

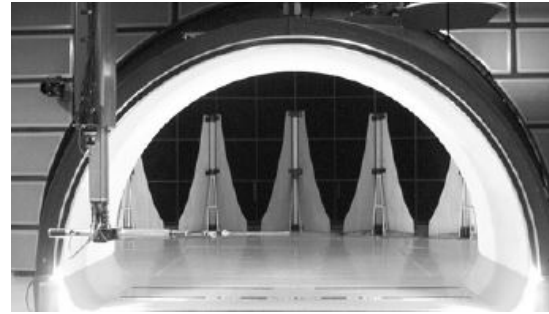


Figure 2.11: Pininnfarina TGS nozzle and vortex generators [9]. Reproduced or adapted from Ref. [9] with permission.

The two methods to create turbulent conditions in a wind tunnel may be classified as either passive or active. Passive methods, as seen in the Canadian National Research Council (NRC) TGS shown in Fig. 2.10, utilize static spires placed within the contraction; these spires widen closer to the ground to create turbulent boundary layers to replicate atmospheric conditions [8]. Passive systems are limited to producing only a small range of turbulent flow scales and are generally unsuitable for replicating large scale unsteady flow events that are known to occur on the road. Still, passive systems are generally inexpensive and simple to manufacture. On the other hand, active TGS systems require moving components, motors and a control system, which results in greater costs and is more challenging to design. However, active TGS systems have potential for a larger range of turbulence generation and unsteady events such as gusts and time varying flow yaw [10, 11]. Accordingly, many of the TGS designs reviewed incorporate active flow elements due to the significant advantages over passive designs.

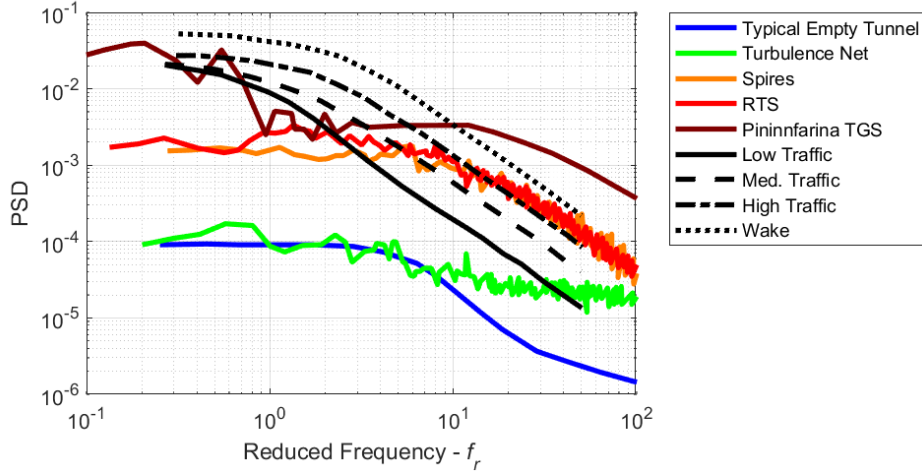


Figure 2.12: Power spectra comparisons of different existing TGS and collected on-road data [8]. Reproduced or adapted from Ref. [8] with permission.

Aside from the active or passive basis, the existing TGS designs rely on two main different methods of turbulence or flow yaw generation mechanisms. First, the use of bluff body or drag based devices have been used in early TGS designs such as the Pininfarina TGS, shown in Fig. 2.11, or the NRC TGS [8, 9]. These devices generate turbulence through high frequency vortex shedding created by vortex generators or bars placed within the contraction. Although these systems produce sufficient high frequency turbulence, they have been shown to lack broadband turbulence and flow yaw as shown in Fig. 2.12. Another method of turbulence generation is the airfoil cascade or lift based TGS designs. An example of this is the Toyota Natural Wind Generator (NWG) shown in Fig. 2.13 [10]. These systems utilize an array of airfoils that can actively steer the flow. They generate a wider range of dynamic and turbulent flow behavior for lower to medium frequencies but lack inputs to replicate streamwise turbulence intensity and length scales. Furthermore, they have also been shown to produce sufficient flow yaw generation performance across all airfoil cascade designs reviewed. Therefore, two main turbulence and yaw generation mechanisms have been described in literature, each with their own advantages and disadvantages.



Figure 2.13: Picture of the Toyota NWG [10]. Reproduced or adapted from Ref. [10] with permission.

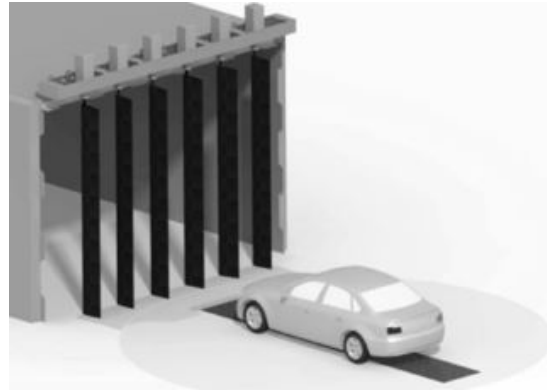


Figure 2.14: 3D model of the FKFS Swing [6]. Reproduced or adapted from Ref. [6] with permission.

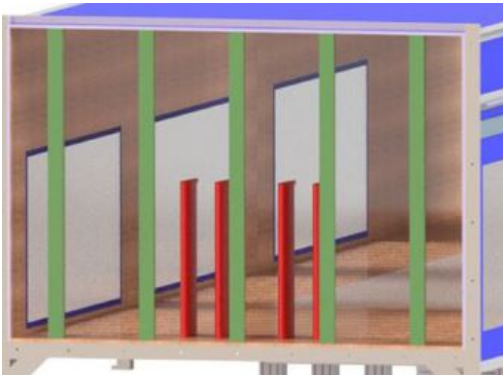


Figure 2.15: Model of the FKFS Active Flaps showing the passive bars (green) and the active airfoil cascade (red) [11]. Reproduced or adapted from Ref. [11] with permission.

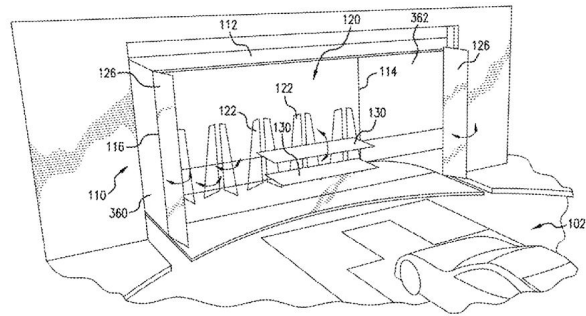


Figure 2.16: Schematic of the Honda TGS design [12].

Modern TGS designs have combined active drag and lift type elements to increase turbulence and flow yaw performance. For example, the Toyota NWG utilizes an active airfoil cascade combined with an active damper system that can dynamically control the nozzle opening area, allowing it to create streamwise pulsations in the flow [10]. As a result, the NWG can produce yaw and spanwise turbulence from the cascade and streamwise turbulence through the active damper system. Another modern TGS system is the FKFS Active Flaps, shown in Fig. 2.15, which utilizes an airfoil cascade combined with a passive

drag based bar system in the contraction [11]. Finally, the Honda TGS, as shown in Fig. 2.16, produces unsteady flow through a combination of systems; however, data from this system is not yet made available. The Honda TGS utilizes three main subsystems including a pair of large active airfoils for flow turning and spanwise turbulence, active vortex generators for bluff body turbulence generation and a large active horizontal airfoil to reproduce upwash and downwash flow behaviors found on the road [12]. Therefore, these systems demonstrate the need for multiple strategies to reproduce the wide range of complex flow behavior known to occur on the road, but in controlled wind tunnel tests.

## 3 Conceptual Design and Analysis

The following chapter overviews the development and analysis of a conceptual model of the TGS. The term, TGS, refers to a combination of mechanical subsystems connected to a single frame. The present work will only address the design and analysis of the unsteady yaw subsystem.

### 3.1 System Objectives and System Specifications

An important first step in the TGS design is the definition of system objectives and requirements. This information is used as a guide and reference to design decisions discussed later in the chapter. It must be noted that the information presented in Section 3.1.1 and 3.1.2 represent the entire TGS system.

#### 3.1.1 Objectives

A set of objectives were defined below and were used as a guide for initial design decisions.

1. **Maximize Flow Yaw Performance:** The main function of the TGS yaw system is to generate sufficient unsteady flow turning to replicate on-road flow conditions with respect to yaw magnitude and frequency. This metric will be measured against the maximum required flow angle that must be achieved based on requirements.
2. **Maximize Turbulence Generation:** Lift-based yaw systems are known to also enhance certain levels of turbulence. Although the yaw system will be combined with another turbulence generating mechanism (in a related parallel project), any additional turbulence is considered beneficial for the project as a whole. Again, this will be measured against turbulence parameter requirements.

3. **Minimize System Losses:** The system should minimize aerodynamic losses when not in use.
4. **Minimize System Cost:** The system cost should be within the allocated budget.
5. **Minimize System Complexity:** The system must be designed such that complexity is minimized to prevent excessive system failure during testing.
6. **Maximize System Manufacturability:** The system must be designed such that manufacturing and repair can be completed without significant difficulty.

### 3.1.2 Requirements

In addition to the objectives defined above, an initial set of system specifications were determined based on the literature review in Section 2.1 and Table 2.1. The required specifications are tabulated below.

Table 3.1: Summary of recommended performance specifications based on results summarized in Table 2.1

[1]. *TI and TLS values represent streamwise ( $u$ ), spanwise ( $v$ ) and vertical ( $w$ ) components respectively.*

TI (% , u:v:w)	TLS (m, u:v:w)	Flow Yaw ( $\pm^\circ$ )	Op. Freq. (Hz)
9 : 9 : 7	1 : 1 : 0.5	10	0.1 - 30

Additionally, there are three main functions that must be achieved by the TGS. The list below describes the functional requirements or subsystems that make up the TGS.

1. **Unsteady Yaw Generation:** Unsteady flow yaw is an important component of on-road flow conditions. As such, the system shall be able to generate a wide range of flow yaw angles over the entire test section.
2. **Streamwise Flow Pulsations (Gusting):** A common gap of existing TGS designs is the ability to generate sufficient streamwise flow variations. Therefore, the TGS must be able to generate these unsteady flow variations inside the wind tunnel.

3. **Broadband Turbulence Generation:** Spectral analysis on existing TGS have shown that current designs are unable to replicate on-road flow spectra; for example, active systems have been shown to lack performance in the mid-high frequency turbulence range. The proposed system must then be able to generate streamwise and spanwise unsteady flow over a broad frequency range (low to high).

### 3.2 Conceptual Design

Modern TGS systems, such as the Toyota NWG, FKFS Active Flaps or Honda TGS, include a combination of different type of active flow elements. Previous works have shown that active airfoil cascades are able to generate sufficient unsteady yaw generation performance at low frequencies. To reduce inertial load, enhance system bandwidth, and reduce control system demand (and cost), an airfoil cascade with fixed airfoil bodies and controllable flaps is considered. The airfoil cascade, however, only considers the unsteady yaw functional requirement; instead, an active grid is used to achieve the gusting and broadband turbulence generation functional requirements. The fixed airfoils of the cascade lends to embedding the active turbulence system for support and simplicity.

The combination of these two systems were visualized through a miniature prototype. The conceptual prototype is shown in Fig. 3.1. The active yaw system consists of fixed vertical airfoils, shown in white, that are each paired with servo controlled flaps at the trailing edge, shown in red. These flaps can be controlled independently or simultaneously to replicate different on-road flow conditions. Other components shown in Fig. 3.1 are the active grid and

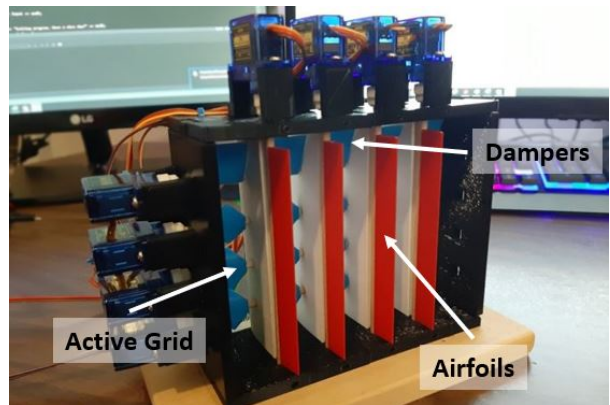


Figure 3.1: Miniature TGS used as a proof of concept.

gusting system, shown in blue, which are used to work alongside the active yaw system by producing extra streamwise turbulence and flow pulsations. The system shown in Fig. 3.1 is not an accurate representation but was used as a proof of concept for the mechanical and electrical systems required. Another important

note to consider is the limited conceptual options and difficulty of combining these three unique subsystems together to achieve all functional requirements. As such, a traditional approach to evaluate different conceptual options was not considered for this design.

### 3.3 Theory and System Modeling

#### 3.3.1 Airfoil Wakes

Analysis was done to promote flow uniformity downstream of the airfoil, which are to be part of the yaw system. Inherently, airfoils create velocity deficits, as shown in Fig. 3.2. In general, the centerline velocity for an isolated symmetrical airfoil wake recovers to around 90% of the freestream velocity at approximately 2 chord lengths [21]. For an airfoil cascade, the wake decays slower compared to an isolated airfoil but recovers to around 70 - 80% of the freestream velocity at 0.5 chord lengths [22]. Accordingly, the distance between the trailing edges of the cascade and the test vehicle was chosen to be 5 chord lengths. This distance would promote flow uniformity at the test vehicle. Given that an automobile is to be placed at 250 mm away from the TGS exit, the target of 5 chord lengths is used to set a desired baseline chord length of the airfoils. It should be noted that this analysis may only be applied to static flap cases. Uncertainties concerning the wake when replicating dynamic unsteady yaw will be tested later in the physical experimental testing with the prototype system.

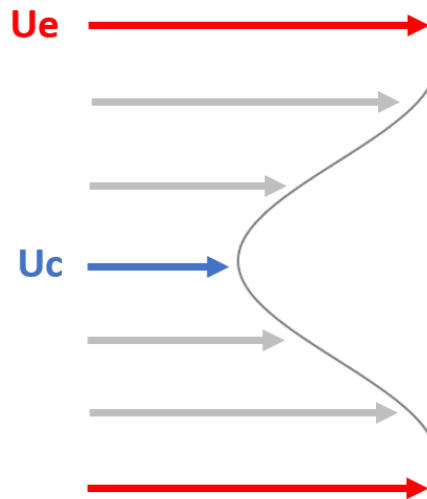


Figure 3.2: Centerline ( $U_c$ ) and the freestream velocity ( $U_e$ ) of an airfoil wake at zero angle of attack.

### 3.3.2 Flow Yaw

To estimate potential flow turning performance of the airfoils, literature concerning compressor blade design was examined. One key variable that effects flow turning performance is the diffusion factor ( $DF$ ). The diffusion factor is proportional to the difference between the maximum flow velocity on the suction side ( $V_{SS}$ ) and the trailing edge ( $V_{TE}$ ) and can be calculated with  $DF = (V_{SS} - V_{TE})/V_{LE}$ , where  $V_{LE}$  is the leading edge velocity [23, 24]; a large diffusion factor indicates that there is a large velocity gradient across the suction surface, leading to the development of an adverse pressure gradient. Therefore, flow turning capabilities are related to the diffusion factor because it provides an indication of flow separation or stall along the suction side, at which flow turning is impeded.

A diffusion factor of less than 0.4 - 0.5 ensures that minimal flow separation occurs on the suction surface of cascade blades, thus being able to turn the flow according to the angle of attack [23, 24]. The diffusion factor can be related to the chord and spacing between each airfoil of a cascade by the following equation given the geometry of the airfoil as shown in Fig. 3.3.

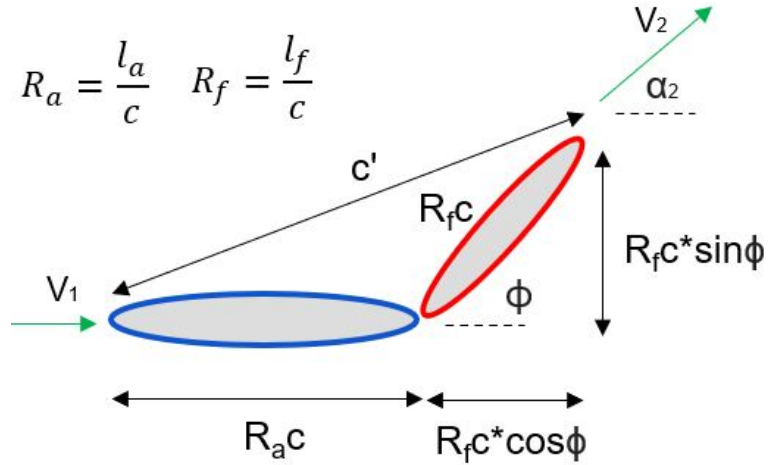


Figure 3.3: Dimensional diagram of the fixed airfoil (blue) and flap (red). The diagram above shows a single airfoil only.

$$s = \frac{2c\sqrt{(R_a + R_f \cos(\phi))^2 + (R_f \sin(\phi))^2}}{\tan(\alpha_2)} \left( DF + \frac{1}{\cos(\alpha_2)} - 1 \right) \quad (3.1)$$

where  $s$  is the spacing between the airfoils,  $c$  is the chord length (related to the effective chord length,  $c'$ ),  $R_a$  is the fixed airfoil length ( $l_a$ ) relative to the chord,  $R_f$  is the flap length ( $l_f$ ) relative to the chord,  $\phi$  is the flap angle,  $\alpha_2$  is the exiting flow angle and  $DF$  is the diffusion factor. The equation can be used to relate the spacing between each airfoil given a chord length and diffusion factor. A maximum diffusion factor of

0.3 was conservatively chosen to minimize possible flow separation.

### 3.3.3 System Blockage

System blockage was minimized to reduce pressure losses during operation. The total blockage caused by the airfoils is given by  $B = N_{af}t_{af}/W$  where  $N_{af}$  is the number of airfoils,  $t_{af}$  is the thickness of the airfoils and  $W$  is the total nozzle width. A NACA profile airfoil is intended to be used similar to the airfoils used in other TGS designs, but modifications were made in order to reduce the system blockage while maintaining the ability to turn the flow. Simply reducing the thick-

ness of a NACA profile airfoil will reduce blockage but will also reduce the chord length which lowers flow turning performance as per Equation 3.1. To

get around this, it was decided to split a thinner NACA airfoil at its maximum thickness and to add

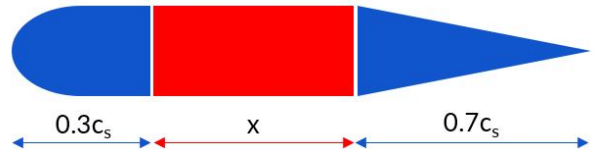


Figure 3.4: Split airfoil (blue, chord  $c_s$ ) and flat plate extension (red, length  $x$ ).

a section of equal thickness between the leading and trailing edges, as shown in Fig. 3.4. This modification ensures that blockage is minimized with the use of thinner airfoils while flow turning performance is conserved by extending the chord. The flat portion of the airfoil will also be used to house other related subsystems in the TGS design (active grid).

### 3.3.4 Baseline Model

A baseline model of the airfoil cascade was established using the concepts discussed above. A cascade of 16 airfoils was chosen with chord lengths of 50 mm for the baseline case. Originally, the spacing between the sidewalls and the adjacent airfoils were half of the cascade spacing ("HALF" in Table 3.2) but was changed to be equal to the cascade spacing later on ("EQ" in Table 3.2). The diffusion factor was also calculated using the chord length and airfoil spacing to verify that it was under 0.3. Each airfoil included a 50% chord trailing edge flap that could move between  $\pm 15^\circ$ .

## 3.4 Simulations

### 3.4.1 Setup and Results

Steady flow simulations were performed using the RANS  $k - \varepsilon$  equations in StarCCM to verify and assess yaw system performance. The governing equations used by this model are based on mass and momentum conservation (continuity and Navier Stokes), and turbulence transport equations (turbulent kinetic energy,  $k$ , and dissipation rate,  $\varepsilon$ ). The baseline airfoil cascade at different flap angles were modeled along with the test section. The simulation setup regions including the velocity inlet, pressure outlet, test section and TGS can be seen in Fig. 3.5 and 3.6. The figures also show the perimeter of the outer walls that bound the flow (contour). Additionally, other walls, such as the nozzle and collector, are shown with light gray shaded areas. The data was collected from the simulation using a line probe, or a line of distinct measurement points, as shown in Fig. 3.5. The line represents an area in front of a vehicle at 5 chord lengths away from the TGS (250 mm) and at the core of the yawed flow. Data was taken at a height of 50 mm off of the floor. A list of simulations conducted are shown in Table 3.2 for static flap angles. Further details of these simulations are omitted for brevity.

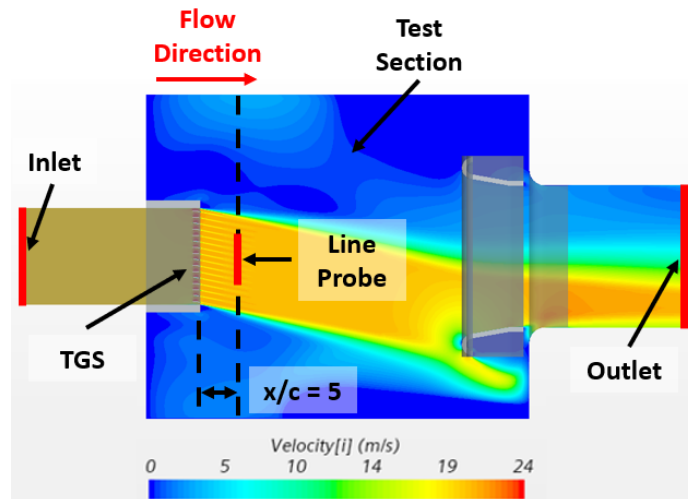


Figure 3.5: Top view of the simulation domain with simulation setup labels. Data is taken at 5 chord lengths (c) away (x-direction, dashed black line) and at the core of the flow (red line).

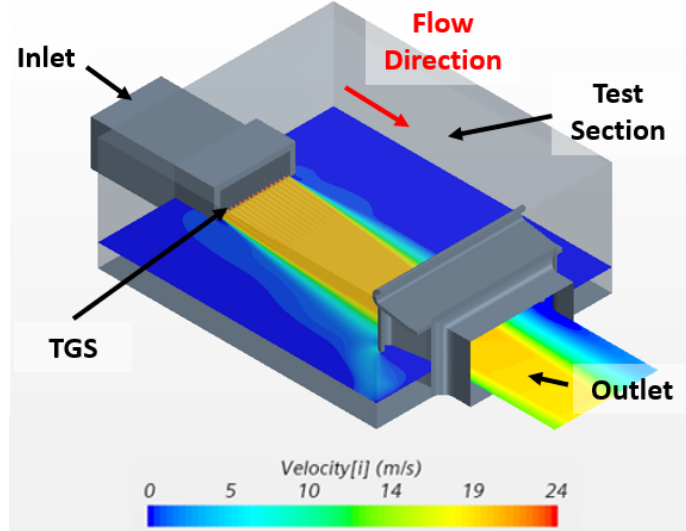


Figure 3.6: Isometric view of the simulation domain.

Flow velocity data was collected for each simulation that was conducted. In particular, streamwise and spanwise velocity was collected with line probes in order to obtain flow yaw,  $\beta$ , across the entire test section. The velocity data was analyzed using MATLAB and flow yaw plots were created at different chord lengths away from the trailing edge. As per Table 3.2, several configurations have been chosen with varying yaw system parameters. From the simulations performed, the following conclusions were drawn:

1. **Number of Airfoils** - The peak flow yaw angle decreased with the number of airfoils in the cascade. Reducing the number of airfoils increased the spacing and thus the diffusion factor, which resulted in less lift and greater potential for flow separation and drag.
2. **Flap Length** - Increasing flap length improved flow turning for the cascade. Increasing flap length also increased the overall thickness of the airfoil (profile was constant), leading to additional blockage and losses.
3. **Flap Angle** - Flap angle increases flow yaw at all angles considered. The yaw and flap angle have been shown to be linearly related with a slope of  $\beta/\phi = 0.74$  after 2 to 3 chord lengths away. Finally, no indications of potential stall was observed at all cases tested.

Table 3.2: Overview of the various airfoil configurations and details pertaining to the simulations.

# of Airfoils	Flap % of chord	Flow Speed (m/s)	Flap Angle - $\phi$ ( $^{\circ}$ )	Note
16	50	17.5, 27.8	0, 5, 10	HALF, No collector
16	50	20	0, 2.5, 5, 7.5, 10, 12.5	HALF, With collector
15	50	20	5, 10, 12.5	EQ, With collector
15	30, 35, 40, 45	20	12.5	EQ, With collector
8, 12	40	20	12.5	EQ, With collector
10, 12	40	20	0, 5, 10, 15	EQ, With collector

### 3.4.2 Mesh Refinement

A mesh refinement study was conducted to ensure that the chosen simulation cell resolution was sufficient to obtain accurate results. The simulations were conducted with a static flap angle of  $15^{\circ}$  at different cell resolutions and appropriate surface treatment modifications, such as prism layers. The average yaw across the line probe for each resolution is shown in Table 3.3.

Table 3.3: Summary of the mesh refinement study results.

Mesh	Low Res. 1 ~3.7 mill. cells	Low Res. 2 ~6.7 mill. cells	Baseline ~13.3 mill. cells	High Res. 1 ~22.3 mill. cells	High Res. 2 ~30.3 mill. cells
Average Yaw Angle ( $^{\circ}$ )	11.14	10.84	10.92	10.87	10.97
Pressure Drop (Pa)	107.20	106.40	106.15	106.82	105.47

The results shown in Table 3.3 show that the average yaw angle measured from the line no longer changes significantly after the baseline case. The results for the high resolution meshes 1 and 2 have percent differences of less than  $\pm 1\%$  compared to the baseline case for both the yaw angle and the pressure drop.

These differences are considered to be acceptable. The baseline mesh is applied for other angles of attack for the airfoil sections considered in this study.

### **3.4.3 Additional Simulation Considerations**

Several considerations should be noted on the differences between the methods applied for the simulations and simplifications made in comparison to the intended physical experimental setup. First, the simulations are run for steady flows; thus, only static flap angles were considered which is in contrast to the planned dynamic flap motion to be applied. Experimental measurements are, therefore, required to understand the full extent of the TGS flow yaw generation performance. Next, a chord length of 50 mm was chosen at the beginning of the design phase as a first step; simulations with different chord lengths were not conducted and thus it is unclear whether or not different chord lengths are more effective. However, based on the results of the number of airfoils, it can be assumed that a reduction of chord length reduces flow turning as per the diffusion factor relation. Finally, the most significant consideration is the fact that the experimental TGS and the simulation model were significantly different. For example, the experimental TGS has both the yaw and active grid subsystems installed together while the active grid is not modeled in the simulations as shown in Fig. 3.7 and 3.8. Furthermore, these figures also shows that the experimental airfoil has a mechanical gap between the body and flap while the simulation was modelled as a single piece. These differences between the simulation and experimental models are expected to have a significant negative effect on the flow turning performance. Therefore, all of these factors and considerations may cause differences between the simulated and experimental results.

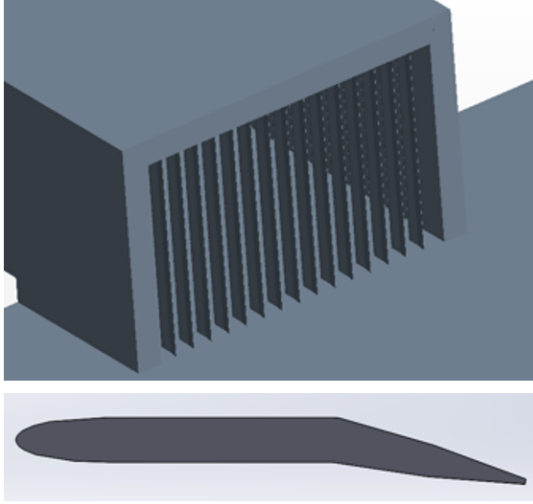


Figure 3.7: 3D airfoil cascade (top) and airfoil (bottom) model used for the simulations. The TGS CAD model does not include the active grid between the airfoils and uses a simplified airfoil body model with a truncated trailing edge.

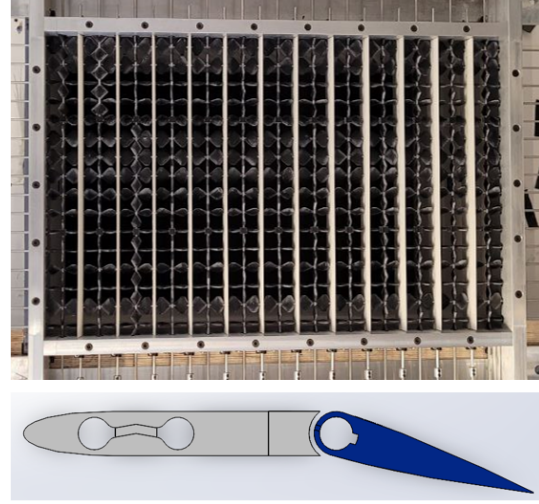


Figure 3.8: Final TGS assembled and installed in the test section (top) and the 3D airfoil model (bottom) used for the experiments. The physical TGS model includes the active grid (black elements and shafts) between the airfoils.

### 3.5 Yaw System Specifications

The theory and simulations discussed previously were analyzed alongside the project objectives and requirements defined in Sections 3.1.1 and 3.1.2 to determine the final yaw system specifications. The chosen specifications for the system are shown in the table below.

Table 3.4: Chosen yaw system and airfoil (AF) specifications.

# AF	AF Spacing	Chord Length	Flap Length	Flap Range	Op. Freq.
$N_{af}$	$s$ (mm)	$c$ (mm)	$R_f$ (% chord)	$\phi_{max}$ ( $\pm^\circ$ )	$f$ (Hz)
12	48.41	50	40	20	0 - 15

## 3.6 Motor Selection and Testing

### 3.6.1 Motor Selection

Two main factors were used to determine the suitability of different motor options. First, the motors were required to be able to oscillate and hold the flaps at desired angles and frequencies at nozzle velocities of up to 20 m/s at the defined specifications in Section 3.5. Secondly, the motors must be able to physically fit onto the frame when placed adjacent from one another; doing so reduces the complexity of the mechanical interface design. The process of analyzing these factors are discussed below.

The most important factor when choosing the motor was its ability to drive all possible test cases. It was expected that airfoil flap operation would require more performance from the motors compared to the active grid motion. As such, force and torque analysis on the TGS flaps were conducted to determine the minimum performance parameters of the chosen motor. The required torque from the motors was determined using static flap analysis (control volume - RTT and simulations) and dynamic vibration analysis with conservative parameters ( $\phi_{max} = \pm 20^\circ, f = 20$  Hz). The former two methods only consider the flaps at the maximum angle (aerodynamic forces only) while the latter considers all positions of the flap over a cycle and the inertial load of the shaft. Still, all three methods were in close agreement with one another, indicating that the forces on the shaft is dominated by aerodynamic forces acting on the flaps; the minimum required torque to perform all required TGS functions was calculated to be approximately 0.0323 Nm for all three torque calculation methods used. Therefore, torque requirements were determined and used for the next motor selection steps.

Integrated stepper motors from Applied Motion were chosen due to their simple control scheme, low cost and performance options. Due to the many different unknown factors in the wind tunnel, it was decided that the motors would be over-sized for the required application. The largest motors available that would fit between the shaft spacing (48.41 mm) were NEMA 17 motors with a frame size of approximately 42.3 mm. Accordingly, Applied Motion's STM17Q-3RN motors were chosen as they were sufficiently suitable for the

TGS applications.

### 3.6.2 Motor Movement Cases

In order to replicate unsteady on-road flow conditions, the motors must be able to perform various movement cases. The current possible motion cases are listed below.

1. **Point to Point** - Point to Point movement is the most basic function of the motors. This motion can be used to create mean angles in the flow through holding static flow element, such as airfoil flaps, positions. The only important parameter in this function is the move distance between each point and whether or not the move is relative or absolute.
2. **Rotation** - Rotating flow elements are not usable for the active airfoil cascade. However, this movement case can be used with the active grid for broadband turbulence generation. Important parameters for this case include the speed and direction of the rotation. Furthermore, another important function of this movement case, which will not be discussed in detail for this work, is the ability to randomly change the direction and speed of the rotation and the ability to couple the rotation of certain motor shafts during testing.
3. **Oscillation** - Repeated Point to Point movements allows the ability to create oscillations in the flow. Attempts were made to continuously update the position of the shaft during oscillations (time-based commands) but was not feasible due to internal delays ( $\sim 0.0016$  s per command and per motor) when sending serial commands to multiple motors in MATLAB. Instead, a path planning approach was used to develop equations for the velocity and acceleration of the oscillation.

$$\omega = \frac{4f\phi_A}{R_v - R_s + 1} \quad (3.2)$$

$$\alpha = \frac{16f^2\phi_A}{R_s^2 - R_v^2 - 2R_s + 1} \quad (3.3)$$

The motor velocity ( $\omega$ ) and acceleration ( $\alpha$ ) values are calculated using the oscillation frequency ( $f$ ), oscillation amplitude ( $\phi_A$ ), fraction of a cycle where the motor moves at constant velocity ( $R_s$ ) and the

fraction of a cycle where the motor stops ( $R_s$ ). The  $R_v$  and  $R_s$  are used to determine the shape of the oscillation, whether it be a sinusoidal, triangle or square waveform. Typical values for  $R_s$  are 0, 0.8 and 0.2 while values of  $R_v$  are 0, 0 and 0.6 for sine, triangle and square wave oscillations respectively. It should be noted that these values are always rounded within the motor registers automatically. Implications of this rounding will be discussed in the next section. Additional discussion on these parameters and the control scheme are discussed in Appendix D.

Two main oscillation frequency modes are possible with the system. First, a constant frequency mode is commonly used for most test case scenarios. In this case, the flaps will oscillate at a set constant frequency for the entirety of the measurements. On the other hand, the system also has functionality to ramp up and ramp down the oscillation frequency between two set frequencies. This mode is referred to as frequency scanning where the oscillations will cover a range of frequencies between the two set values during a single run.

### 3.6.3 Motor Testing

Physical tests were conducted on sample motors to ensure that the chosen motor option was suitable for the TGS. The test setup consisted of the motor, an encoder, a 3D printed mass and 2 springs as shown in Fig. 3.9. A PC, National Instruments Data Acquisition System (DAQ) and power supply (24 V) was also used for data collection and power respectively. The encoder was used to measure and monitor the shaft position during testing. The 3D printed mass was used to replicate the expected inertial load of the shaft and flap assembly to be used in the full-sized prototype. Two masses, shown in Fig. 3.10, were tested; the first mass had an equivalent moment of inertia (MOI) as the final flap-shaft assembly while the second mass had 4 times the expected MOI in order to test the motors under much higher loads than expected. Two springs were used to replicate the elastic forces due to the moving air as the flaps oscillate back and forth. The springs were identical and pushed the mass back towards the equilibrium position during oscillation testing as shown in Fig. 3.11. The spring position and constant was also chosen to replicate the forces discussed in Section 3.6.1.

The test results showed that the motor was able to perform all required functions with both masses within acceptable accuracy ranges. Encoder data showed that the oscillation amplitude was within 1 to 2 encoder counts, equivalent to around  $0.30^\circ$ , during oscillation. There is little concern about the amplitude of the oscillation because the motors are built to complete move commands before performing another. However, oscillation frequency errors within  $\pm 2\%$  were observed during testing. The observed frequency errors are likely due to two main factors. First, the internal rounding of the calculated velocity and acceleration values within the motors themselves may cause significant issues with obtaining the set oscillation frequency during testing. The exact velocity and acceleration values calculated from Equations 3.2 and 3.3 are proportional to the

oscillation frequency,  $f$ , and  $f^2$  respectively. Thus, any rounding has a significant effect on the measured frequency of the oscillation. Moving on, the second possible cause for the frequency error is the internal delays between motor commands inside the motors themselves; the motors oscillate by cycling through a set of pre-programmed commands each with their own micro-delays. This explains why the measured frequency tends to lag more and more as the set frequency increases. Still, the error was acceptable since it was also observed that all motors have the exact same frequency error as long as the exact same commands (amplitude and frequency) are sent. This happens because the motors have the exact same rounding and internal command delays. Therefore, the motor testing has shown that all required functions were possible from the chosen motors.

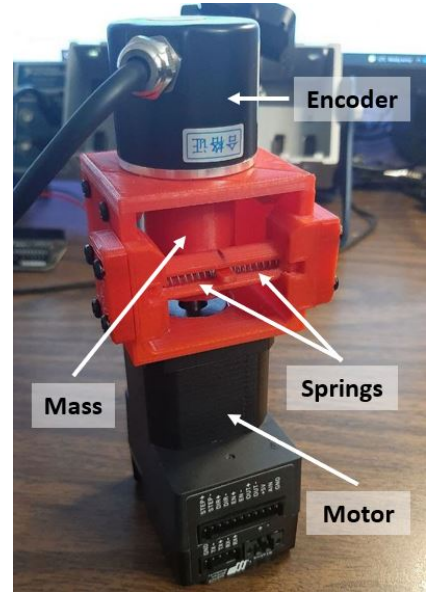


Figure 3.9: Motor spring and mass testing assembly with an encoder shown on top.



Figure 3.10: Equivalent MOI test mass (left) and the 4x MOI test mass (right).

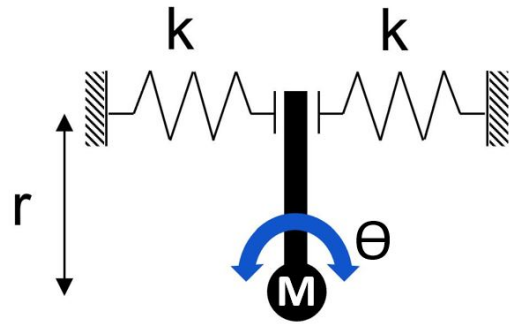


Figure 3.11: Schematic diagram of motor spring assembly. The springs replicated torques acting on the flap during the planned experiments ( $\tau_{flow} = \tau_{spring} = kr^2\theta$ ).

## 4 Mechanical and Electrical/Software Design

The following chapter discusses the final mechanical and electrical design for the TGS. There are selected CAD, electrical, and operational codes that have been added to the Appendix for reference.

### 4.1 TGS Mechanical Assembly and Installation

The TGS is made up of three main mechanical subsystems that are designed to achieve the functional requirements discussed in Section 3.1.2. These subsystems include the active airfoil cascade, gusting and active grid). These subsystems are connected to a single aluminum frame fitted to the front of the test section nozzle. Only the design of the active airfoil cascade or yaw subsystem will be discussed in this thesis.

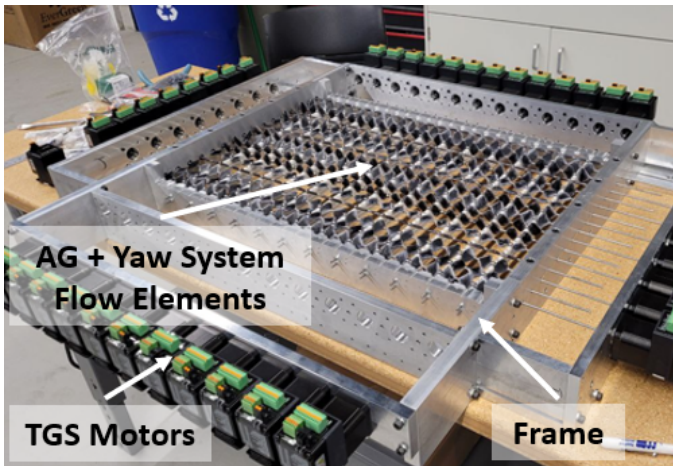


Figure 4.1: TGS assembly prior to wind tunnel installation.

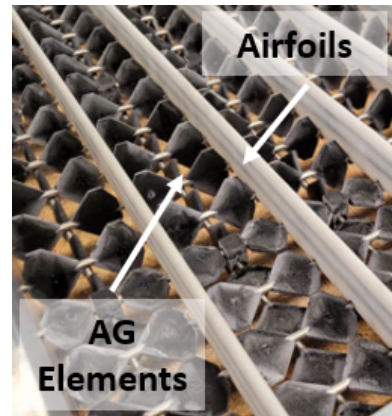


Figure 4.2: Close up view of the fixed airfoils and active grid elements.

The final design specifications of the active airfoil cascade were given in Table 3.4. The TGS consists of 12 equally spaced airfoils ( $s = 48.41$  mm) along the width of the wind tunnel nozzle. The airfoils have a

chord length of 50 mm and is made up of two main parts, the fixed airfoil body and the flaps, as shown in Fig. 4.3 and 4.4.

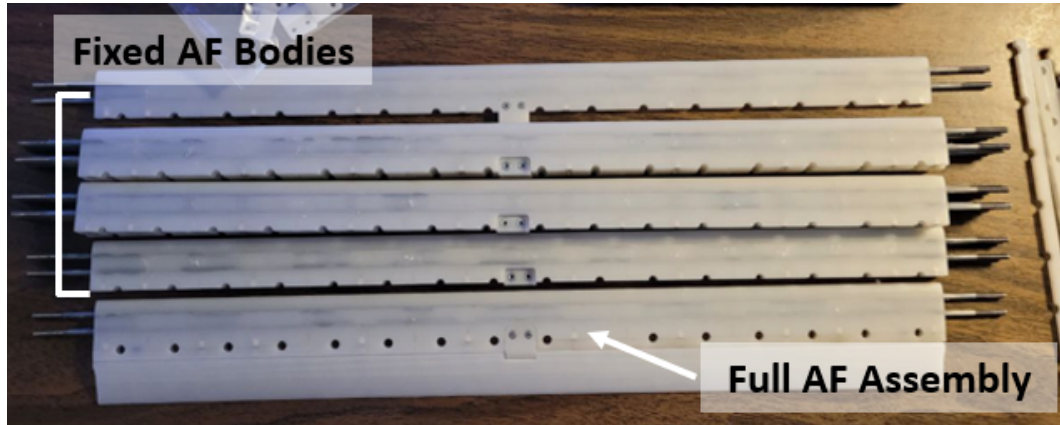


Figure 4.3: Yaw system fixed airfoil bodies during assembly (final, full-sized). A full airfoil assembly (fixed body, flap, flap support) is shown at the bottom.

#### 4.1.1 Fixed Airfoil Body

The fixed airfoil body combines both the leading edge and flat plate extension, as discussed in Section 3.3.3, in a single 3D printed (SLA) part. The flat portion of the airfoil body is also used to provide support for the horizontal grid components; in order to do this, bearing cavities have been designed into the airfoils and the shafts (with bearings) are fastened with a back-plate. The back-plate is attached with M2 screws which are fastened to the threaded inserts installed in the fixed airfoil body. Moving on, the airfoil body contains two 3 mm steel rods that run through the entire length. The steel rods are glued to the inside of the airfoil body via internal glue channels. Each of the steel rods also have threaded ends that extend past the ends of the airfoil body; these threaded ends are used to fix the airfoil body to the aluminum TGS frame via

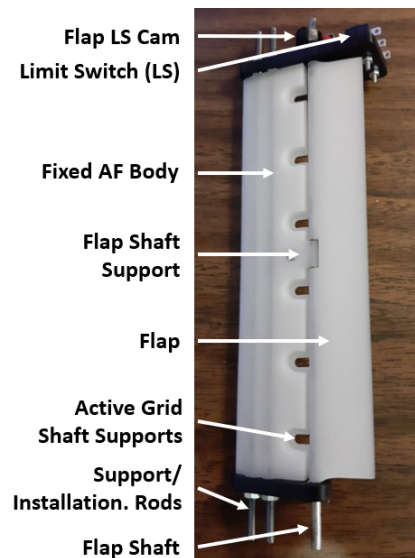


Figure 4.4: Prototype (early mini design) airfoil assembly with labeled parts.

M3 nuts. Finally, the airfoil body was designed with a spot to attach the flap shaft support holder which will be discussed below.

#### **4.1.2 Airfoil Flaps**

A single flap assembly is made up of a 3D printed (SLA) flap glued to a 1/8" steel shaft and a free moving flap support holder. A miniature prototype model of the assembly is shown in Fig. 4.4. The flap support holder, shown at the center of the assembly, is attached to the fixed airfoil body to add additional structural rigidity to the flap shaft during operation (due to the aerodynamic forces acting on the flap). The location and number of the flap support holders was determined using bending calculations during the conceptual design phase. Next, the flap shaft extends much farther past the flap length in order to couple the shaft to the TGS motors. Furthermore, all flap shafts are fitted with bearings at both ends of the shaft to fix the position of the shafts with the frame.

### **4.2 TGS Electrical and Software Design**

The electrical design of the TGS consists of the power and motor communication subsystems. The TGS uses 54 individually controlled Applied Motion STM17Q-3RN motors. Only 42 of the planned motors were used during this thesis for testing. Additional motors were later purchased so that all subsystems could be operated at the same time.

#### **4.2.1 Communication and Power**

All TGS motors are powered with 5 Meanwell NDR-480-48 power supplies (48V, 10A) and are controlled through MATLAB via 4-wire RS485 communication as shown in Fig. 4.5. Power is supplied to the motors via 5 daisy chained power lines. The motors are also connected through daisy chained communication lines with cat5e wires. Up to 32 motors can be connected to each line; as such, the current system (42 motors) utilizes two daisy chains of 21 motors each. The daisy chains are connected to a PC via RS232 Serial PCIE

cards and 2 RS232 to RS485 adapters. The wiring diagrams can be found in Appendix C.

Commands are sent to each motor via serial command line. Each motor on a single line is assigned a unique character address that is used as a reference for motor commands. Through this communication setup, separate commands can be sent to each motor individually, allowing fully independent control for each motor in the system.

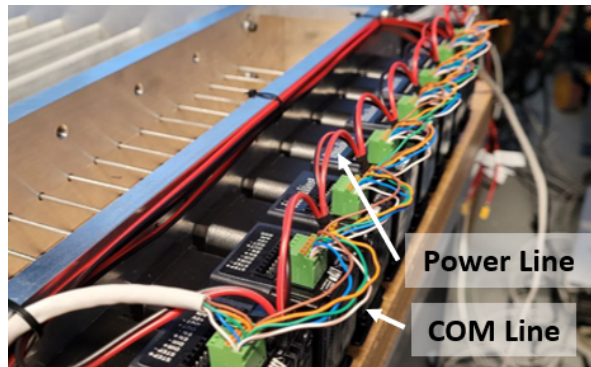


Figure 4.5: TGS motor power and COM lines.

#### 4.2.2 Motor Control

The most important aspect of the motor control design is the ability to control up to 54 motors simultaneously in a single control script. Furthermore, the motor command timing issues described in Section 3.6.3 makes it difficult to use timed commands; internal delays in the software, such as the time it takes to send a serial command, will create significant delays when attempting to constantly update the position of all motors in the system. Additionally, these internal delays will create synchronization issues with the motors during testing. Therefore, sending continuous timed commands to control each individual motor is not feasible for this system.

A motor control system that utilizes Applied Motion's Q-Programming software was developed in order to get around the previously discussed issues. An example of a program is shown in Fig. 4.6. The core of the motor control system revolves around utilizing the internal registers and memory of the motors. Based on the equations developed in Section 3.6.3, the oscillation behavior of each individual motor can be controlled through a set of parameters. These parameters can be modified and edited inside the motor registers before the test is run. In other words, motors can be loaded with the proper commands and parameters before the run begins. Afterwards, motors can be programmed, through Q-Programming, to read and access the registers to perform the various motion cases. Therefore, the Q-Program acts as a basic set of instructions or a template for the motors that uses preset register values or variables set before the run. The list of registers

and their descriptions are shown in Table 4.1. Meanwhile, the current Q-Program descriptions are shown in Table 4.2. Additional information on the Q-Programs are given in Appendix D.

Table 4.1: Motor control parameters

Parameter	Description	Values
A	Defines the main motion of the motor: static, rotation, oscillation (amplitude)	0 - Static Position 1 - 359: Oscillation Amp. ( $^{\circ}$ ) 360: Rotation
B	Defines the oscillation frequency (if A is an oscillation) or rotation speed (if A is a rotation)	0 - 20: Oscillation Frequency (Hz) 0 - 20: Rotation Speed (rps)
$R_v$	Percentage of the osc. cycle where the motor moves at constant velocity	Sine Wave: 0 Triangle Wave: 0.8 Square Wave: 0.2
$R_s$	Percentage of the osc. cycle where the motor is stopped	Sine Wave: 0 Triangle Wave: 0 Square Wave: 0.6
$\theta$	Mean offset angle for oscillations or static positions	0 - 360 ( $^{\circ}$ )
t	Time lag	seconds

The parameters described in Table 4.1 can then be used to control each individual motor independently. Motor instructions are set into a motor control parameter matrix prior to the run. In this matrix, each row represents the motors from 1 to 42 and each column represents the parameters discussed in the table above. The order of the parameters in each row is as follows: A, B,  $R_v$ ,  $R_s$ ,  $\theta$ , t. An example of this matrix is shown in Fig. 4.7. Thus, the matrix contains all of the required information and instructions to control each individual motor independently. This matrix can then be saved into a Motor Program Set (MPS) and then be used for different tests.

Table 4.2: Q-Program descriptions.

QP#	Description
1	Performs all functions or motion cases described in Section 3.6.2 based on the provided MPS. (fixed oscillation cases only)
2	Homes all motors.
3	Performs all functions or motion cases described in Section 3.6.2 based on the provided MPS. (frequency scanning only)

Motor Motion					
Line	Label	Cmd	Param1	Param2	Comment
1		SO	Y1H		Turn off output pin
2		TR	5	360	Check for rotation condition
3		QJ	E	#LABEL1	Go to rotation command (jog) if rotation is selected
4		TR	5	0	Otherwise, check for static position command
5		QJ	E	#LABEL2	Go to static position command if selected
6		WD	4		Pause motor for milliseconds defined in variable (user) register 4
7	LABEL3	SO	Y1L		Clock high
8		WD	3		Pause motor for milliseconds defined in variable (user) register 3
9		RM	2	D	Set DI register to variable (user) register 2
10		FP			Move shaft to the position defined in DI
11		WD	3		Pause motor for milliseconds defined in variable (user) register 3
12		SO	Y1H		Clock low
13		WD	3		Pause motor for milliseconds defined in variable (user) register 3
14		RM	1	D	Set DI register to variable (user) register 1
15		FP			Move shaft to the position defined in DI
16		WD	3		Pause motor for milliseconds defined in variable (user) register 3
17		QG	#LABEL3		Return to label 1 (loop back to the beginning)
18	LABEL2	QK			Kill the queue -> Stay at initial position
19	LABEL1	WD	4		Pause motor for milliseconds defined in variable (user) register 4
20		SO	Y1L		Clock high
21		CJ			Start jog (rotation)
22					

Figure 4.6: Example Q-Program (QP1) within the motor memory.

```

mp2 = [40  1  0  0  0  0; % M01A [TOP]
        40  1  0  0  0  0; % M02A
        40  1  0  0  0  0; % M03A
        40  1  0  0  0  0; % M04A
        40  1  0  0  0  0; % M05A
        40  1  0  0  0  0; % M06A
         0  0  0  0  0  0; % M07A
        20  2  0  0  0  0; % M08A
        20  2  0  0  0  0; % M09A
        20  2  0  0  0  0; % M10A
        20  2  0  0  0  0; % M11A
        20  2  0  0  0  0; % M12A
        20  2  0  0  0  0; % M13A
         0  0  0  0  0  0; % M14A [RIGHT]
         0  0  0  0  0  0; % M15A
         0  0  0  0  0  0; % M16A
         0  0  0  0  0  0; % M17A
         0  0  0  0  0  0; % M18A
         0  0  0  0  0  0; % M19A
    
```

Figure 4.7: Example MPS parameter matrix.

### 4.2.3 System/Software Limits, Motor I/O and the Encoder

The system was designed with mechanical and software limits. The yaw system has been designed with limit switches to prevent possible collisions between the flap and the fixed airfoil body. Each airfoil assembly has a single limit switch that is activated with a symmetrical dual-lobed cam connected to the flap shaft as shown in Fig. 4.8. The limit switch is connected to the motor I/O port and triggers a stop command when the switch is pressed. The cam limits the flap angle to  $\pm 20^\circ$ . Moving on, the software was built to perform system checks for the motor communication and motor programs. The software will check if all motors are properly connected and receive the proper commands prior to

running. Likewise, the software will also ensure that the inputted MPS are correct; for example, the software will flag potential issues such as flap motors that are programmed to spin. Therefore, these limits will ensure that all motors are properly set and connected to prevent any issues during testing. The motors have also been programmed to provide a basic reference pulse, through the motor I/O port, during oscillation functions. The reference pulse changes state (HI/LO) when the motors change directions during oscillation. This reference pulse will be used with other planned tests and measurement plans, such as plotting collected data and conducting future PIV measurements.

Additionally, another reference signal is provided by the TGS encoder. Attempts were made to utilize the motor's built-in encoders during testing but it was determined that it was not feasible due to the previously discussed continuous command timing issues. Instead, the TGS is equipped with a single 600 PPR incremental encoder; the encoder uses X4 encoding giving a total CPR of 2400 and a resolution of  $0.15^\circ$ . The encoder is connected to the opposite end of the motor flap shaft via a 3D printed mount. This encoder provides the reference flap position information for later analysis such as phase-averaging results.

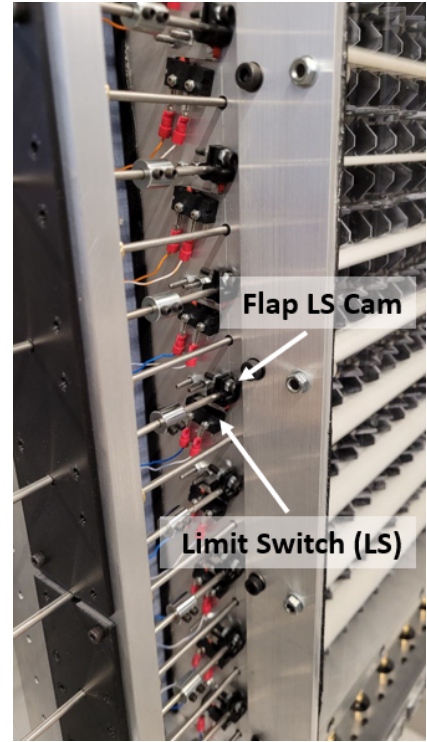


Figure 4.8: Motor limit switches and cams.

## 5 Experimental Setup and Methods

This chapter provides an overview and descriptions on the wind tunnel, flow diagnostic instruments, data acquisition system, and other supporting hardware. Descriptions of the planned tests and expected outcomes will also be provided. Afterwards, notes on key analysis methods will be presented.

### 5.1 Wind Tunnel

All tests were conducted in a 1/10-scale 3/4 open-jet automotive model wind tunnel that was donated by Aiolos Engineering Inc. and BMW to Prof. Hanson's Fluid Mechanics and Flow Control (FMFC) Research Laboratory located in the Lassonde Research Center at York University. The wind tunnel has a 6.84 to 1 contraction and is equipped with a fan capable of producing test section flow velocities of up to around 70 m/s. The wind tunnel is also equipped with a heat exchanger that can be used to maintain flow temperatures inside the test section.

The TGS was installed directly in front of the wind tunnel nozzle as shown in Fig. 5.1. The TGS is primarily secured to the nozzle with L-brackets and 10 M8 bolts. Steel cables are used to further support the TGS and additional screws are used



Figure 5.1: TGS installed onto the wind tunnel nozzle.

to compress a gasket between the TGS and nozzle to prevent air leakage.

The wind tunnel velocity was controlled with an external ABB Variable Frequency Drive (VFD). The VFD is directly controlled with MATLAB using a Modbus interface. Only wind tunnel speeds between 7.5 - 25 m/s are required during testing.

## 5.2 Coordinate System

The coordinate system employed for this thesis is shown in Fig. 5.2 and 5.3 for the actual system and the CAD model, respectively. The origin of the coordinate system is taken at floor of the test section ( $Y = 0$  mm) and at the exit of the TGS ( $X = 0$  mm). The origin is also located at the center of the width of the nozzle ( $Z = 0$  mm).

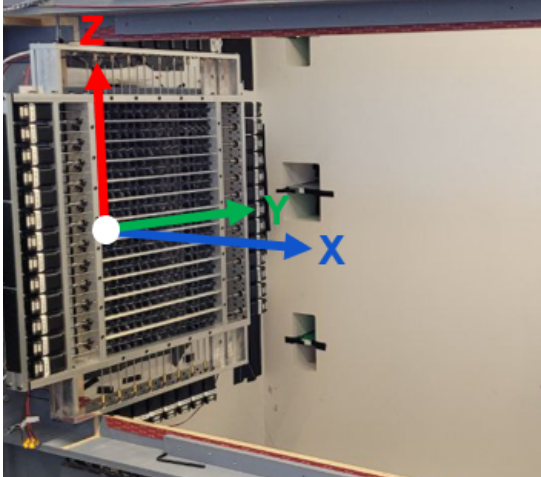


Figure 5.2: Coordinate system shown on the installed TGS.

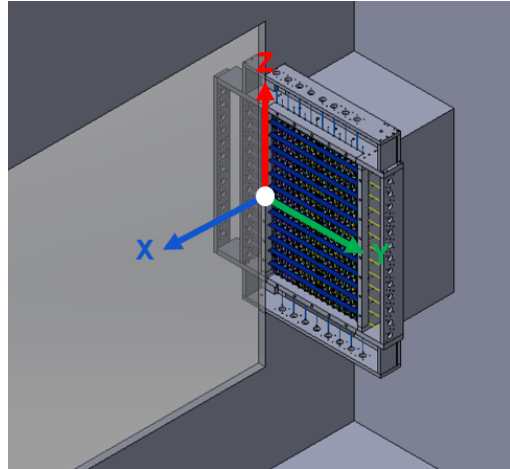


Figure 5.3: Coordinate system shown on the wind tunnel CAD model.

## 5.3 Measurement Equipment

The following section describes the various flow measurement equipment that was used as a part of this research.

### 5.3.1 Temperature Probe

A thermocouple was used to measure the flow temperature inside the test section. The probe is installed at the exit of the test section. The probe can measure temperatures up to  $50^{\circ}\text{C}$  and outputs a voltage between 0 and 10 volts. Typical testing temperatures range from  $19^{\circ}\text{C}$  to  $22^{\circ}\text{C}$ . The range of the linear relationship between the sensor output in voltage and the temperature was calibrated at two reference temperatures.

The temperature probe information was used for temperature compensation for other measurement techniques. Pressure probe temperature compensation was done by calculating the density of the air at the measured temperature. The flow velocity was then calculated with  $U = \sqrt{\frac{2\Delta P}{\rho}}$ . Meanwhile, temperature compensation for the hotwire was done using a common method described in the literature [25].

### 5.3.2 Differential Pressure Probe

A  $1/8''$  pitot static tube was used to measure the streamwise velocity of the flow. The pitot static tube was placed within the core of the flow and was aligned parallel to the direction of the flow. Furthermore, the tube was supported with steel wires to increase the stiffness and reduce the vibration during operation. A Honeywell HSCDRRD002NDAA5 Differential Pressure Transducer (Range:  $\pm 0.5$  kPa  $\pm 0.25\%$  FS) was used with the pitot static tube.

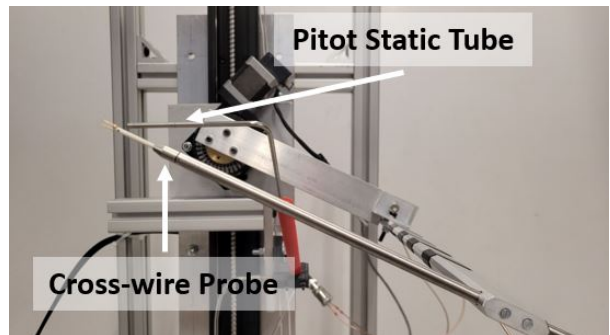


Figure 5.4: Pitot static tube and the cross-wire probe assembled onto the traverse.

### 5.3.3 Hot-wire Anemometry

Time resolved measurements of the flow were primarily done using hot-wire anemometry. A Dantec cross-wire probe was used to measure the flow angle and flow velocity at different locations. The cross-wire was setup and balanced using a Dantec Streamwire Pro shown in Fig. 5.5. The hot-wire specifications are as

follows; the hot-wire was set with an overheat ratio of 0.7 for both wires, an offset of 1.136V and a gain of 8. Additionally, the hot-wire was set to output voltage data at 20 kHz with a 10 kHz low pass filter. The cross-wire probe was placed near the pitot static tube ( $\Delta Y = 40$  mm) at the core of the flow. This ensures that the pitot static tube measurements can be used as reference for the measured cross-wire velocity magnitude during the calibrations.



Figure 5.5: Dantec Streamline Pro used for setting up and conducting hotwire measurements.



Figure 5.6: National Instruments data acquisition system used for data collection.

### 5.3.4 Data Acquisition System (DAQ)

All data was collected using a National Instruments (NI) data acquisition system (DAQ). The DAQ samples 5 analog inputs (2 NI 9125 Analog I/O Modules) and 2 digital inputs (1 NI 9401 Digital I/O Module, encoder quadrature signal A and B) at 20 kHz simultaneously. All modules were connected to a single NI cDAQ-9178 (8-module) connected to a PC and is shown in Fig. 5.6. The exact input assignments and descriptions are shown in Table 5.1. The NI DAQ was interfaced with the PC via built-in functions in MATLAB's Data Acquisition Toolbox. Data was sampled in the background during measurement operations.

Table 5.1: DAQ Input Descriptions

Input #	Description
1	Cross-wire Voltage 1 (Raw)
2	Cross-wire Voltage 2 (Raw)
3	Pressure Probe Voltage
4	Temperature Probe Voltage
5	Encoder Position Signal
6	Motor Reference Clock Signal

## 5.4 Traverse System

### 5.4.1 Assembly

A 4-DOF traverse system was used to move the measurement instruments within the test section and is shown in Fig. 5.7. The system uses 3 linear traverses (T1 - T3) for XYZ translation and a rotary table (T4) for XZ-plane rotation. All of the aforementioned parts are driven using stepper motors. Additionally, several parts were machined to complete the assembly of the system; this includes interface/connection plates between each of the traverses and probe holders for both the pitot static tube and the cross-wire holder. Other assembly elements include structural pieces of extruded aluminum and their brackets or electrical component and wiring guides. Finally, the traverses are equipped with limit switches to prevent collisions with different parts of the traverse system.

Stiffness was an important concern during the design and early testing of the traverse system. After installation, it was visually observed that the original traverse assembly was susceptible to significant vibration during early testing. Multiple changes and iterations of the traverse system assembly were tested to reduce the overall vibration at the probes. These changes include changing the design of the structural extruded aluminum or interface plates, 3D printing aerodynamic parts that fit over corners/bluff bodies and adding an additional follower traverse. It was visually observed that there was little to no more vibration in both the pitot static tube and the cross-wire arm while running wind tunnel flow at its maximum testing

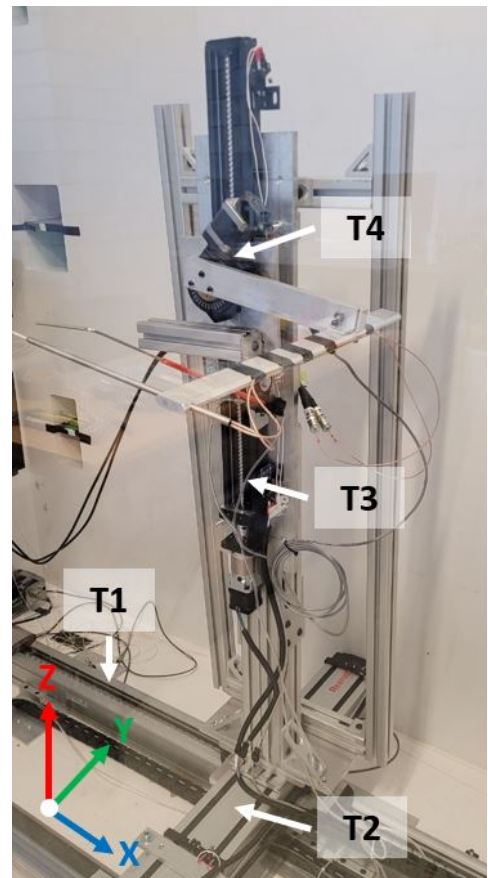


Figure 5.7: Traverse system installed inside the wind tunnel test section. Traverse labels are shown.

speed ( $\sim 25$  m/s). These improvements minimize potential effects of sensor vibration on the measurements.

#### 5.4.2 Control

The traverse system was controlled via MATLAB through serial communication. T1's motor was controlled using an integrated Schneider Electric controller while T2 - T4 use an external MMC-4s stepper controller. Because these groups (T1 and T2 - T4) have different serial command line syntax, their control commands have been combined into a single setup and move function within MATLAB. However, due to the limitations of the MMC-4s controller, only T1 has access to closed feedback control. For simplicity, all traverse positions are tracked within the software only in an open loop. There are several commands that can be sent to the motors within MATLAB, such as relative moves, absolute moves, homing traverses, setting home position and requesting the current position. Thus, all required functions for conducting tests are possible within the main control script.

During testing, predefined probe positions were used. The measurement positions were defined prior to a run and were stored in a separate file. Within these files, the absolute XYZ positions and orientation of the measurement probe were stored in sequential order. Each file can store different types of measurement position ranges such as single point, multi-point, plane scans or 3D grid scans. Therefore, different probe position and orientation sequences can be stored in separate files, defined before any run and be used for multiple tests.

The probe position sequencing was automatically generated using a custom made path optimization script. The script generated the optimal probe position order to reduce the time of the test. To achieve this, the script requires the user to input all possible X, Y, Z positions and probe angles in separately. Afterwards, all possible combinations of the defined coordinates were generated and were ordered to reduce testing time accordingly. The script automatically considers the speed of each traverse as well as the distance between points. This path generation script has shown significant improvements to testing time; testing times have shown reductions of up to 50% with tests that require upwards of 250 measurement points.

## 5.5 Control System and Program Flow

A typical experiment consisted of 5 different steps. These steps are the run preparation, x-wire calibration 1, data collection, x-wire calibration 2 and data conversion. Descriptions of these steps will be discussed in the following sections.



Figure 5.8: Measurement program steps.

### 5.5.1 Overview

The MATLAB control system is primarily set up and operated using three main files: the program/test configuration file (step 1, programVariables.m), the main control script (step 2 - 4, main.m), and the data conversion script (step 5, dataConverter.m). The program configuration file contains all of the editable variables to set up the run. As such, all modifications to different tests will be done through this single file under normal operation. The main control script is run when conducting the experiments. The main script goes through the previously discussed system checks and afterwards leads the user towards an operation menu. In this menu, the user can perform several actions such as manually moving traverses, homing traverses or setting home, manually controlling wind tunnel flow velocity, manually sending motor commands, manually testing selected MPS and starting the test program. Finally, data conversion script is used after data is collected to convert voltage readings into useable data, such as flow velocities or flow angles.

### 5.5.2 Run Preparation

Majority of the work for each test is done during the run preparation stage. All necessary test parameters are defined during this stage and are listed out below.

1. **TGS MPS** - All MPS, as described in Section 4.2.2, must be defined prior to the run since they contain all of the required motor register parameters to conduct tests. All MPS are saved as variables within separate .mat files. Afterwards, these .mat files are loaded into the program variables to choose which MPS to run during the test. Multiple MPS configurations can be tested back to back.
2. **Probe Positions** - All probe positions must be predefined for a test as described in Section 5.4.2. The testing program will automatically move the probe to the defined absolute positions during a run in the optimized order. These probe positions are automatically generated and optimized as described in Section 5.4.2.
3. **Wind Tunnel (freestream) Velocities** - All desired testing velocities must also be defined in the setup. Freestream velocities are defined as percentages based on the current wind tunnel setup. For example, the results in this paper use a wind tunnel setting of 50% which corresponds to a flow velocity of approximately 15 m/s. Like the MPS, multiple freestream velocities can be tested back to back.
4. **Sampling Time** - The final important parameter that must be defined before each test is the sampling time per point. This parameter is defined in seconds and it determines how much data is collected at each measurement point during the run.

### 5.5.3 Calibration

In-situ calibrations are conducted with the cross-wire before and after collecting data. All calibrations are conducted at  $X = 600$  mm. The calibrations move the probe between 9 angles from  $\pm 30^\circ$  in intervals of  $7.5^\circ$  and 9 freestream velocities from 7.5 to 25 m/s creating 81 calibration points. The magnitude of the flow velocity is referenced from the pressure probe. Cross-wire voltages measured at each of these calibration points are then used to construct a surface mesh that relates cross-wire voltages to the flow velocity magnitude, and the cross-wire voltages to the flow angle or yaw. The calibration surfaces are then used to obtain the flow angle or flow velocity magnitude given cross-wire voltages measured during the data collection phase. Examples of these calibration surfaces are shown in Fig. 5.9.

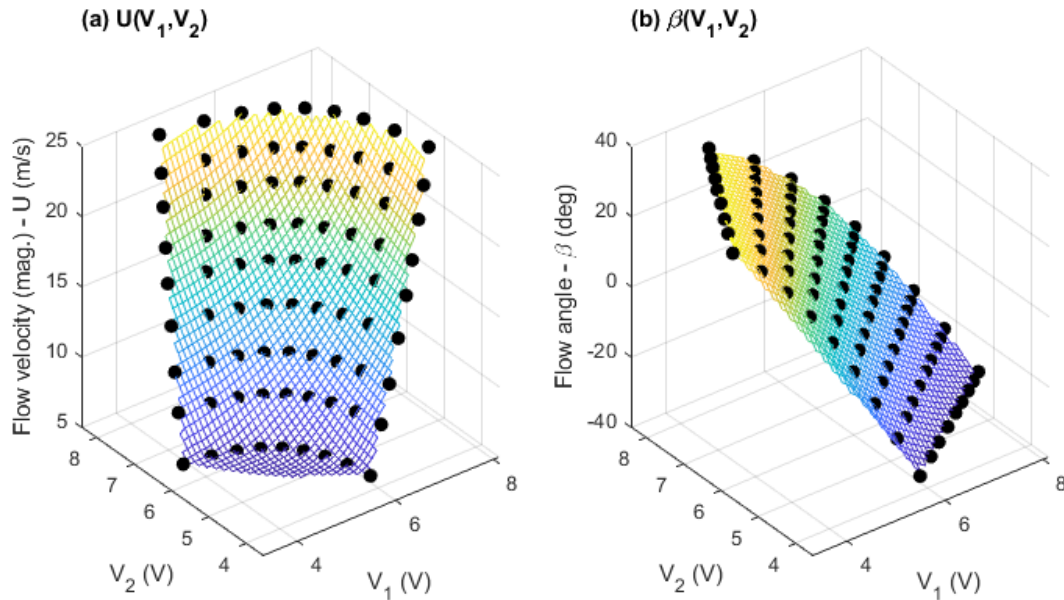


Figure 5.9: (a) Example flow velocity (magnitude) calibration surface. (b) Example flow yaw ( $\beta$ ) calibration surface. The black dots represent the data collected at all set probe angles and freestream velocities. The surface resolution is reduced in this image for clarity.

#### 5.5.4 Conducting Measurements

Measurements are started using the main control script's command menu. Experiments consist of an initial calibration, data collection, and a final calibration. The initial and final calibrations are identical and have been described in the previous section. The measurement run uses the parameters discussed in section 5.5.2. The system will cycle through measuring the flow, for the specified sampling time, at all possible combinations of the defined MPS, probe positions and freestream velocities. This entire process is automatically conducted and requires no user input once started. Once complete, the data is automatically saved onto the PC's drive.

#### 5.5.5 Data Conversion and Drift

Temporal drift, due to the surrounding temperature or measurement equipment, can cause discrepancies when analyzing data measured for extended periods of time. For example, wind tunnel temperatures were commonly observed to range from  $18^{\circ}\text{C}$  to  $24^{\circ}\text{C}$  which may cause variations between measured data before

and after data collection. It is for this reason that two calibrations are conducted during tests; the converted data is linearly weighted towards the appropriate calibration depending on its measurement time in the run. For example, data taken at the start are completely weighted towards the initial calibration while the data at the end are weighted towards the final calibration. This method ensures that temporal drift factors before and after the data collection are accounted for during the conversion.

An important step in conducting the conversions is determining the difference between measurements taken at the beginning against the end of the data collection. In order to test this, the collected data is calculated using calibration 1 and calibration 2 separately and the difference between the two sets is saved as a calibration error. All data used for this paper have an average calibration error of  $\delta U_C = \pm 0.07$  m/s for the freestream velocity and  $\delta \beta_C = \pm 0.10^\circ$  for measured flow angle. Therefore, this validation process ensures that errors due to temporal drift are within acceptable values.

## 5.6 Measurement Positions

All hotwire-based velocity and flow angle measurements were chosen relative to a typical vehicle location in the wind tunnel. A summary of the three main measurement locations are summarized next. All chosen measurement ranges are based on a 1:1 scale vehicle (compared to the wind tunnel and TGS). Measurements were all taken at  $X = 250$  mm away from the TGS; this distance represented the area at the front of a test vehicle placed in the wind tunnel. Furthermore, tests further downstream were not considered because the presence of a vehicle would significantly change the flow compared to the current empty test section setup.

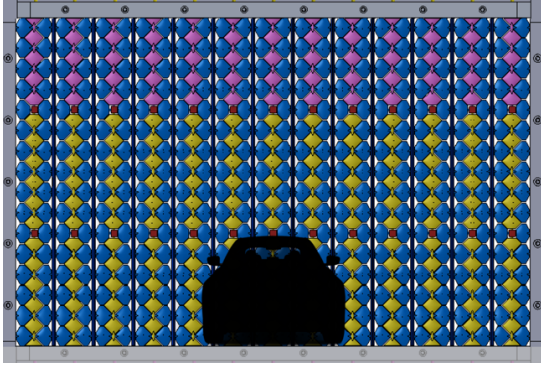


Figure 5.10: Front view of the TGS nozzle area with a to-scale vehicle for reference.

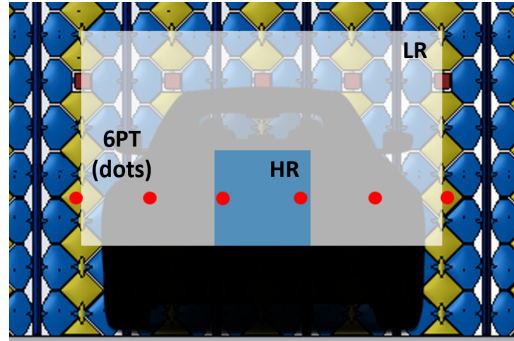


Figure 5.11: Zoomed in view of the vehicle with color coded measurement ranges.

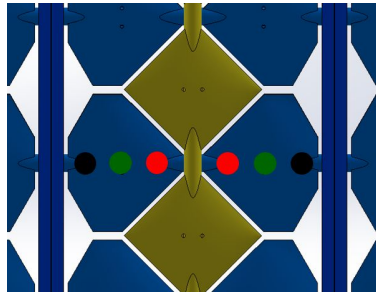


Figure 5.12: 6-points superimposed between a pair of airfoils. Symmetric pairs (across the middle vertical in Fig. 5.11) are color coded (Outer - red, Inner - black, Middle - green).

1. **Low Resolution (LR) Scan** - The LR scan area is represented by the white box in Fig. 5.11. The scan consists of 250 points (Y - 10 points, Z - 25 points). The chosen points ranges from 50 to 150 mm off the floor (Y) and from -96.8 to 96.8 mm across the width (Z). The range defined by these points represents an area slightly wider and taller (from bumper height only) than the average vehicle as shown in Fig. 5.11. This setup divides spaces between each flap/grid shaft by 3 in both directions.
2. **High Resolution (HR) Scan** - The HR scan area is represented by the blue box in Fig. 5.11. The high resolution scan consists of 225 points (Y - 15 points, Z - 15 points). The chosen points ranges from 50 to 100 mm off the floor (Y) and from -24.2 to 24.2 mm across the width (Z). The range defined by these points represents a “unit” area for the TGS between two airfoils and two active grid horizontal shafts. The area is centered around  $Y = 75$  mm and  $Z = 0$  mm; this area corresponds to a smaller

area around the hood of the vehicle as shown in Fig. 5.11.

3. **6-Point Scan** - The 6-point scan is represented with red dots shown in Fig. 5.11. The full scans described above consist of many measurement points that significantly increase the measurement time making it difficult to test a variety of test configurations. As such, measurements will be primarily conducted using a set of 6 points in a line at a height of 75 mm off the floor. The points are positioned to avoid the direct wakes of the shafts as shown in Fig. 5.12. Therefore, significantly more TGS test configurations can be tested with the 6-point setup.

An important consideration is to determine the validity of measuring flow data for 6 points only. The validity of using data averaged from the 6 measurement points to represent the flow generated by the TGS is discussed in Chapter 6. Validation is conducted by comparing the flow measured at the 6 points to the LR and HR plane scans.

## 5.7 Baseline and Test Parameters

Two main baseline programs have been defined to be used as a reference to other TGS tests.

The first baseline motor program, MP1, holds the TGS is fully open and stationary, and is the baseline case for comparison. The second baseline motor program, MP2, oscillates the flaps simultaneously at 1 Hz and at  $\pm 10^\circ$ . This program will provide a baseline reference for the oscillation type, frequency and amplitude. Both of these baseline programs were run during every test. Two other variations of

Table 5.2: Baseline testing parameters

Parameter	Specification
MPS	MP1: Fully open MP2: Sine osc. at $\pm 10^\circ$ , 1 Hz MP3: Sine osc. at $\pm 10^\circ$ , 1 Hz + Gusting at 1 Hz MP4: Sine osc. at $\pm 10^\circ$ , 1 Hz + Gusting at 1 Hz + Grid Rotation
Sampling Time	6-point: 60s, Plane: 45s
Freestream Velocity	15 m/s

the baseline case, MP3 and MP4, are also used. These add the gusting and the grid rotation to the baseline

dynamic yaw case. The baseline program specifications are shown in Table 5.2.

In addition to the baseline MPS, several testing parameters were used. Most tests will be conducted at a constant freestream velocity of approximately 15 m/s; this flow velocity magnitude was measured when the TGS is fully open. Other tests that analyze the effect of freestream velocities will test additional flow velocity values (12.5 and 17.5 m/s). The 6-point measurements will be sampled for 60 seconds while plane scans (LR or HR) will be sampled for approximately 45 seconds due to the testing time and size of the collected data. The effect of these sample times on measurement uncertainty will be discussed in Chapter 6.

## **5.8 Test Cases**

All tests cases considered are shown in Table 5.3. The table contains the names, descriptions, specifications and objective of each test. All parameters not shown in the specification column are taken at the reference values described in Table 5.2.

Table 5.3: Summary of test cases.

Name	Objective	Notable Specifications
Static Flap Angles	1.1: Determine the average flow angle generated by static flaps. 1.2: Determine the applicability of the simplified simulations to capture the flap versus flow angle relationship.	Flap Angles ( $^{\circ}$ ): -15, -10, -5, 0, 5, 10, 15
Dynamic Flap Response	2.1: Determine the phase-averaged flow angle created by dynamic flaps at different amplitudes and frequencies.	Flap Angles ( $^{\circ}$ ): 0, $\pm 5$ , $\pm 10$ , $\pm 15$ Flap Freq. (Hz): 0.5, 1, 5, 10, 15
Combining TGS Subsystems	3.1: Determine the distribution of energy in the flow generated by the TGS. 3.2: Compare the yaw performance with and without the active grid.	Gust Freq (Hz): 0.5, 1, 5 H. Grid Rotation: On, Off Flap Freq. (Hz): 0, 0.5, 1, 5, 10
Freestream Velocity	4.1: Understand the effects of changing freestream velocity on yaw performance.	MPS: MP1, MP2, MP4 Freestream Vel. (m/s): 12.5, 15, 17.5
Plane Scans	5.1: Obtain LR/HR contour plots.	MPS: MP1, MP2, MP4 Sample Time (s): 45s
Frequency Scans	6.1: Determine the effect of conducting freq. scans	MPS: MP1, MP2, MP3, MP4 Sample Time (s): 120s

## 5.9 Analysis Methods and Notes

The following section will describe the methods that will be used when analyzing the results.

### 5.9.1 Time Series and Time-Averaging

Time series data is used as an input for advanced methods such as conducting phase-averaged analysis, spectral analysis and for calculating different turbulent characteristics. To prevent inaccuracies due to

filtering, the raw time series is used for all subsequent data processing steps.

Time-averaged data will also be presented in the results. These results simply take the mean of a raw time series to show a variety of results. The error due to taking the mean will also be presented for time-averaged data. Mean errors, calculated with  $E = z\sigma/\sqrt{N}$ , will be calculated with a confidence interval of 99% ( $z = 2.56$ ). The number of independent samples,  $N$ , is calculated through auto-correlation of the raw time series signal to ensure that sampled points are independent of one another. The time between each independent sample is calculated by obtaining the time it takes to reach the first zero crossing of the auto-correlation.

### 5.9.2 Shape of Yaw Distributions

A common method of presenting unsteady yaw performance for existing TGS is through the use of yaw distribution plots. Histogram plots will be provided for certain test configurations using the combined raw time series data for all measurement points considered. The standard deviation and kurtosis of each of the distributions will be denoted by  $\sigma$  and  $K$  respectively. Examples of possible standard deviations of a distribution are shown in Fig. 5.13. Typical values of the standard deviation measured on the road were previously discussed in Section 2.1. Meanwhile, the shape of different values of kurtosis are shown in Fig. 5.14. The kurtosis values will be primarily used to compare the measured distribution to a normal distribution with a kurtosis value of  $K = 3$ . These values are listed in the legend of each plot in this thesis. These plots will be an important aspect when comparing the TGS's performance against existing TGS and on-road conditions.

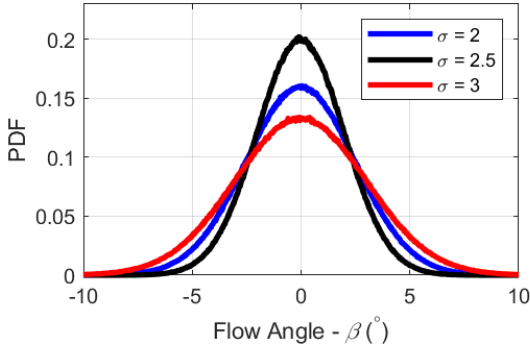


Figure 5.13: Depiction of flow yaw distributions with different standard deviation values and a constant kurtosis value of  $K = 3$ .

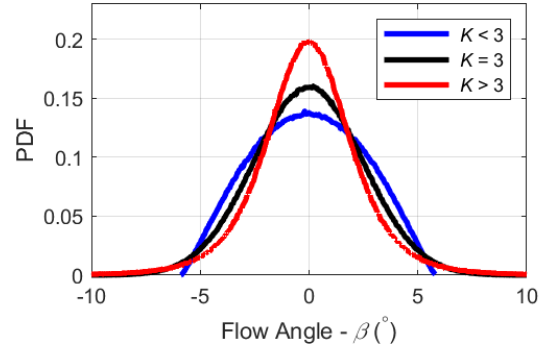


Figure 5.14: Depiction of flow yaw distributions with different kurtosis values and a constant standard deviation value of  $\sigma = 2.5$ .

### 5.9.3 Phase-Averaging

An important analysis method used in this research is phase-averaging. This method involves the use of time series of both the measured flow data and a reference shaft encoder signal sampled in parallel during a flap oscillation test case. Both time series are divided based on flap oscillation cycles using the zero-crossings of the collected encoder signal. Afterwards, these divided cycles are averaged together. The phase-averaging method is demonstrated in Fig. 5.15 and 5.16. In Fig. 5.15, a time series having an underlying sinusoidal component of frequency,  $f$ , is shown over two cycles. The time series is windowed over a duration of  $16/f$  and the local time averaged data at a corresponding phase is ensemble averaged with that of the same corresponding phase in subsequent cycles. In Fig. 5.16, the red dots show the phase averaged data of the first and second cycles. If further cycles were included the distribution of the points would presumably become smoother. It should also be noted that the time series used for this method have no filtering applied.

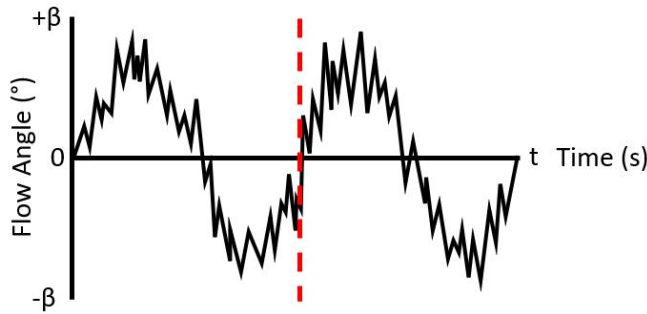


Figure 5.15: Depiction of a raw time series (2 cycles) from an oscillating yaw case. A red line shows where data is cut (zero-crossing) for phase-averaging. The individual cycles are stacked to perform phase-averaging.

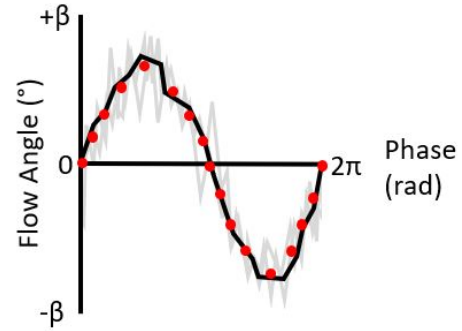


Figure 5.16: Depiction of phase-averaged data over a single phase. The black line represents the phase-average of the stacked time series data shown in gray. The red dots represent windowed phase-averaging data at discrete points.

The resulting data is a phase-averaged plot of the flow data and encoder signal (flap position) over a single cycle; in other words, it shows the average flap angle (from the encoder) and the flow data (velocity or angle) across all collected flap oscillations on a single flap cycle. This method, therefore, makes it possible to determine the phase-averaged flow velocity or angle at any phase of the flap cycle. One of the most important results that can be drawn from this method are plots such as flap angle versus flow angle for any dynamic oscillation test case. This will be referred to as the flap versus flow angle relation moving forward.

Several parameters must be defined when conducting phase-averaging. The important parameters for this method are discussed below.

1. **Phase Bins** - The number of bins across a single cycle must be defined. These bins are equally spaced within a single cycle and represents a local average at defined phases. Phase-averaged data discussed in this paper uses 64 equally spaced bins. An example of these bins are represented by the points shown in Fig. 5.16.
2. **Window Width** - The data width considered for the mean of a phase bin is important for determining

the actual value of the bin. Window widths, or the range of data considered around a bin, are defined by percent overlap with adjacent bins. All phase-averaging results in this paper use a 50% overlap.

- Cross-Correlation Shift** - Phase-averaged plots are expected to show the lag between the encoder signal (flap position) and the measured flow data at the hot-wire as shown with the black dots in Fig. 5.17. The lag value is usually dependent on the freestream velocity and becomes much more apparent for high frequency oscillation cases. Thus, it is often required to line up the signals when plotting results, such as flap angle versus flow angle, to see the direct effect of the oscillations at a later time.

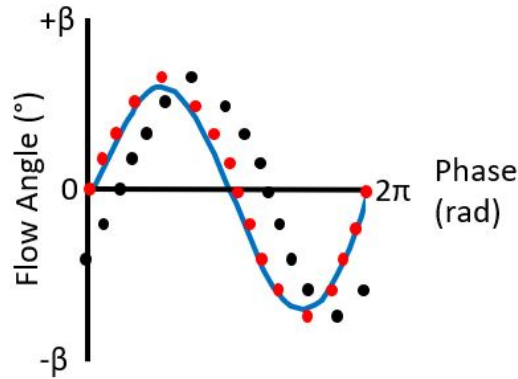


Figure 5.17: Phase-averaged flow angle data with (red) and without (black) cross-correlation shifting compared to the reference phase provided by the encoder.

Cross-correlation is used to line up the encoder and flow data time series as shown with the red dots in Fig. 5.17. This method utilizes the `xcorr` function in MATLAB to determine the lag between both signals. Afterwards, the flow data signal is shifted by the calculated value. An important note to consider is that method removes the real-world lag between the signals, thus making it different from what is actually happening within the test section. Still, having the ability to see the direct effect of the flap oscillation is useful for determining the yaw system performance. All phase-averaged plots in this paper will indicate whether or not cross-correlation shifting (referred to as `xcorr`) was used.

Phase-averaging is also applied in two different ways depending on the analysis being performed. Normally, phase-averaging is conducted for a single point only. However, given that tests include multiple points

as described in Section 5.6, the spatially averaged flow data across all points is often considered. Spatially averaging the flow data involves taking the phase-averaged data or cycle for each measurement point then averaging all of their corresponding phase bins together.

#### 5.9.4 Spectra

Flow spectra is an important tool to determine the flow's energy distribution across a range of frequencies. MATLAB's `pwelch` function is used in this thesis to determine the power spectral density (PSD) plots for any of the test cases. Two power spectral density plots will be presented based on the streamwise ( $u$ ) and spanwise ( $v$ ) velocity component time series. The velocity component means ( $\bar{u}$  or  $\bar{v}$ ) are used to obtain the fluctuations ( $u' = u - \bar{u}$  or  $v' = v - \bar{v}$ ) of the velocity components. Afterwards, the fluctuations are normalized by the mean freestream velocity,  $U$ .

### 5.10 Measurement Uncertainties

Possible areas of uncertainties due to measurement or testing equipment are discussed in this section. The uncertainties affecting the measured flow angle and velocity are considered in this discussion. Afterwards, the effects of post-processing steps on measurement accuracy, such as taking averages, are presented.

#### 5.10.1 Cross-Wire Measurement Uncertainty

Flow yaw and velocity are obtained with the cross-wire probe using a variety of measurement equipment, each with their own uncertainties, during calibrations. The equipment used during calibrations have been discussed previously in this Chapter. Uncertainties due to the traverse position and hotwire equipment are neglected. Therefore, errors due to the reference velocity measurement (pressure probe) and temperature compensation are considered when obtaining the cross-wire flow velocity and angle calibration surfaces as described in Section 5.5.3.

The flow velocity magnitude from the pressure probe,  $U_P$ , can be calculated with the pressure and air

density as described in Section 5.3.1. Assuming variable pressures and temperatures, the pressure probe flow velocity can be calculated with  $U_P = \sqrt{2RPT/P_{atm}}$ , where  $R$  is the gas constant (286.9 J/kgK),  $P$  is the measured differential pressure (kPa),  $T$  is the measured temperature (K) and  $P_{atm}$  is the atmospheric pressure (assume average of 101.7 kPa during testing). Assuming both pressure and temperature have random independent errors of  $\delta P = \pm 1.25$  Pa (0.25% of 500 Pa) and  $\delta T = \pm 1^\circ\text{C} = \pm 1$  K (T-type probe) respectively, the total pressure probe velocity error,  $\delta U_P$ , can be calculated using the general error formula commonly found in literature [26].

$$\delta U_P = \sqrt{\left(\frac{\partial U_P}{\partial P} \delta P\right)^2 + \left(\frac{\partial U_P}{\partial T} \delta T\right)^2} = \sqrt{\left(\frac{RT}{2P_{atm}P}\right) \delta P^2 + \left(\frac{RP}{2P_{atm}T}\right) \delta T^2} \quad (5.1)$$

Assuming an average flow temperature of  $T = 20^\circ\text{C}$  and a known flow velocity of  $U_P = 15$  m/s, or  $P = 136$  Pa, the total error can be calculated as  $\delta U_P = 0.074$  m/s. Therefore, the error due to the pressure probe velocity is less than 1% of the expected test velocity and was deemed acceptable for this experiment.

Another source of uncertainty is the error due to fitting measured cross-wire data onto the flow velocity and angle calibration surfaces. Analysis of the fitting error was conducted by calculating the RMSE across all 81 calibration points (known flow velocity and angle) using the constructed calibration surfaces; the voltage data from these points were used to obtain the calculated flow velocity and angle for error comparison. Furthermore, the RMSE was calculated with both the initial and final calibrations for each data set. The analysis showed that the RMSE values were less than  $0.02^\circ$  for the flow angle and 0.1 m/s for the flow velocity.

The total error due to the entire calibration process can be determined by combining all individual errors. Three main sources exist for the calibration process. First, the reference velocity error,  $\delta U_P = 0.074$  m/s, was determined based on the accuracy of the pressure probe and thermocouple. The reference velocity was then used to construct the flow velocity calibration surface. Thus, any values velocity values calculated from the surface have an inherent error equal to  $\delta U_P$ ; it should be noted that this only applies to the flow velocity surface because the flow angle calibration surface was constructed using known traverse angles with no

significant error. Next, the uncertainty associated with the surface fit to the calibration points are shown to create errors of  $\delta U_S = \pm 0.1$  m/s and  $\delta \beta_S = \pm 0.02^\circ$  for the flow velocity and angle respectively. Finally, errors between the initial and final calibrations have been discussed in Section 5.5.3 with values of  $\delta U_C = \pm 0.07$  m/s and  $\delta \beta_C = \pm 0.10^\circ$  for the flow velocity and angle respectively. Therefore, the error for the hot-wire flow velocity ( $U$ ) and flow angle ( $\beta$ ) prior to any post-processing are  $\delta U = \sqrt{\delta U_P^2 + \delta U_S^2 + \delta U_C^2} = \pm 0.14$  m/s and  $\delta \beta = \sqrt{\delta \beta_S^2 + \delta \beta_C^2} = \pm 0.10^\circ$ .

### 5.10.2 Phase-Averaging Uncertainty

Obtaining phase-averaged yaw data requires three averaging operations. First, the total number of cycles in the time series,  $N_\phi$ , can be used in with the standard deviation of all data at the same phase,  $\sigma_\phi$ , to determine the error due to averaging over cycles,  $\delta \beta_\phi$ , using the standard error formula,  $\delta \beta_\phi = \sigma_\phi / \sqrt{N_\phi}$ . Secondly, the yaw error due to windowing,  $\delta \beta_W$ , at each phase can be determined with  $\delta \beta_W = \sigma_W / \sqrt{N_W}$  where  $\sigma_W$  is the standard deviation of the data within the window and  $N_W$  is the number of independent points within the window. Finally, the average over 6 points can then be determined using  $\delta \beta_6 = \sigma_6 / \sqrt{N_6}$  for each window. Given average values of  $\delta \beta_\phi = \pm 0.297^\circ$ ,  $\delta \beta_W = \pm 0.018^\circ$ , and  $\delta \beta_6 = \pm 0.173^\circ$  used in this research, the total error after post-processing,  $\delta \beta_T$ , can be estimated with  $\delta \beta_T = \sqrt{\delta \beta_\phi^2 + \delta \beta_W^2 + \delta \beta_6^2 + \delta \beta^2} = \pm 0.36^\circ$ .

## 6 Results and Discussion

In this chapter, the results pertaining to the cases described in Section 5.8 are presented. The choice of sample time and representative measurement points is first discussed in Section 6.1. In Section 6.2, the performance of the yaw system is analyzed first when operating at fixed of steady conditions. Next, an analysis the yaw system under dynamic operating conditions is given in Section 6.3. Finally, a summary of the results and a comparison to on-road measurements are given in Sections 6.4 and 6.5 respectively.

### 6.1 Test Parameter Validation

In the following subsections the validation of sampling time and a reduced set of representative measurement points is given.

#### 6.1.1 Sampling Time Validation

An important validation step is to ensure that data has been sampled long enough such that results no longer change significantly at higher sampling times. As such, results at different sampling times, between 30 to 150 seconds, have been presented in Fig. 6.1. It should be noted that the plots are created with truncated data from the same measurement set (total 180 seconds). The plots show that there are no significant differences between the tested sampling times for the 6-point baseline (MP2) test. Quantitatively, additional analysis was conducted on determining the error due to taking an average over cycles,  $\delta\beta_\phi$ , since the sampling time is directly related to the number of independent cycles within the time series. The results of this analysis is shown in Fig. 6.2.

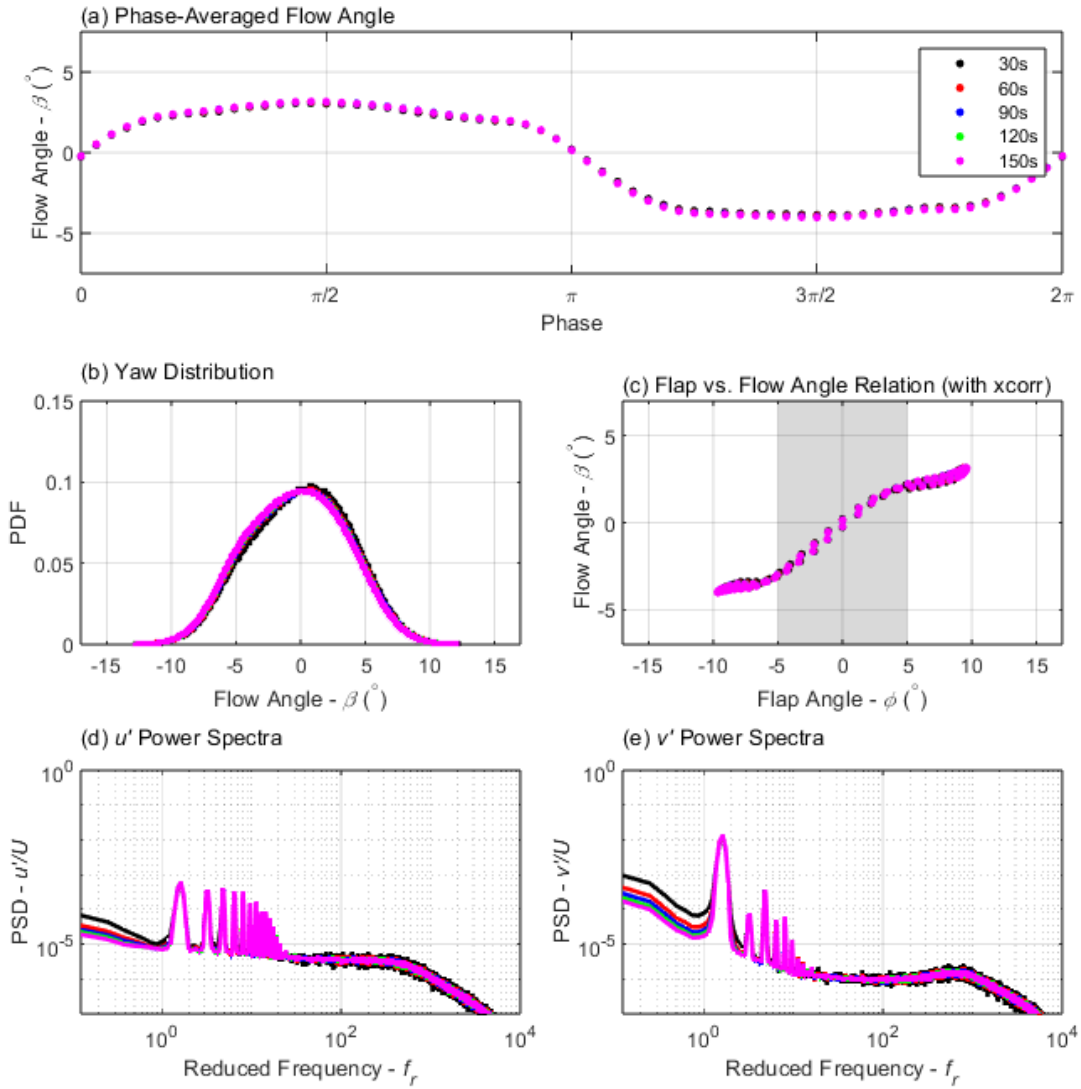


Figure 6.1: Baseline oscillation (MP2, sinusoidal flap oscillation at 1 Hz and  $\pm 10^\circ$ ) plots taken at different sampling times from 30 to 150 seconds as shown in the legend. The results shown are the spatially averaged using 6 points and with a freestream velocity of  $U = 15$  m/s.

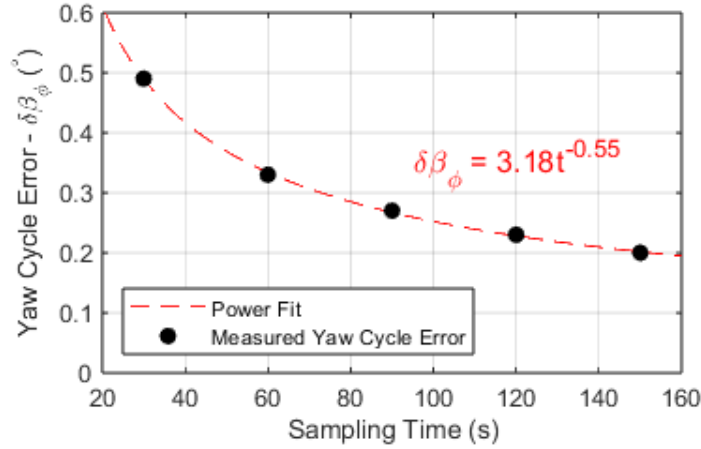


Figure 6.2: The error due to taking an average over cycles shown with baseline oscillation case (MP2, sinusoidal flap oscillation at 1 Hz and  $\pm 10^\circ$ ) taken at different sampling times. The equation of the fit is also provided.

### 6.1.2 6-Point Measurement Validation

Validation for the chosen 6-point scan, as described in Section 5.6, was conducted to ensure that these points were sufficiently representative of the average flow going over the vehicle. Figure 6.3 shows that a large variation of yaw angles (between  $\beta = 2^\circ$  to  $4.3^\circ$ ) were measured across the nozzle plane for the LR plane scan (black points). These variations were primarily due to the presence of wakes generated by the active grid elements/shafts and airfoils. The average flow over a vehicle, or the average of the LR and HR plane scans, was considered to account for spatial variations of yaw over the nozzle and will be referred to as the reference scan in this section. The reference phase-averaged flow angle cycle is obtained by taking the average of both the LR and HR phase-averaged flow angle cycles at each respective phase.

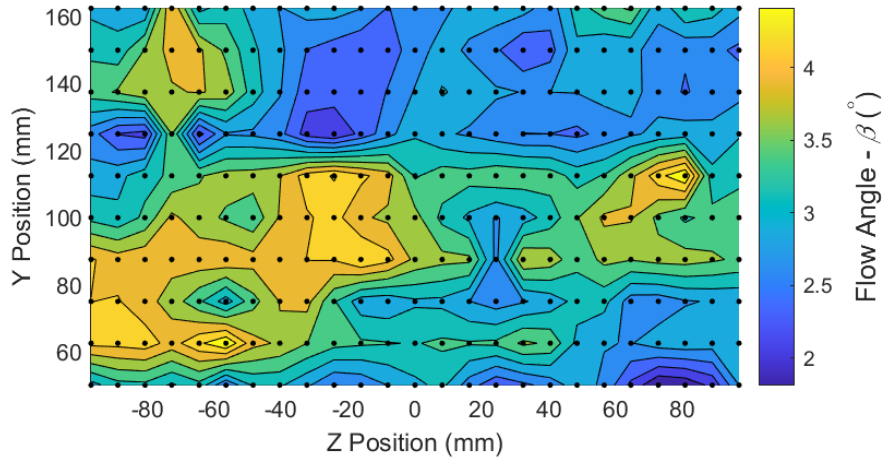


Figure 6.3: Contour plot of the phase-averaged flow angle,  $\beta$ , at the LR measurement plane (black dots) located at  $X = 250$  mm from the grid. The baseline yaw oscillation case (MP2, sinusoidal flap oscillation at 1 Hz and  $\pm 10^\circ$ ) and a freestream velocity of  $U = 15$  m/s was tested. An instantaneous flap angle of  $10^\circ$  is shown in this figure.

Comparisons were made between the reference and 6-point phase-averaged flow angle cycles as shown in Fig. 6.4. The plot shows that phase-averaged results for both measurement point configurations are in close agreement with one another. The RMSE between the 6-point and reference cycle was determined to be  $0.126^\circ$  which is deemed acceptable for this research. Therefore, the 6-point scan can be used to determine the flow angle for a wide range of test cases.

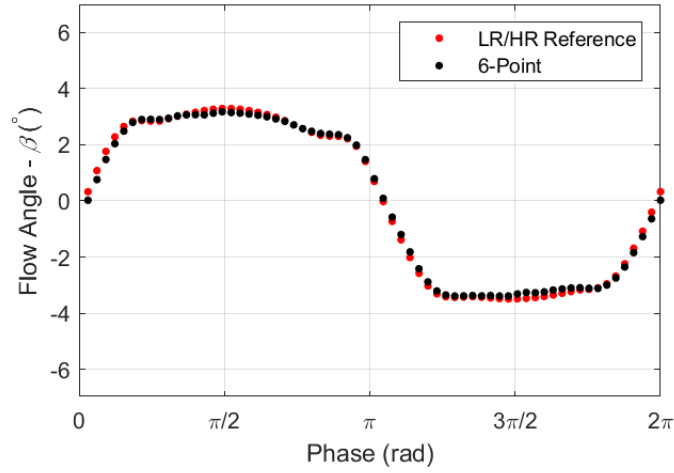


Figure 6.4: Comparison of the flow angle,  $\beta$ , versus the phase of the turning vanes for the 6-point and LR/HR reference plane measurement point configurations. All configurations use a baseline oscillation case (MP2, sinusoidal flap oscillation at 1 Hz and  $\pm 10^\circ$ ) with a freestream velocity of  $U = 15$  m/s.

## 6.2 Static Yaw Performance

Yaw system performance was tested using static flap angles. The flaps were held at static flap angles from  $\phi = -15^\circ$  to  $15^\circ$  in intervals of  $5^\circ$ . All points are tested with a freestream velocity of  $U = 15$  m/s. The resulting time-averaged flow angles with respect to the known flap angles are shown in Fig. 6.5(a).

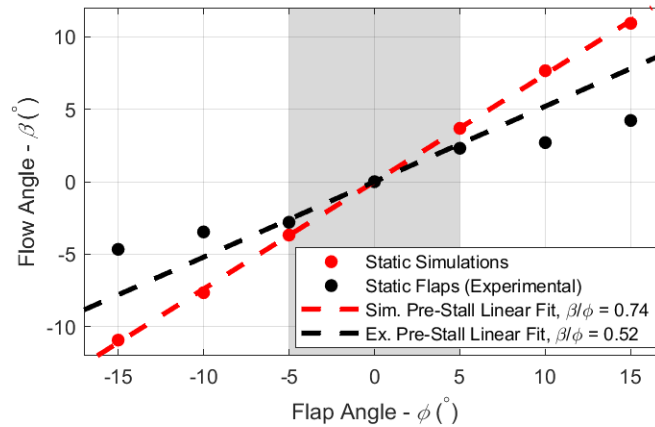


Figure 6.5: Comparison of the flow angle,  $\beta$ , and flap angle,  $\phi$ , for the static simulations and the experimental static test cases.

The data collected from the static flaps test shows a large yaw performance difference when compared to the simulated results. Figure 6.5 shows that for small flap angles between  $\phi = \pm 5^\circ$ , the relationship between the flap and flow angles follows a slope of approximately  $\beta/\phi = 0.52$ . On the other hand, the simulations predicted a value of approximately  $\beta/\phi = 0.74$ . In addition, there is a distinct change in the slope at the flap angles greater in magnitude than  $\phi = \pm 5^\circ$ . The slope of  $\beta/\phi$  decreases significantly and a maximum mean flow angle of approximately  $\beta = \pm 4.5^\circ$  is achievable from the TGS for  $\phi = \pm 15^\circ$ . Therefore, the static response of the system is not performing as expected based on the original simplified simulation performed for the isolated turning vanes results during the conceptual design phase. The possible causes for these differences have been discussed previously in Section 3.4.3 and are later discussed with new experimental data in Appendix A. It is shown in Appendix A that the active grid system effects the yaw system. However, the current active yaw system is able to meet performance targets as shown in the following sections and the final comparisons to on-road measurements.

### 6.3 Dynamic Simultaneous Yaw Performance

The following section contains the collected results for all of the different dynamic test cases that were conducted. Each subsection will analyze the effect of a different TGS operation parameter (flap amplitude, flap frequency, oscillation shape, freestream velocity etc.) on yaw performance. Subsection 6.3.2 and onwards will present the same set of 8 plots that were used to draw insight on the effects of each operation parameter. These plots range from phase-averaged velocity components, yaw distributions, flap versus flow angle performance (pre-stall region shaded in gray) and power spectra. Each respective plot have constant axis limits across all operation parameters that were analyzed for ease of comparison. Finally, the analysis of each data set will typically go through discussion on the flap versus flow angle performance, effects on the yaw distribution and, finally, the effects on the power spectra. All results presented in this section are spatially averaged across the 6-point scan.

### 6.3.1 Static, Dynamic and Simulation Oscillation Comparisons

The difference between static and dynamic tests were analyzed. Figure 6.6 shows a comparison between a dynamic (sinusoidal flap oscillation at 1 Hz and  $\pm 15^\circ$ ), static and simulated yaw performance results at a constant freestream velocity of  $U = 15$  m/s.

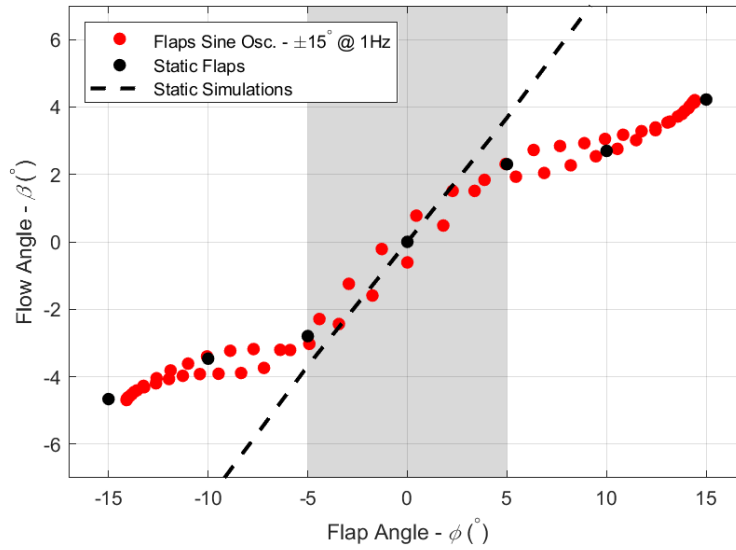


Figure 6.6: Variation of the measured flow angle with respect to the yaw system flap angle. The dashed line shows the result from the simulation. Data markers show the results from the static experiment and one representative experiment having oscillating yaw (sinusoidal flap oscillation at 1 Hz and  $\pm 10^\circ$ ).

Fig. 6.6 shows that both the static and dynamic experimental tests are in close agreement with one another. Both the static and dynamic tests are observed to follow the same linear flap versus flow angle relation with a slope of approximately  $\beta/\phi = 0.52$  within  $\phi = \pm 5^\circ$ . Likewise, a sudden change in flow yaw performance is observed after flap angles of  $\phi = \pm 5^\circ$  indicating yaw performance stall for both cases. Although the dynamic test also shows significant hysteresis in the the flap versus flow angle relation, the static flap results are generally representative of the average of the loop across most flap angles. As with the static test, Fig. 6.6 also shows that the dynamic oscillations do not match the simulated results.

### 6.3.2 Effect of Oscillation Amplitude

Results pertaining to the effect of oscillation amplitude are shown in Fig. 6.7 for three cases where  $\phi = \pm 5^\circ, \pm 10^\circ, \pm 15^\circ$ . The data was taken at a constant flap frequency of  $f = 1$  Hz and freestream velocity of  $U = 15$  m/s. Figure 6.7 subfigures show the phase and 6-point spatially averaged (a) u flow velocity, (b) v flow velocity and (c) corresponding flow angle. The 6-point spatially averaged yaw distribution is shown in (d). The relation between flow and flap angle is shown in (e) and (d) before and after the cross-correlation shifting. The 6-point spatially averaged power spectra is shown in (g) and (h) for streamwise and spanwise components respectively.

Fig. 6.7(f) compares the flap versus flow angle relations for different dynamic oscillation amplitudes considered. All three cases show that the flow continues to follow a linear relation between  $\phi = \pm 5^\circ$  with a slope of  $\beta/\phi = 0.52$ . Likewise, all cases appear to behave similarly after  $\phi = \pm 5^\circ$ . On the other hand, the main difference between the different cases is the maximum achievable phase-averaged flow angle; the plot shows that increasing the oscillation amplitude increases the measured flow yaw.

The yaw distributions show a significant difference between the cases considered. Increasing the flap oscillation amplitude appears to increase the standard deviation, decrease the kurtosis, decrease the PDF peak and widen the overall distribution. Furthermore, large amplitudes, such as the  $\phi = \pm 15^\circ$  case, appear to show the development of a bimodal distribution with approximate flow angle peaks at around  $\beta = \pm 3^\circ$ . The yaw distribution behavior can be explained by two possible causes. First, the results in Fig. 6.7(c) and 6.7(f) show that system has a change in yaw performance at flap angles of around  $\phi = \pm 5^\circ$  or flow angles of  $\beta = \pm 3^\circ$  which can be related back to the development of bimodal peaks at the same yaw angles; the yaw no longer increases as significantly after  $\phi = \pm 5^\circ$ , thus adding more weight to the tails of the distribution and creating mean peaks at the appropriate flow angles. Another possible cause of the increasing kurtosis is the possibility of airfoil stall and, therefore, increased presence of wakes; the potentially stalled airfoils acts as bluff body drag elements that generates a larger range of high angle and frequency flow yaw structures, thus reducing the zero mean peak and widening the distribution further. Therefore, the yaw distribution is

significantly affected by the changing oscillation amplitude.

The PSD plots shown in Fig. 6.7(g) and 6.7(h) show that oscillation amplitude has minor effects on the flow spectra. All three cases have similar peak frequencies and harmonics but have slightly larger magnitudes for increasing flap amplitudes. Another observation is that larger flap amplitudes tend to have more prominent odd harmonic peaks; this is evident in Fig. 6.7(h) and indicates that the flow yaw response from the system is not perfectly sinusoidal, but rather closer to a square wave due to stall after  $\phi = \pm 5^\circ$ .

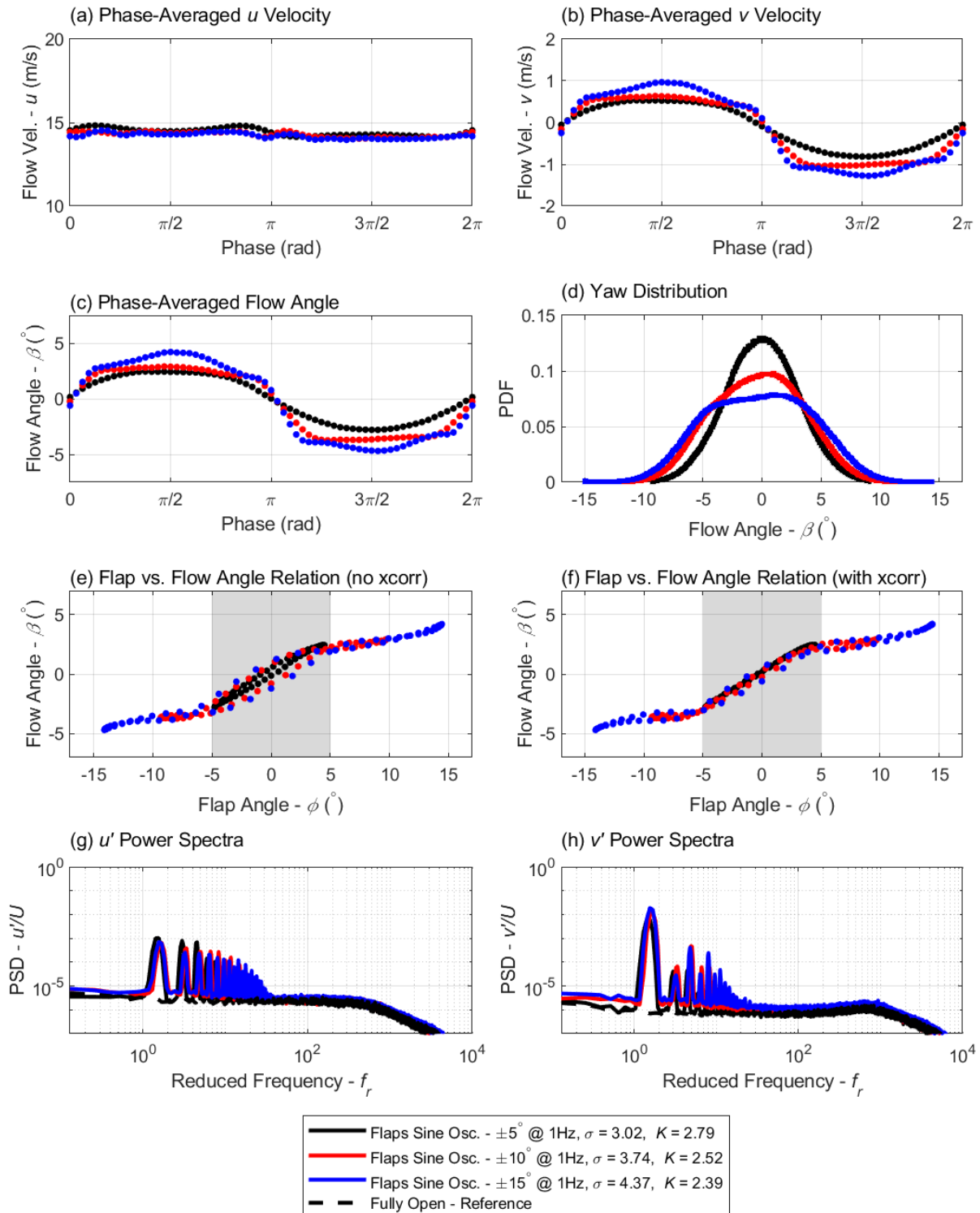


Figure 6.7: Selected sinusoidal flap oscillation amplitude cases ( $\phi = \pm 5^\circ, \pm 10^\circ, \pm 15^\circ$ ) at  $f = 1$  Hz.

Subfigures are explained in the text of the corresponding section.

### 6.3.3 Effect of Oscillation Frequency

The effect of oscillation frequency was analyzed and the results are shown in Fig. 6.8 for five cases where  $f = 0.5, 1, 5, 10, 15$  Hz. The data was taken at a constant flap amplitude of  $\phi = \pm 10^\circ$  and freestream velocity of  $U = 15$  m/s. Figure 6.8 subfigures contain the same set of plots and order as Fig. 6.7.

The flap frequency results show that there is no significant effect on the resulting flap versus flow angle relations as shown in Fig. 6.8(f). The most notable difference, however, is the slight increase of maximum yaw angle achievable as flap frequency increases. A possible explanation for this behavior can be seen in Fig. 6.8(c); the flow angle appears to overshoot prior to changing the flap direction at higher oscillation frequencies due to increased energy input from the motors. Additionally, this may also explain the slight change in the shape of the flap versus flow angle relation in Fig. 6.8(f); increasing flap frequency appears to create a more linear flap versus flow angle relation with increasing hysteresis due to the overshoot prior to changing flap directions (continues momentarily with slope of  $\beta/\phi = 0.52$ ). Still, no strong conclusions can be drawn from this result. However, an important result to note is the consistent yaw performance change typically around  $\phi = \pm 5^\circ$ ; this result is consistent with all flap frequencies.

The yaw distribution of the collected data in Fig. 6.8(d) shows only minor differences between the chosen cases. The yaw distribution plot shows that increasing the flap frequency slightly increases the standard deviation and decreases the kurtosis of the system; the peak appears to reduce slightly with increasing frequency. Again, this is potentially due to the fact that higher frequency oscillations inject more energy into flow, thus generating slightly larger flow angles as previously discussed.

Finally, significant changes to the PSD plots have been observed. The spectral peaks have been shown to shift according to the oscillation frequency. Likewise, the appropriate harmonics are also evident in the plots due to the fact that the phase-averaged cycle shapes, as shown in Fig. 6.8(c), are not perfectly sinusoidal as discussed in the previous section; the cycle shape typically resembles a square waveform due to stall after  $\phi = \pm 5^\circ$  but can also appear as a sawtooth waveform (prominent integer harmonics) at higher oscillation frequencies due to the previously discussed yaw angle overshoot.

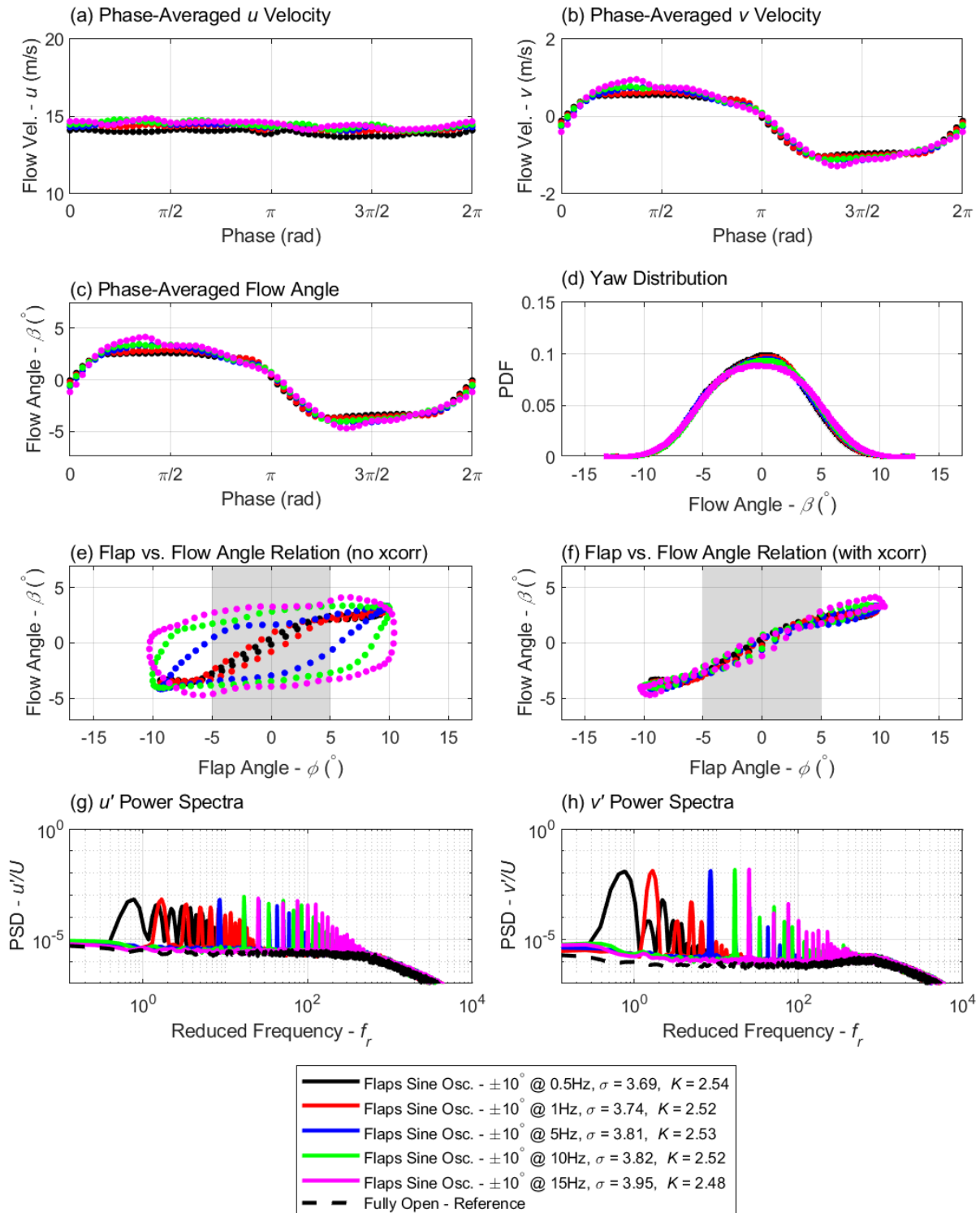


Figure 6.8: Selected sinusoidal flap oscillation frequency cases ( $f = 0.5, 1, 5, 10, 15$  Hz) at  $\phi = \pm 10^\circ$ . Subfigures are explained in the text of the corresponding section.

### 6.3.4 Effect of Freestream Velocity

Figure 6.9 shows the effect of freestream velocity for three cases where  $U = 12.5, 15, 17.5$  m/s. The data was taken at a constant flap frequency of  $f = 1$  Hz and flap amplitude of  $\phi = \pm 10^\circ$ . Figure 6.9 subfigures contain the same set of plots and order as Fig. 6.7.

The results show that freestream velocity has two main effects on the yaw performance. First, Fig. 6.9(c) and 6.9(f) shows that larger phase-averaged peak flow angles can be achieved with higher velocities. Secondly, Fig. 6.9(f) appears to show that higher freestream velocities tend to straighten and create a much more linear flap versus flow angle relation. These observations can, again, be possibly explained by the increased energy in the flow. Despite the differences, however, all three cases show that the flap versus flow angle relation appears to follow the same linear behavior with a slope of  $\beta/\phi = 0.52$  within  $\phi = \pm 5^\circ$ .

Fig. 6.9(d) shows that changing freestream velocities has a noticeable effect on the yaw distribution shape. Increasing the freestream velocity increases the standard deviation and decreases the kurtosis of the system. Another noticeable observation is the development of bimodal peaks for the high velocity case. This behavior can be explained by the observation that higher freestream velocities are able to generate larger yaw angle peaks, thus adding more weight to the tails of the distribution.

Finally, the tested freestream velocities appear to have no effect on the flow spectra peak magnitudes. Figure 6.9(g) and 6.9(h) show that all three cases are in agreement with one another and that no significant effects can be observed for the peaks themselves. However, a reduced frequency shift is noticeable with changing wind tunnel speeds. This occurs due to the fact that the reduced frequency is inversely proportional to the freestream velocity. Thus, increasing velocity shifts the spectra towards the left.

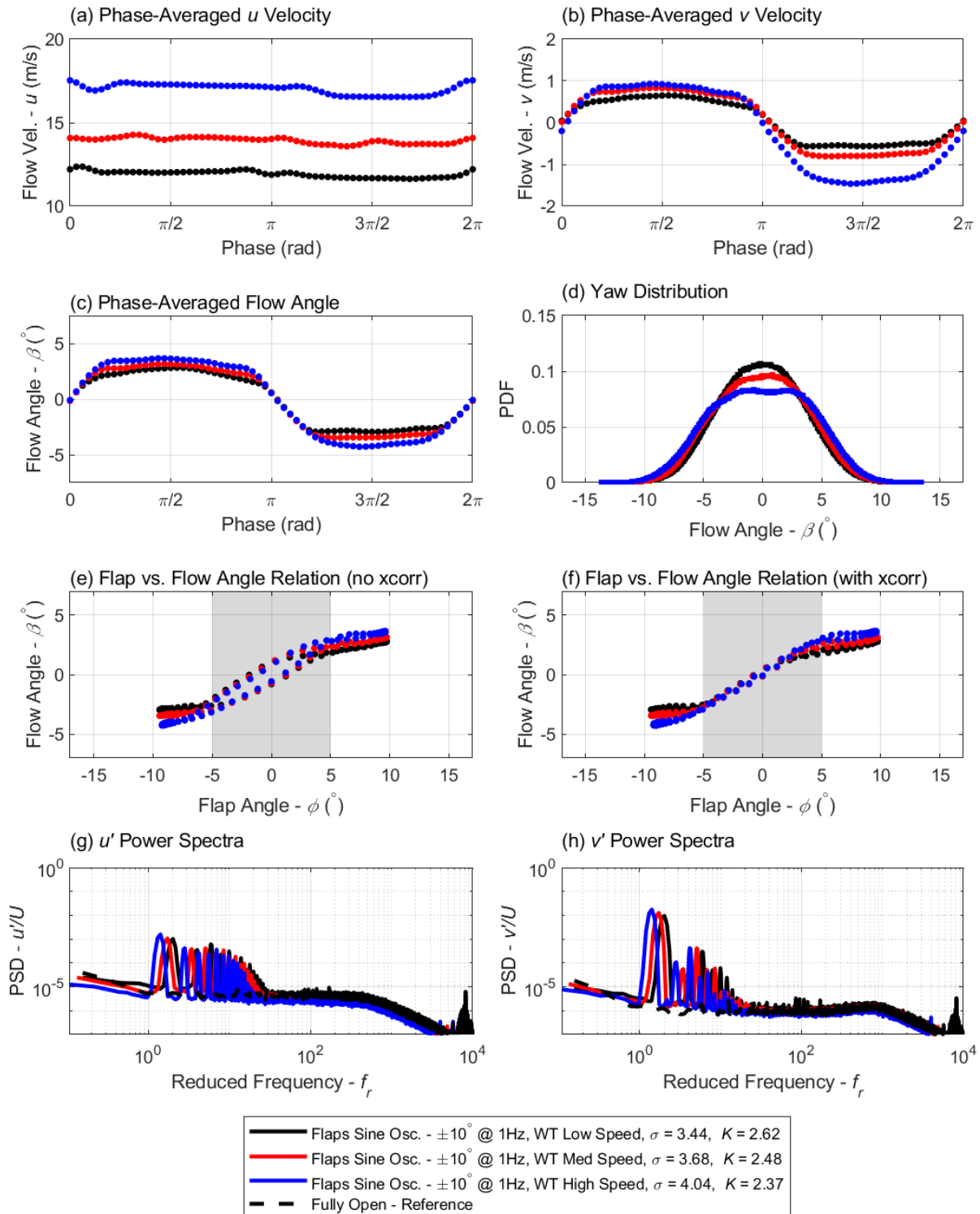


Figure 6.9: Selected freestream velocity cases ( $U = 12.5, 15, 17.5$  m/s) at  $f = 1$  Hz and  $\phi = \pm 10^\circ$ . Subfigures are explained in the text of the corresponding section.

### 6.3.5 Effect of Special Oscillation Cases

The effect of three different oscillation shapes was examined, including sinusoidal, triangle and step oscillations. The results of this analysis are shown in Fig. 6.12. The data was taken at a constant flap frequency of  $f = 1$  Hz, flap amplitude of  $\phi = \pm 10^\circ$  and freestream velocity of  $U = 15$  m/s. Figure 6.12 subfigures contain the same set of plots and order as Fig. 6.7.

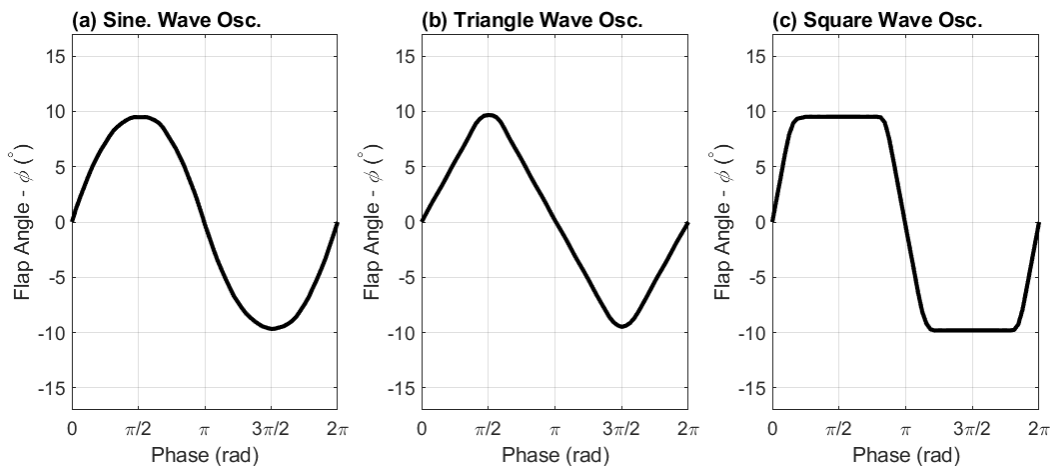


Figure 6.10: Phase-averaged flap position example for three different oscillation shape cases.

The most significant differences between the oscillation cases are observed with the flow yaw distribution shown in Fig. 6.12(d) and the phase-averaged comparisons in Fig. 6.12(c) and 6.12(f). These results indicate that flaps oscillating with a triangular wave pattern are able to most replicate a sinusoidal flow response along with a normal yaw distribution. Likewise, the triangle flap oscillation also shows the least hysteresis indicating a consistent flow yaw response as the flap moves back and forth in either direction. However, there is no significant differences between the overall shape of the flap versus flow angle relation, including the peak yaw angle, stall angle and the slope, for the three different oscillation shapes. The main difference is that the phase bins of the triangular oscillation are distributed evenly across the flap versus flow angle plot while the sinusoidal and square waves are more dense at the peak angles due to passing  $\phi = \pm 5^\circ$  much earlier as per Fig. 6.12(c). Therefore, these results suggest that flaps oscillating in triangle waveform are best able to produce the most consistent and predictable flow yaw response.

Another interesting observation from Fig. 6.12(c) is the yaw response time differences between the three oscillation types. Flaps oscillating in a square wave have the fastest response time, allowing the flow yaw to sit within the stall region after  $\phi = \pm 5^\circ$  for a longer period of time. Accordingly, the yaw distribution for this case show decreased kurtosis due to the increased proportion of stalled flow within single phase. On the other hand, flaps oscillating in a triangle wave show the slowest flow yaw response. Because of this, the flow response for the triangle wave case has the shortest proportion of stalled flow and thus more closely replicates the normal flow yaw distribution observed on the road. The flow yaw response observations from this test can thus be used to tune the flow yaw response behavior when replicating real world yaw time series.

The PSD plots show that the oscillation shape has no significant effect on the spectra other than peak magnitudes. Figure 6.11 shows the v-component spectra for the different shapes that were tested. All three cases have similar frequency peaks but slightly differ in their magnitude. The most notable difference is between the triangle and square wave oscillations.

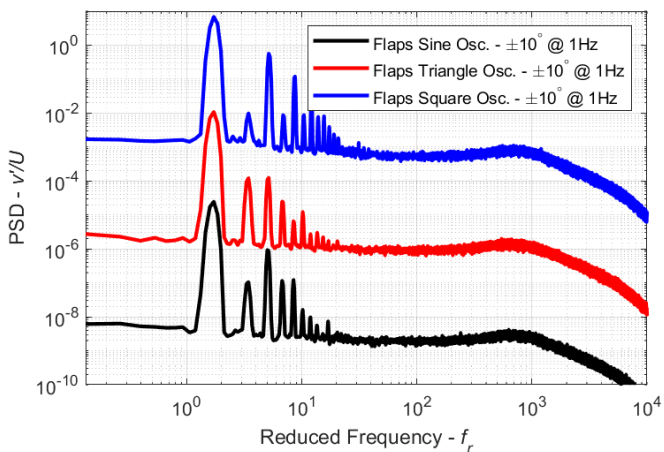


Figure 6.11: Spectra of  $v'$  normalized by the mean flow velocity  $U$  the three different oscillation wave shapes (spectra is shifted vertically by a decade for clarity).

the large portion of yaw stall regions within a cycle. On the other hand, the triangle wave has decreasing peaks at integer harmonics indicating that the flow response is not perfectly sinusoidal but rather more of a sawtooth. Meanwhile, the sinusoidal flap oscillation falls in between these two cases. Nevertheless, these differences are minor and no further conclusions can be drawn due to strong similarities between the cases.

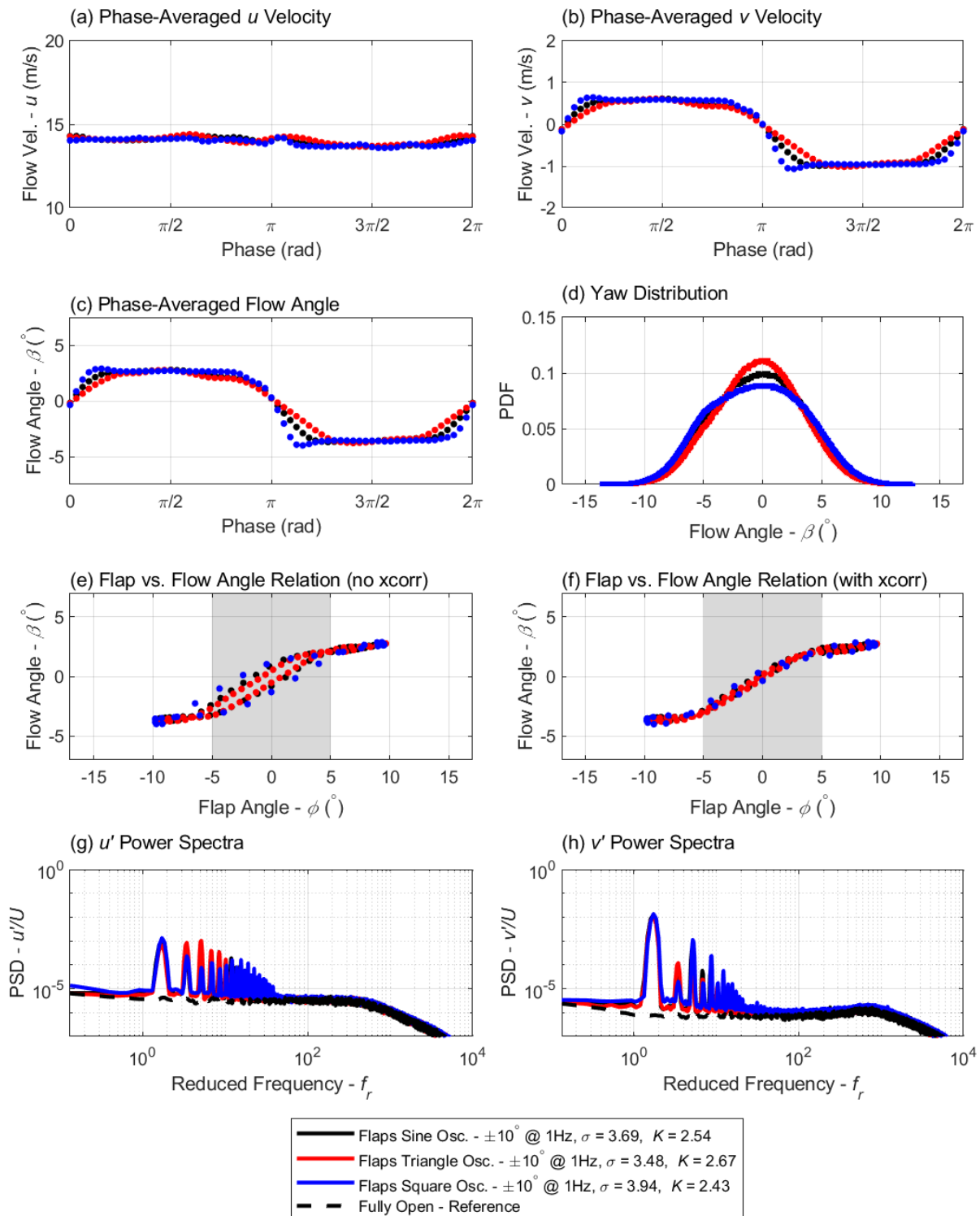


Figure 6.12: Selected oscillation shape cases at  $f = 1$  Hz and  $\phi = \pm 10^\circ$ . Subfigures are explained in the text of the corresponding section.

### 6.3.6 Effect of the Active Grid

The effect of adding the active grid and gusting system on yaw performance was examined and the results are shown in Fig. 6.13. The effect of flap frequency ( $f = 0.5, 1, 5, 10$  Hz) with the grid running was also considered as shown in Fig. 6.14. The horizontal active grid shafts were set to rotate (referred to as “H. Grid Rotation”) at randomly changing speeds of 1 - 10 rps and were set to switch directions and speed every 4 seconds. The gusting system was used to change the blockage of the nozzle between 27% (fully open) to 45%, using a step oscillation with an amplitude of  $90^\circ$  (open/close) and frequencies of 0.5, 1, and 5 Hz as shown in Fig. 6.15. The data was taken at a constant freestream velocity of  $U = 15$  m/s. Figures 6.13, 6.14, and 6.15 subfigures contain the same set of plots and order as Fig. 6.7.

The effect of adding each of the TGS subsystems were examined and the results are shown in Fig. 6.13. The yaw, gusting and active grid subsystems were tested separately first and then together. Baseline MPS specifications were used as described previously in Table 5.2. Phase-averaged results for the gusting and grid only case is not shown due to having no reference encoder signal available.

Several differences can be observed between the yaw performance of the different test cases presented. Figure 6.13(a) shows that the addition of the active grid reduces the mean streamwise flow velocity of the system. This can be attributed to the fact that the active grid rotation creates a blockage across the nozzle leading to fan stall and a reduction in volumetric flow rate. Figure 6.13(c), 6.13(d) and 6.13(f) show a significant difference between the yaw performance of the different cases. The yaw distribution shows that the active grid can be used to create a wider range of yaw angles, significantly increasing the standard deviation, compared to the yaw subsystem alone and brings it much closer to a normal distribution ( $K = 3$ ) as found on the road. However, it should be noted that these high angle yaw flow structures are generated due to the medium to high frequency wakes created by the active grid rotation. Therefore, although it appears that the active grid completely dominates yaw generation as per Fig. 6.13(d), the phase-averaged results show that the bulk and low frequency yaw is still being generated from the yaw subsystem. The addition of the active grid also appears increase the yaw stall angle of the flaps, allowing the flap versus

flow angle relation to appear much more linear. Furthermore, it is also observed that the active grid reduces the slope of the flap versus flow angle relation to approximately  $\beta/\phi = 0.36$  compared to the pre-stall flap versus flow angle performance of the yaw system alone at  $\beta/\phi = 0.52$ . The observed peak yaw angles for the combined yaw and active grid case are also slightly higher compared to the baseline case. This may be due to the presence of the high angle flow structures, generated by the active grid, bringing up the mean yaw angle. Thus, it is evident that the addition of the active grid has a significant effect on the overall yaw performance of the system.

The spectra plots shown in Fig. 6.13(g) and 6.13(h) show the TGS's ability to target different frequency regions in both the streamwise and spanwise directions. The plots show that the yaw system completely dominates the generation of low frequency spanwise turbulence while lacking performance in generating medium to high frequency turbulence in both directions. On the other hand, the gusting system dominates the low frequency streamwise turbulence generation. Meanwhile the active grid rotations shows strong broadband turbulence generation. The difference between these three systems allows the TGS, as a whole, to target all regions of the spectra; in fact, the combined case presented in these plots appears to be a superposition of the individual performances of each of the TGS subsystems. This observation is significant because it shows that the spectral performance of each system can possibly be added to one another to fully replicate a wide range of spectral plots created using data taken from on-road testing.

Figure 6.14 and 6.15 show the effect of changing the operation frequency of the yaw and gusting system respectively. The plots show that there is no significant change in the yaw system performance when changing the operation frequency of the TGS as shown by the phase-averaged cycle and yaw distribution plots. The only difference is observed in the spectral plots; the gusting system shifts the streamwise energy according to its operation frequency while the yaw system shifts the spanwise component.

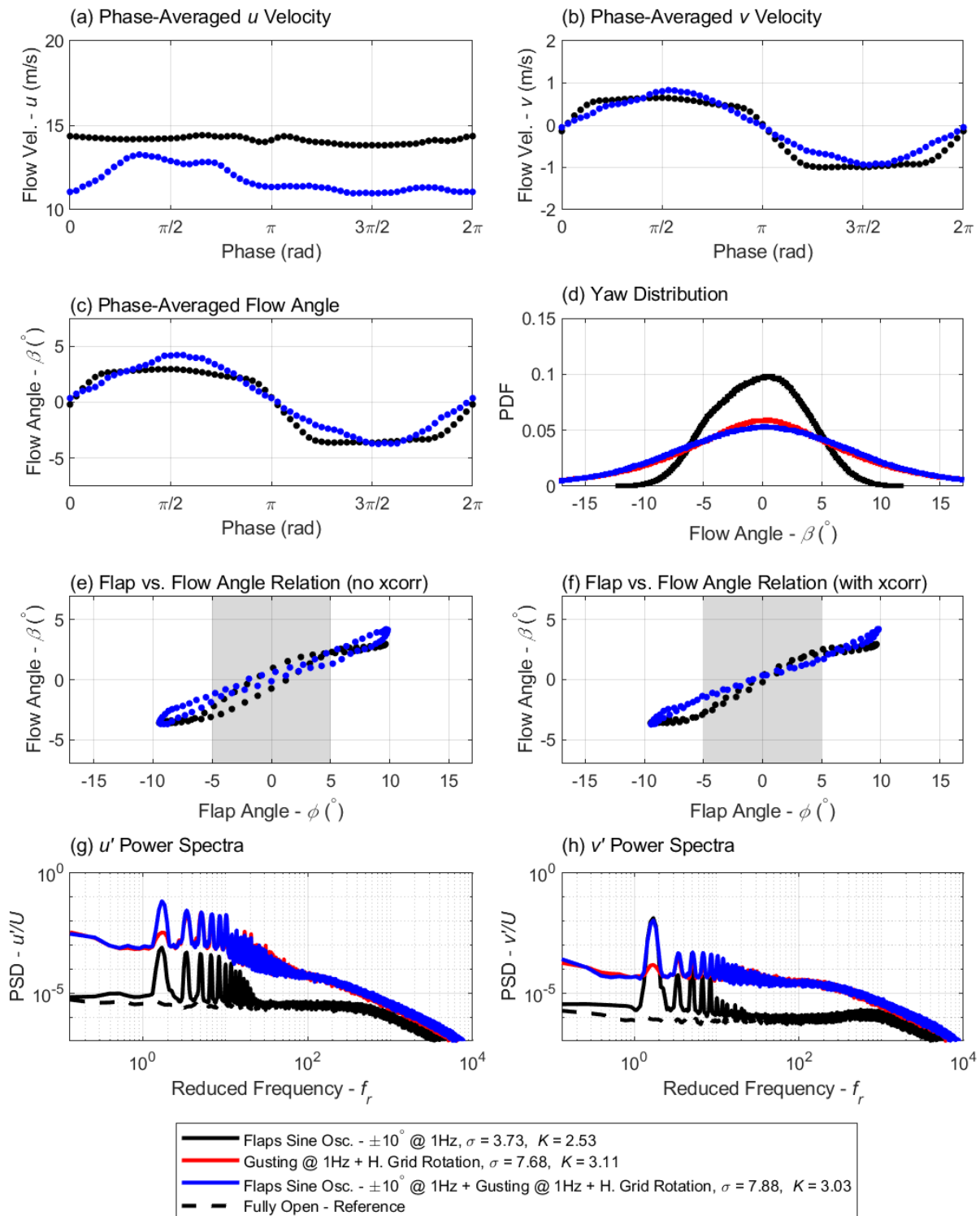


Figure 6.13: Comparison of a combination of yaw, gusting and active grid cases at  $U = 15$  m/s. The subfigures and operating parameters are explained in the text of the corresponding section.

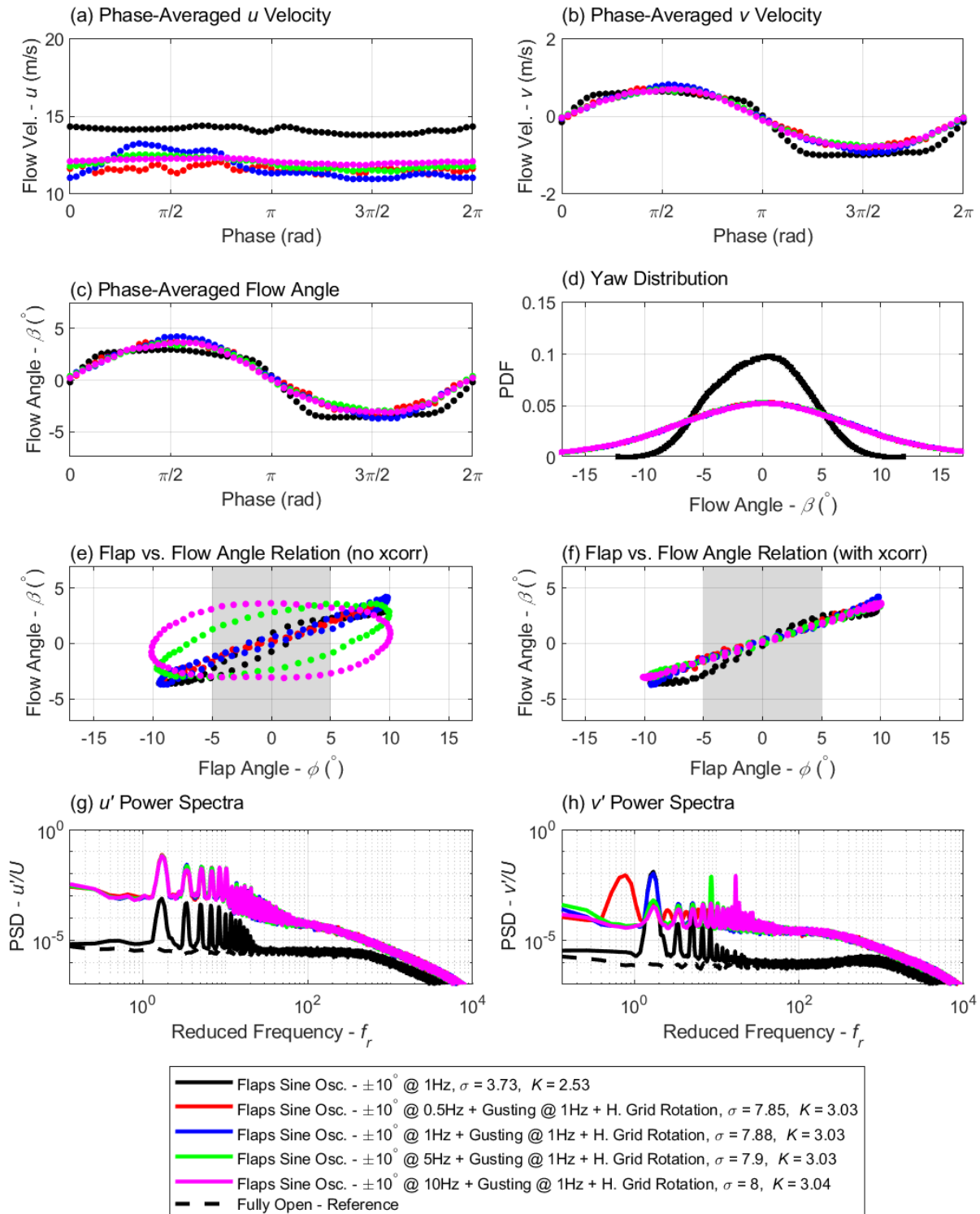


Figure 6.14: Selected flap frequency cases ( $f = 0.5, 1, 5, 10$  Hz) at  $\phi = \pm 10^\circ$  with the gusting and active grid system. Subfigures are explained in the text of the corresponding section.

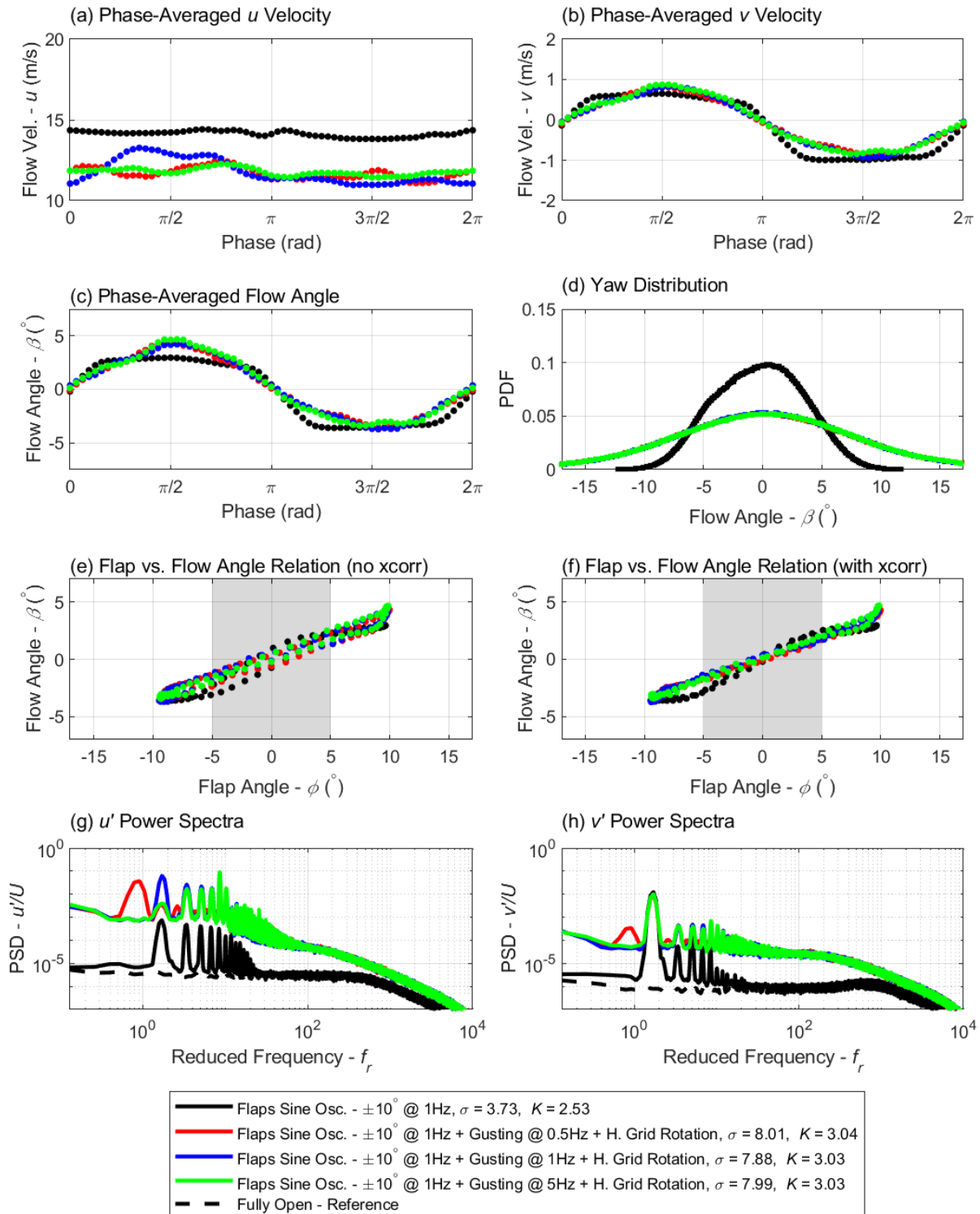


Figure 6.15: Selected gusting frequency cases ( $f = 0.5, 1, 5, 10$  Hz) at  $\phi = \pm 10^\circ$  with the yaw and active grid system. Subfigures are explained in the text of the corresponding section.

### 6.3.7 Frequency Scanning

The following section examines the effect and results of performing frequency scans as shown in Fig. 6.17. The scans dynamically ramp the oscillation frequency of the yaw and gusting system approximately between 0.5 to 12.5 Hz. The flap amplitude and freestream velocity were constant at  $\phi = \pm 10^\circ$  and  $U = 15$  m/s respectively. An example time series of the encoder data is shown in Fig. 6.16. Figure 6.17 subfigures contain the same set of plots and order as Fig. 6.7.

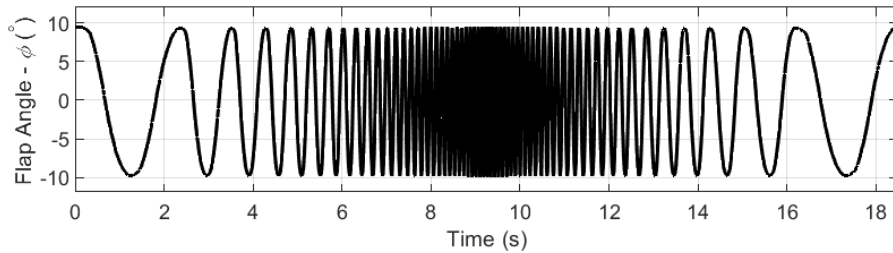


Figure 6.16: Example encoder time series used to show the flap angle as function of time for a frequency scanning test.

In general, the distribution and flap versus flow angle plots do not show any notable observations different to what was already previously discussed in Section 6.3.3. As expected, the effect of dynamic frequency scanning is most notably seen on the power spectrum plots in Fig. 6.17(g) and 6.17(h). The results show that the flow spectra is filled out appropriately depending on the limits of the frequency scan. The plots show that the gusting system generates the most significant fluctuations in the streamwise direction while the yaw system dominates in the spanwise component. However, it is evident that the active grid is still required for medium to high frequencies if the gusting and yaw system are unable to operate at such frequencies. Still, an important observation from the results is the fact that unlike the active grid which fills out the spectra at the expense of creating a wider range of flow yaw, as per Fig. 6.13(d), the frequency scanning can achieve similar spectra while maintaining yaw values between  $\pm 10^\circ$  as observed on the road. Thus, the frequency scanning method can be used as an alternative to the active grid rotation to match on-road flow spectra while maintaining moderate levels of yaw assuming operation frequencies can be achieved.

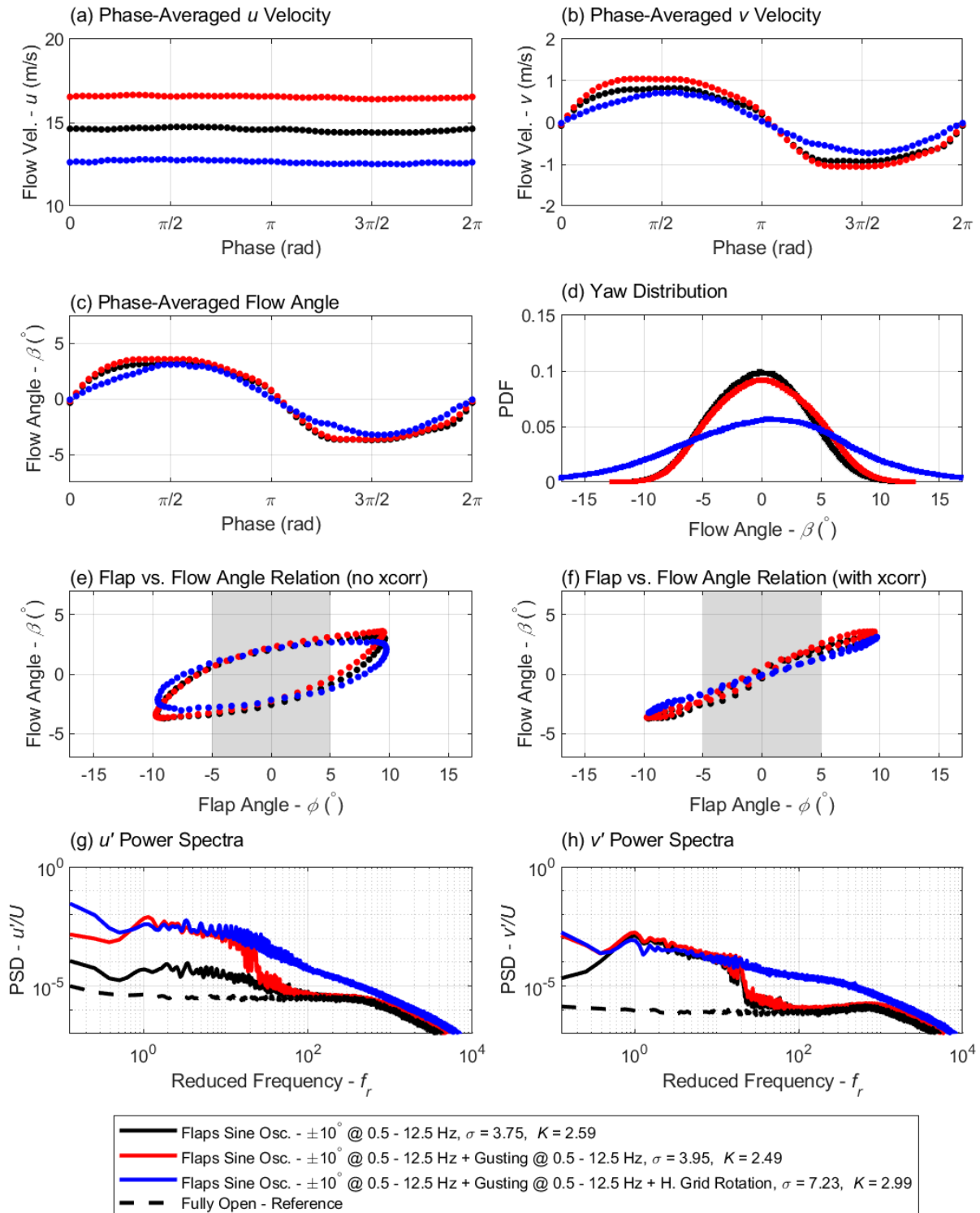


Figure 6.17: Comparison of a combination of yaw, gusting and active grid cases at  $U = 15$  m/s with frequency scanning. The subfigures and operating parameters are explained in the text of the corresponding section.

## 6.4 Summary of Results

The sections above discussed the effects of different operating conditions on measured flow yaw performance and flow spectra. A summary of the observed effects are discussed in the table below.

Table 6.1: Summary of results.

Parameter	Flap versus Flow Angle	Yaw Distribution	PSD
<b>Yaw Osc. Amp.</b>	<ul style="list-style-type: none"> <li>- Linear relation of <math>\beta/\phi = 0.52</math> between <math>\phi = \pm 5^\circ</math>.</li> <li>- Reduced yaw performance (stall) after <math>\phi = \pm 5^\circ</math>.</li> </ul>	<ul style="list-style-type: none"> <li>- Reduces the peak and widens the distribution (increases <math>\sigma</math> and decreases <math>K</math>) with increasing flap amplitude.</li> <li>- Bimodal distribution develops with increasing flap amplitude with peaks at the flow yaw stall angle of approx. <math>\beta = \pm 3^\circ</math>.</li> </ul>	<ul style="list-style-type: none"> <li>- Minor reductions for peak <math>u'</math> PSD magnitude and minor increases of <math>v'</math> PSD magnitude with increasing flap amplitude.</li> </ul>
<b>Yaw Osc. Freq.</b>	<ul style="list-style-type: none"> <li>- Increased hysteresis with increasing flap frequency.</li> <li>- Slight increases in the max mean yaw angle with increasing flap frequency.</li> <li>- Maintains <math>\beta/\phi = 0.52</math> linear flap versus flow angle relation pre-stall and a stall angle of <math>\phi = \pm 5^\circ</math>.</li> </ul>	<ul style="list-style-type: none"> <li>- Minor peak reductions with increasing flap frequency.</li> <li>- Increasing flap frequency slightly increases <math>\sigma</math> and slightly decreases <math>K</math>.</li> </ul>	<ul style="list-style-type: none"> <li>- Creates minor <math>u'</math> PSD peaks at the corresponding flap frequency and it's integer harmonics.</li> <li>- Creates major <math>v'</math> PSD peaks at the corresponding flap frequency and it's integer harmonics (strong odd peaks).</li> </ul>

Table 6.1 continued from previous page

<p><b>Freestream Vel.</b></p>	<ul style="list-style-type: none"> <li>- Minor increases to the peak mean yaw angle with increasing velocity.</li> <li>- Maintains <math>\beta/\phi = 0.52</math> linear flap versus flow angle relation pre-stall and a stall angle of <math>\phi = \pm 5^\circ</math>.</li> <li>- The severity of the yaw performance reduction after stall is reduced with increasing velocity.</li> </ul>	<ul style="list-style-type: none"> <li>- Reduces the peak and shifts towards a bimodal distribution with increasing velocity.</li> <li>- Increasing velocity increases <math>\sigma</math> and decreases <math>K</math>.</li> </ul>	<ul style="list-style-type: none"> <li>- No significant effect.</li> <li>- PSD reduced frequency is observed due to being normalized by velocity.</li> </ul>
<p><b>Triangle Osc.</b></p>	<ul style="list-style-type: none"> <li>- Slowest response time out of all shapes tested.</li> <li>- Phase-averaging bins are evenly distributed.</li> <li>- Phase-averaged response is closer to a sinusoidal shape.</li> <li>- Maintains <math>\beta/\phi = 0.52</math> linear flap versus flow angle relation pre-stall and a stall angle of <math>\phi = \pm 5^\circ</math>.</li> </ul>	<ul style="list-style-type: none"> <li>- Increases the distribution peak.</li> <li>- Reduces <math>\sigma</math> and increases <math>K</math>.</li> </ul>	<ul style="list-style-type: none"> <li>- Generates strong <math>v'</math> PSD peaks at the operating freq. and its integer harmonics.</li> </ul>

Table 6.1 continued from previous page

<p><b>Square Osc.</b></p>	<ul style="list-style-type: none"> <li>- Fastest response time out of all shapes tested.</li> <li>- Phase-averaging bins are concentrated at the peak yaw angles.</li> <li>- Phase-averaged response is square and has a large proportion of stalled flow.</li> <li>- Maintains <math>\beta/\phi = 0.52</math> linear flap versus flow angle relation pre-stall and a stall angle of <math>\phi = \pm 5^\circ</math>.</li> </ul>	<ul style="list-style-type: none"> <li>- Decreases the distribution peak.</li> <li>- Increases <math>\sigma</math> and increases <math>K</math>.</li> </ul>	<ul style="list-style-type: none"> <li>- Generates strong <math>v'</math> PSD peaks at the operating freq. and its odd harmonics.</li> </ul>
<p><b>Gusting Subsystem</b></p>	<ul style="list-style-type: none"> <li>- No significant effect.</li> </ul>	<ul style="list-style-type: none"> <li>- No significant effect.</li> </ul>	<ul style="list-style-type: none"> <li>- Generates strong <math>u'</math> PSD peaks at the gusting operating freq. and its integer harmonics.</li> </ul>
<p><b>Active Grid Subsystem</b></p>	<ul style="list-style-type: none"> <li>- Significantly reduces the linear pre-stall region slope to <math>\beta/\phi = 0.36</math>.</li> <li>- Removes the previously observable stall angle at <math>\phi = \pm 5^\circ</math>.</li> </ul>	<ul style="list-style-type: none"> <li>- Significantly reduces the peak and widens the base of the distribution (significantly increases <math>\sigma</math>).</li> <li>- Generates normal distributions with kurtosis values of approx. 3.</li> </ul>	<ul style="list-style-type: none"> <li>- Increases <math>u'</math> and <math>v'</math> PSD magnitudes across medium to high frequencies.</li> </ul>
<p><b>Freq. Scanning</b></p>	<ul style="list-style-type: none"> <li>- No significant effect.</li> </ul>	<ul style="list-style-type: none"> <li>- No significant effect.</li> </ul>	<ul style="list-style-type: none"> <li>- Increases <math>u'</math> and <math>v'</math> PSD magnitudes across the flap operating frequency range.</li> </ul>

## 6.5 Comparison to On-Road Measurements

The primary objective for this thesis was to research and develop a novel TGS that can replicate a wide range of on-road flow conditions. As discussed in Section 2.1, on-road flow can be characterized by the measured yaw and power spectra. As such, comparisons between several TGS test cases and collected on-road data from literature are presented in this section. Comparisons for the flow yaw distributions in different traffic conditions and trailing distances are given in Fig. 6.18 and 6.19 respectively. Finally, a comparison of the power spectra for different TGS systems and collected on-road data is given in Fig. 6.20 and 6.21.

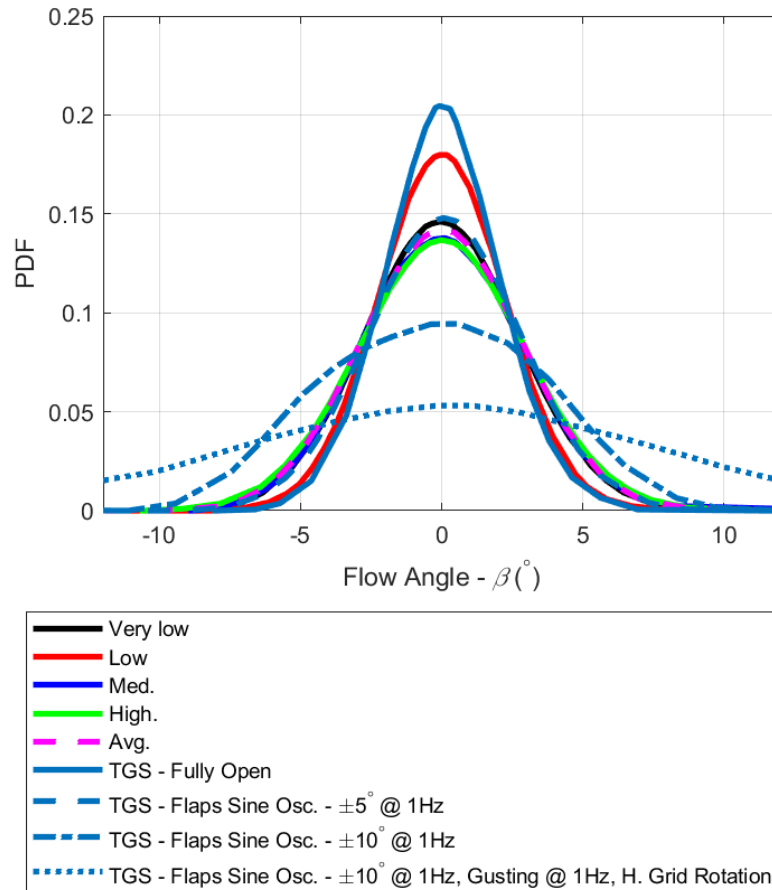


Figure 6.18: Comparison of on-road yaw distributions at different traffic conditions from Jessing et al. [5] and four selected TGS test cases.

The TGS has been shown to be able to replicate on-road flow yaw distributions at a variety of different traffic conditions that were previously reported by Jessing et al. [5]. For example, the average yaw distribution for different traffic densities measured Jessing et al. can be directly achieved by a sinusoidal flap oscillation of  $\pm 5^\circ$  at 1 Hz as shown in Fig. 6.18 [5]. Meanwhile, Fig. 6.19 shows four TGS test cases that completely replicate the yaw distribution across all trailing distances considered. The yaw system by itself has shown that it is capable of replicating distributions for trailing distances from and infinite distance to approximately 25 m as evident by the fully open to the  $\phi = \pm 10^\circ$  at 1 Hz sinusoidal oscillation cases. Based on the collected results, the yaw system may be able to replicate the 20 m case by either increasing the flap amplitude, increasing flap frequency or oscillating the flap in a square wave. However, the active grid is required to replicate distributions taken at a trailing distance closer than 20 m. Therefore, the comparisons show that TGS capable of directly replicating a variety of measured on-road flow distributions.

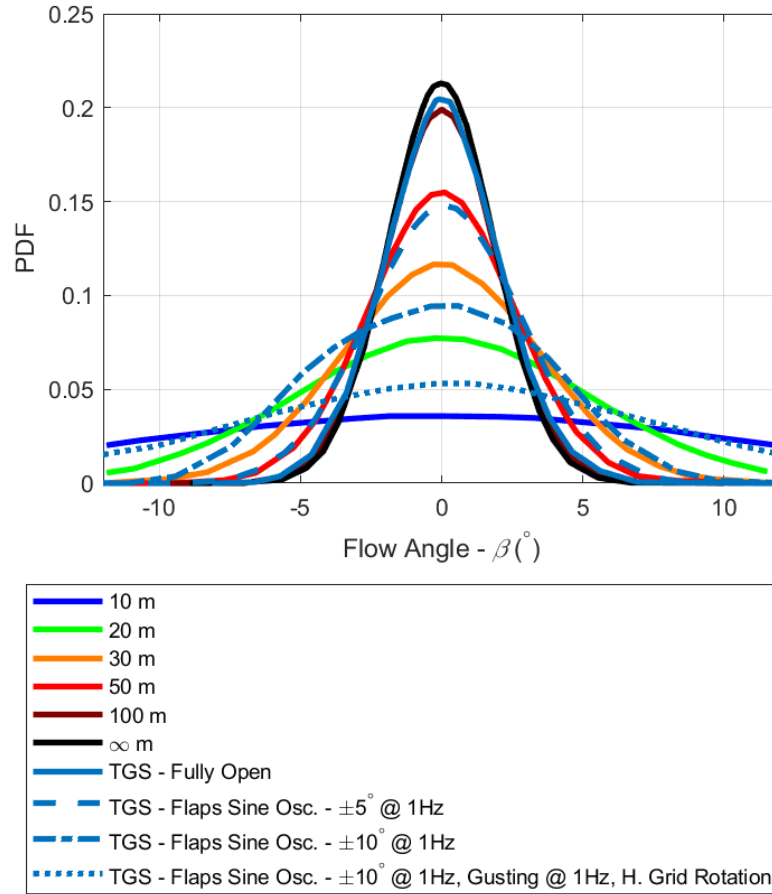


Figure 6.19: Comparison of on-road yaw distributions at different trailing distances from a leading box truck from Jessing et al. [5] and four selected TGS test cases.

Fig. 6.20 and 6.21 show the measured power spectra compared to different systems and on-road data found in literature. The reduced frequency, as defined in Section 2.1 with  $f_r = 2\pi f_s L_r / U_r$ , utilizes both a reference length scale ( $L_r$ ) and velocity scale ( $U_r$ ). On-road measurements use values of  $L_r = 4$  m and  $U_r = 27.8$  m/s. Meanwhile, TGS data use values of  $L_r = 4$  m and  $U_r = 15$  m/s. In general, the TGS is shown to have sufficient performance in replicating the streamwise power spectra but lacks in the spanwise direction.

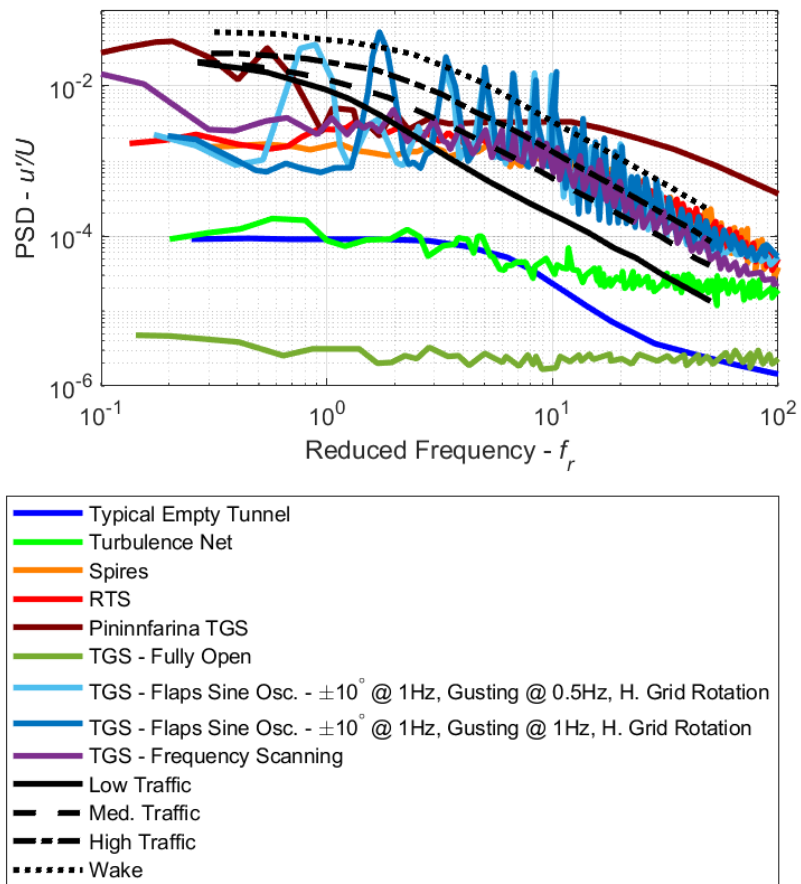


Figure 6.20: Comparison of the streamwise power spectra of different systems and on-road traffic from McAuliffe et al. [8] and select TGS test cases.

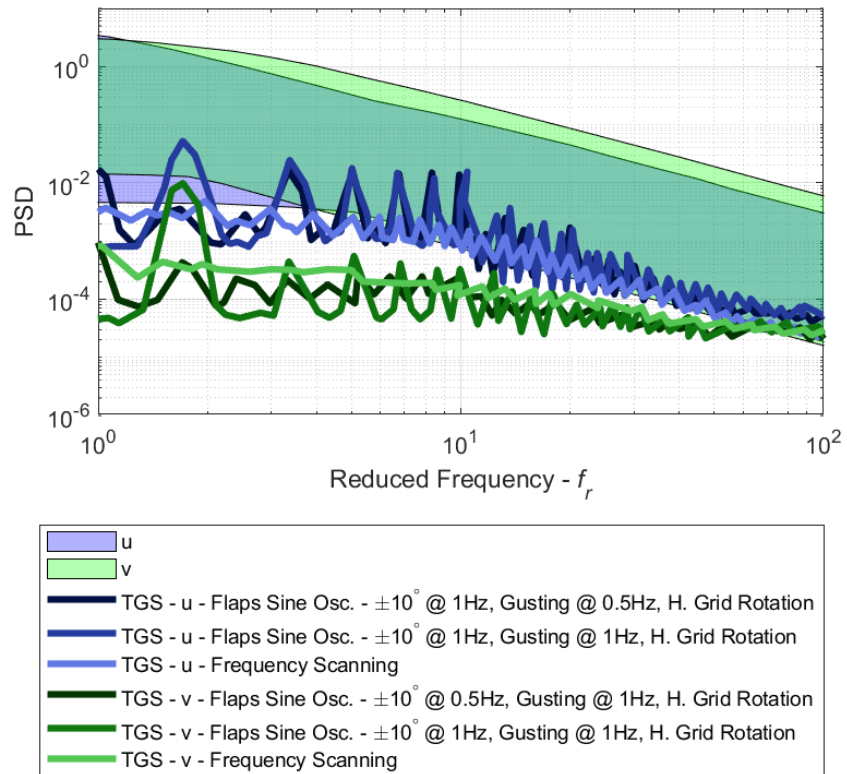


Figure 6.21: Comparison of the TGS and the envelope of on-road flow power spectra at different terrain types from Wordley et al. [4].

## 7 Conclusions and Recommendations

### 7.1 Conclusions

The motivation for this research is to better simulate on-road wind conditions in automotive wind tunnels. In this thesis, the research, development and characterization of a novel TGS design was presented. Contributions to the design and assembly of the mechanical and electrical systems of the novel TGS were also made. The TGS was comprised of three main subsystems, including the unsteady yaw, gusting and active grid system, to replicate on-road flow conditions that were determined from literature. This research focused on the unsteady yaw generation subsystem aspect of the TGS design. Several operation parameters of the yaw system, such as oscillation frequency and amplitude, as examples, were varied. Additionally, select test cases with the gusting and active grid system were considered.

Measurements of the flow were performed using two-component hotwire anemometry. The flow measurements were constrained to a location at  $X = 250$  mm from the TGS, which represents the approximate location where a vehicle would be situated in the 3/4 open jet test section of the model automotive wind tunnel. For the flow measurements, a reference signal of the instantaneous flap angle was sampled in parallel so that phase-averaged results of the yaw oscillating flow could be obtained. A set of six spatially averaged points were determined to be suitable to represent the flow behavior determined from a set of low and high-resolution scans of the flow field.

The as designed TGS yaw subsystem with the other subsystems in place demonstrated a range of mean flow angles of approximately  $\beta = \pm 4.5^\circ$  for flap angles of  $\phi = \pm 15^\circ$ . Additionally, the flap versus flow angle response was shown to be linear with a slope of  $\beta/\phi = 0.52$  between  $\phi = \pm 5^\circ$ . Reduced flow turning

performance, or possibly stall, was observed after  $\phi = \pm 5^\circ$ . The mean response of the yaw subsystem was affected by the addition of the active grid subsystem, reducing the flap versus flow angle relation linear slope to  $\beta/\phi = 0.35$ . However, the current active yaw system was able to meet performance targets related to replication of on-road measurements. The yaw system was able to produce yaw distributions with PDF peaks ranging from 0.08 to 0.21 and peak flow yaw angles between  $\beta = \pm 12^\circ$ . The sinusoidal flap oscillations, used for majority of the tests, have been shown to have standard deviations ranging from  $\sigma = 2.7 - 4^\circ$  and were generally tail heavy with kurtosis values ranging from  $K = 2.37 - 3$ , where the latter value is representative of a normal distribution. However, it was shown from limited testing that triangle flap oscillations may better replicate normal yaw distributions over broader operational ranges. The addition of the active grid system has been shown to generate normally distributed flow yaw with decreased PDF peaks from 0.03 - 0.05 while generating a significantly larger range of flow yaw angles between  $\beta = \pm 25^\circ$  and standard deviations up to  $\sigma = 8$ . The main parameters shown to affect the yaw distribution are the flap amplitude, freestream velocity, oscillation shape and the active grid. In general, it has been shown that different combinations of these parameters can be used to tune the shape of the generated yaw distributions allowing the system to directly replicate on-road yaw in different environmental conditions.

Power spectral density analysis has shown that the TGS has limited performance when replicating on-road flow spectra. The yaw system was shown to be able to create peaks at targeted frequencies for the spanwise power spectra but often lack the required magnitude. Meanwhile, the gusting system has been shown to generate peaks at targeted frequencies while containing sufficient peak magnitude. Finally, the active grid has been shown to generate broadband energy from medium to high frequencies.

## 7.2 Recommendations

Although this thesis outlined novel methods of designing, controlling and evaluating a modern TGS system capable of replicating a wide range of flow conditions, several improvements can still be made. These improvements range from TGS configuration changes to different measurement methods or tools. The following section will discuss recommendations that can be used to contribute to future works.

The active yaw system of the novel TGS was shown to replicate a wide range of on-road flow conditions in the model scale wind tunnel. The flow was measured using time resolved hot-wire anemometry, which is a point-based measurement technique. The next progression in quantification of the flow field would be to spatially resolve the streamwise and spanwise flow variations around the intended location of a vehicle. Measurement techniques such as Particle Imaging Velocimetry would be well suited for this purpose. Furthermore, another potential analysis to be conducted is the TGS's ability to be scaled up for full scale applications. This can be done by running operation parameters to match appropriate non-dimensional scaling factors, such as reduced frequency.

The results obtained in this thesis are for the active yaw subsystem in parallel with the other components of the TGS, including the active grid and gust generation subsystems. It was shown that the grid subsystem modified the active yaw system performance from predicted values. Therefore, future design of an active yaw system should include consideration of effects of embedded turbulence generation subsystems. Furthermore, an important question concerning the application of a TGS in a wind tunnel is the mean and unsteady pressure losses induced in the closed loop circuit, which effect the fan. Future work should consider determination of relationships between the effected flow parameters, such as the maximum yaw and oscillation frequency, on losses induced by the TGS.

## Bibliography

- [1] G. Cacho, J. Marques, and R. Hanson, “Turbulence generation system recommendations.” Private Communication, 10 2020.
- [2] B. Duncan, L. D’Alessio, J. Gargoloff, and A. Alajbegovic, “Vehicle aerodynamics impact of on-road turbulence,” Proceedings of the Institution of Mechanical Engineers, Part D: Journal of Automobile Engineering, vol. 231, no. 9, pp. 1148–1159, 2017.
- [3] A. Brown, “This incredible process is how automakers make extremely fuel efficient cars.” <https://www.businessinsider.com/how-automakers-test-a-cars-aerodynamics-2016-4>, 2016. Accessed: 2022-09-15.
- [4] S. Wordley and J. Saunders, “On-road turbulence: Part 2,” SAE Int. J. Passeng. Cars – Mech. Syst., vol. 2, pp. 111–137, 04 2009.
- [5] C. Jessing, H. Wilhelmi, F. Wittmeier, A. Wagner, J. Wiedemann, and A. Dillmann, “Investigation of transient aerodynamic effects on public roads in comparison to individual driving situations on a test site,” tech. rep., SAE Technical Paper, 2020.
- [6] D. Stoll and J. Wiedemann, “Active crosswind generation and its effect on the unsteady aerodynamic vehicle properties determined in an open jet wind tunnel,” SAE Int. J. Passeng. Cars - Mech. Syst., vol. 11, pp. 429–446, 04 2018.
- [7] B. R. McAuliffe, L. Belluz, and M. Belzile, “Measurement of the on-road turbulence environment experienced by heavy duty vehicles,” SAE Int. J. Commer. Veh., vol. 7, pp. 685–702, 09 2014.

- [8] B. R. McAuliffe and A. D’Auteuil, “A system for simulating road-representative atmospheric turbulence for ground vehicles in a large wind tunnel,” SAE International Journal of Passenger Cars-Mechanical Systems, vol. 9, no. 2016-01-1624, pp. 817–830, 2016.
- [9] A. Cogotti, “Generation of a controlled level of turbulence in the pininfarina wind tunnel for the measurement of unsteady aerodynamics and aeroacoustics,” in SAE Technical Paper, SAE International, 03 2003.
- [10] S. Terakado, T. Makihara, T. Sugiyama, K. Maeda, K. Tadakuma, K. Tsuboi, M. Iyota, K. Kosaka, and S. Sugiyama, “Experimental investigation of aeroacoustic cabin noise in unsteady flow by means of a new turbulence generating device,” SAE International Journal of Passenger Cars-Mechanical Systems, vol. 10, no. 2017-01-1545, pp. 309–317, 2017.
- [11] H. Wilhelmi, C. Jessing, J. Bell, D. Heine, A. Wagner, J. Wiedemann, and C. Wagner, “Simulation of transient on-road conditions in a closed test section wind tunnel using a wing system with active flaps,” in SAE Technical Paper, SAE International, 04 2020.
- [12] J. McKillen, “Turbulence generation system.” Patent, 10 2020.
- [13] N. Lindener, H. Miehl, A. Cogotti, F. Cogotti, and M. Maffei, “Aeroacoustic measurements in turbulent flow on the road and in the wind tunnel,” SAE Transactions, pp. 1481–1500, 2007.
- [14] A. D’Hooge, R. Palin, L. Rebbeck, J. Gargoloff, and B. Duncan, “Alternative simulation methods for assessing aerodynamic drag in realistic crosswind,” SAE International Journal of Passenger Cars-Mechanical Systems, vol. 7, no. 2014-01-0599, pp. 617–625, 2014.
- [15] A. P. Gaylard, N. Oettle, J. Gargoloff, and B. Duncan, “Evaluation of non-uniform upstream flow effects on vehicle aerodynamics,” SAE Int. J. Passeng. Cars - Mech. Syst., vol. 7, pp. 692–702, 04 2014.
- [16] G. Carlino and A. Cogotti, “Simulation of transient phenomena with the turbulence generation system in the pininfarina wind tunnel,” in SAE Technical Paper, SAE International, 04 2006.

- [17] S. Watkins, J. Saunders, and P. Hoffmann, “Turbulence experienced by moving vehicles. part i. introduction and turbulence intensity,” Journal of Wind Engineering and Industrial Aerodynamics, vol. 57, no. 1, pp. 1–17, 1995.
- [18] S. J. Miller, M. Gordon, R. M. Staebler, and P. A. Taylor, “A study of the spatial variation of vehicle-induced turbulence on highways using measurements from a mobile platform,” Boundary-Layer Meteorology, vol. 171, pp. 1–29, 2019.
- [19] J. W. Saunders and R. B. Mansour, “On-road and wind tunnel turbulence and its measurement using a four-hole dynamic probe ahead of several cars,” in SAE Technical Paper, SAE International, 03 2000.
- [20] D. Sims-Williams, “Cross winds and transients: reality, simulation and effects.,” SAE International journal of passenger cars. Mechanical systems., vol. 4, no. 1, pp. 172–183, 2011.
- [21] D. Spence, “Growth of the turbulent wake close behind an aerofoil at incidence,” 1953.
- [22] R. Raj and B. Lakshminarayana, “Characteristics of the wake behind a cascade of airfoils,” Journal of Fluid Mechanics, vol. 61, no. 4, pp. 707–730, 1973.
- [23] RDDM, “Module 04 – axial flow compressors.” [https://moodle.polymt1.ca/file.php/1047/HDVo/Module\\_04\\_-\\_Axial\\_Flow\\_Comp.pdf](https://moodle.polymt1.ca/file.php/1047/HDVo/Module_04_-_Axial_Flow_Comp.pdf), 1 2011. Accessed: 2022-12-11.
- [24] MIT, “16.50 lecture 25: Velocity triangles; compressor performance maps.” [https://ocw.mit.edu/courses/16-50-introduction-to-propulsion-systems-spring-2012/6242f54646f5274f1b7d809400e6fe00\\_MIT16\\_50S12\\_1ec25.pdf](https://ocw.mit.edu/courses/16-50-introduction-to-propulsion-systems-spring-2012/6242f54646f5274f1b7d809400e6fe00_MIT16_50S12_1ec25.pdf), 3 2012. Accessed: 2022-12-11.
- [25] P. Bearman, “Corrections for the effect of ambient temperature drift on hot-wire measurements in incompressible flow disa info,” Bull, vol. 11, 1971.
- [26] J. Taylor, An Introduction to Error Analysis: The Study of Uncertainties in Physical Measurements, Second Edition. University Science Books Mill Valley, 1997.

## A Assessment of Effects on Turning Vane Performance

Additional analysis was conducted to determine the possible causes of airfoil stall after flap angles of  $\phi = \pm 5^\circ$ . Two main hypotheses relating to the reduced yaw performance are discussed in this section. First, tests were conducted with the active grid to verify the negative effect of the active grid on yaw performance. Secondly, a discussion on airfoil geometry is presented.

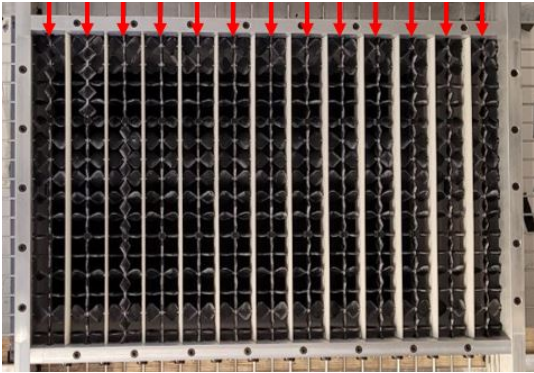


Figure A.1: Red arrows show the location of the fixed vertical active grid shaft elements.



Figure A.2: Close up of the TGS in the fully open position. The fixed vertical active grid elements are shown to be in parallel to the airfoils. These elements remained fixed during the original tests.

Tests were conducted to determine the effect of the vertical active grid shafts. Previously, the vertical active grid shafts were fixed parallel to the fixed airfoil bodies during the original test program as shown in Fig. A.1 and A.2. It was hypothesized that these flow elements reduce the yaw performance of the cascade because they work against the angled flaps since they remain straight throughout the test. Additional motors that directly control the vertical shaft elements were installed onto the TGS to verify this hypothesis; the vertical flow elements were programmed to follow the yaw system flap oscillation and was compared to the previously fixed configuration. The baseline yaw oscillation case was compared against a case with the

vertical grid tracking. All cases were tested at a freestream velocity of 15 m/s. The results of these tests can be seen in Fig. A.3(a) and A.3(b).

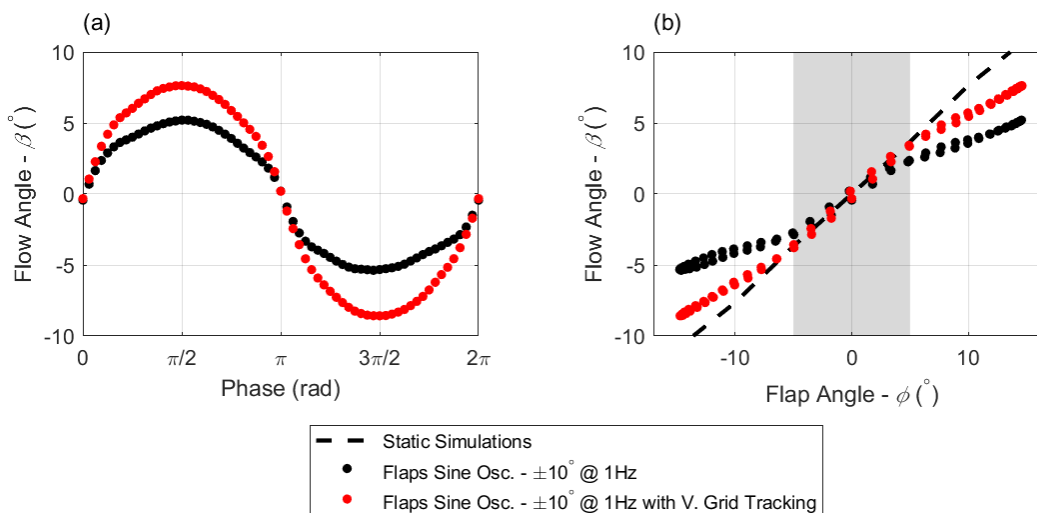


Figure A.3: Phase-averaged plots for the vertical grid tracking test compared against the original testing configuration. Comparison with the simulated results are also shown.

The plots above show that the vertical grid elements have a significant improvement on the yaw performance when configured to track the flap motion. First, the maximum achievable yaw angle increases to approximately  $\beta = \pm 8^\circ$  from the original  $\beta = \pm 5.2^\circ$  at a flap angle of  $\phi = \pm 15^\circ$ . Furthermore, the slope within the stall region increased to  $\beta/\phi = 0.70$  compared to the original  $\beta/\phi = 0.52$ . Although the flap stall angle of  $\phi = \pm 5^\circ$  appears to still be present, the flap versus flow results of the vertical grid tracking appears to be more linear. All of these observations show that the addition of the vertical grid tracking increases the yaw system performance and brings it closer to the simulated results ( $\beta/\phi = 0.74$ ) as shown in Fig. A.3(b). Therefore, the results of this analysis shows that the vertical grid tracking should be used in future tests to maximize the performance of the yaw system.



Figure A.4: Top view of the airfoil assembly with the gap (approx. 0.5 mm) circled in red.

Another potential factor affecting the yaw performance is the gap between the airfoil and flap as shown in Fig. A.4. It was hypothesized that air would flow from the pressure side to the suction side through this gap which would trip the flow and increase flow separation. In order to test this, the flap was held at static angles from  $\beta = \pm 0 - 15^\circ$  with tufts taped on the airfoil to visualize the flow over the flap as shown in Fig. A.4. Tape was added to completely cover the gap across each airfoil. Comparisons with and without the tape for each flap angle is shown visually in Fig. A.5 and A.6 respectively and through collected hotwire data in Fig. A.7. All angles were tested at a freestream velocity of 15 m/s.

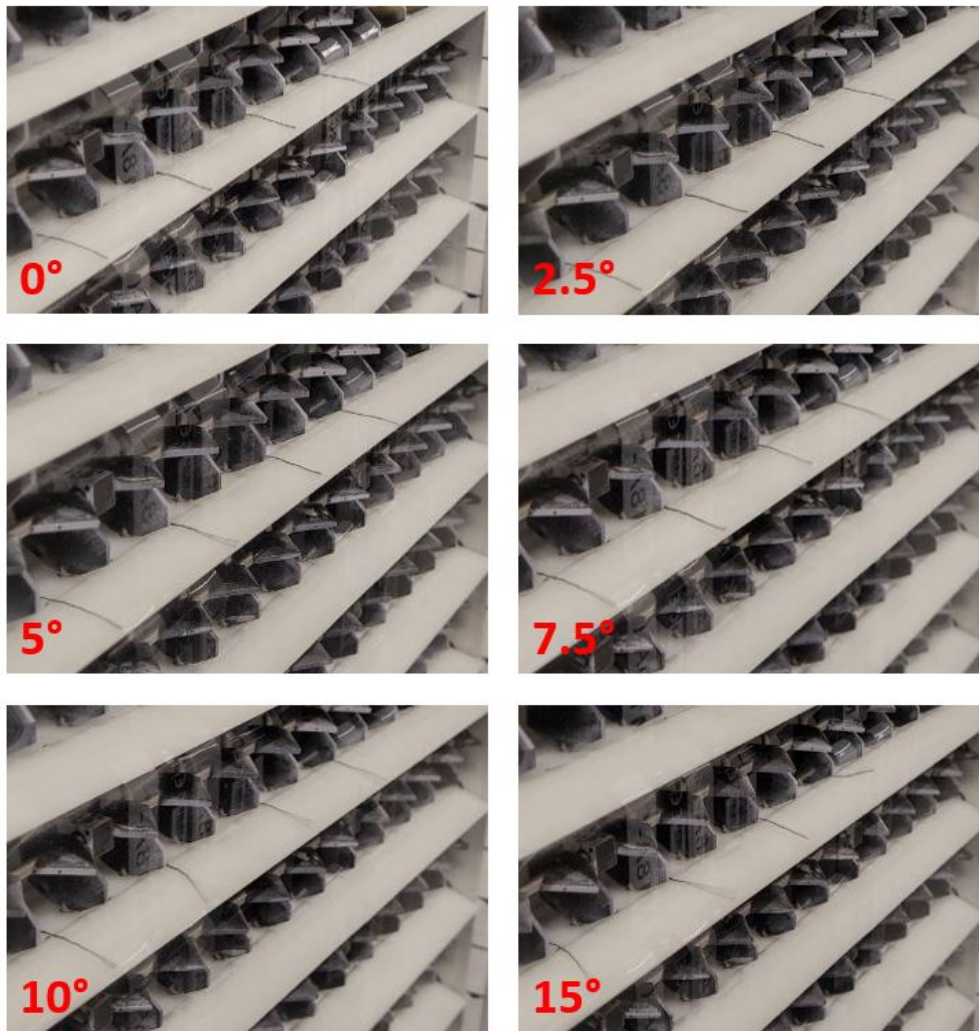


Figure A.5: Images of tufts at different flap angles without tape across the airfoil gaps.

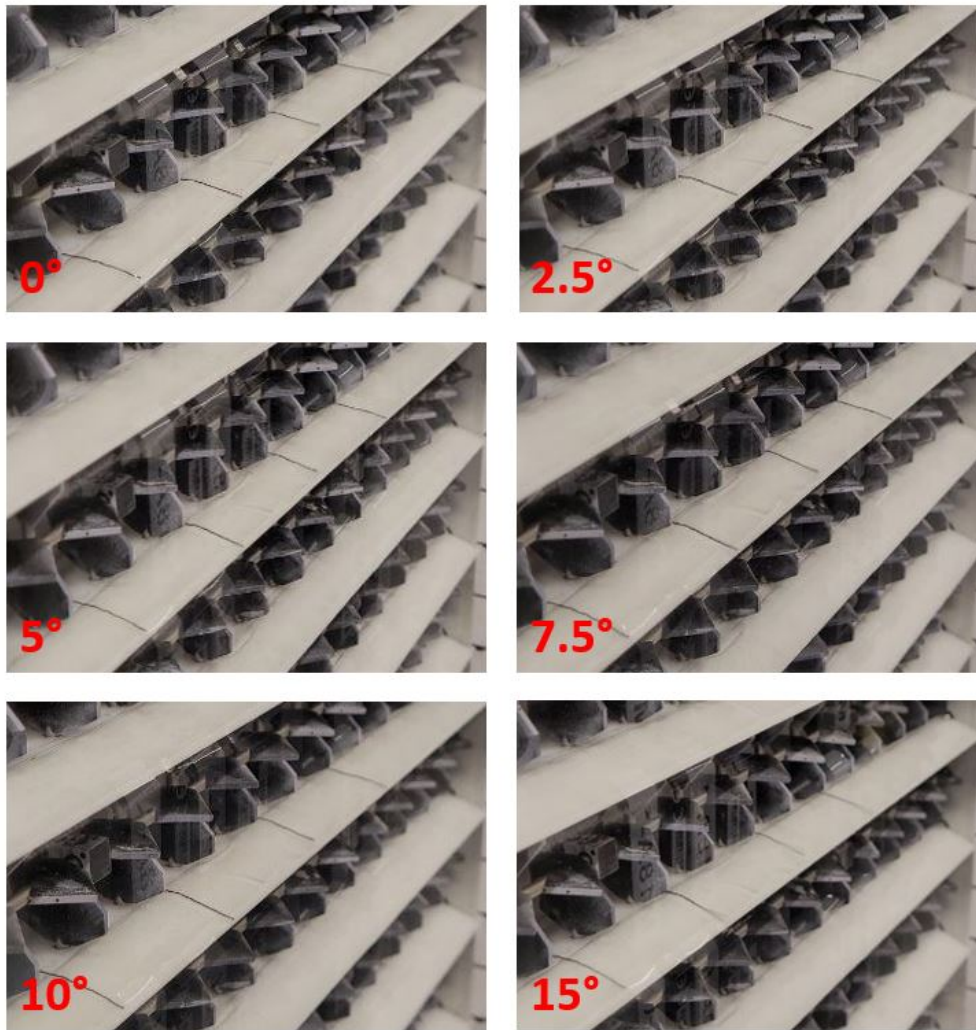


Figure A.6: Images of tufts at different flap angles with tape across the airfoil gaps.

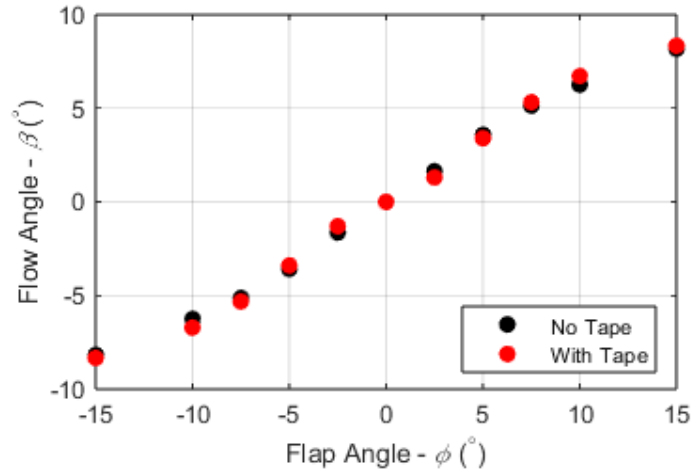


Figure A.7: Flap versus flow angle plot of flaps held at static flap angles with and without tape over the gaps.

Visually, the tape has been observed to reduce the flow separation over the flap at higher angles. Figure A.5 and A.6 show flow reversal is present at higher flap angles greater than  $\phi = 7.5^\circ$  for the case without the tape. On the other hand, this observation of flow separation does not appear to be as significant for the cases with the taped gaps. Thus, visual observations indicate that the tape does indeed reduce the flow separation which should increase yaw performance. However, the collected hotwire data, as shown Fig. A.7, shows that there is little difference between the two cases considered. Therefore, it is unclear whether or not adding tape across the gaps has an effect on the yaw performance.

## B Select Mechanical Diagrams

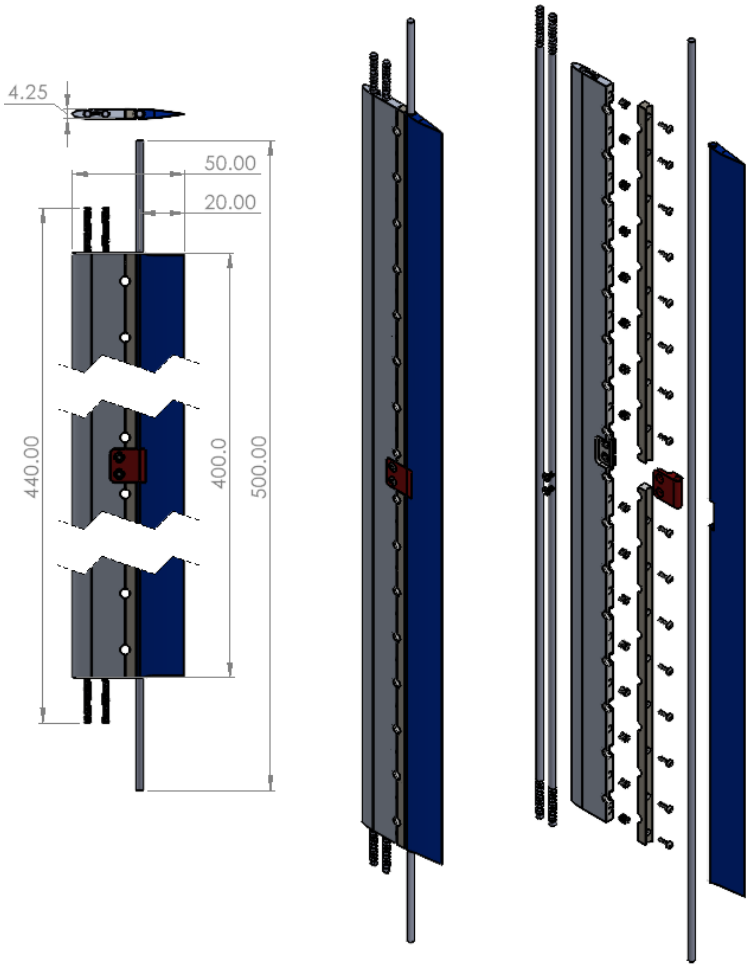


Figure B.1: Mechanical assembly of a single airfoil with important dimensions only. The diagram includes the flap (blue), fixed airfoil body (gray), flap shaft support (red), backplate (brown), 2 airfoil body support/installation threaded rods, 1 flap shaft, and fasteners (threaded inserts and screws).

## C Select Electrical Diagrams

Select electrical diagrams have been provided in this section for reference. The diagrams include connections used for a single motor, power supply daisy chains and the power/COM line assignments for the TGS.

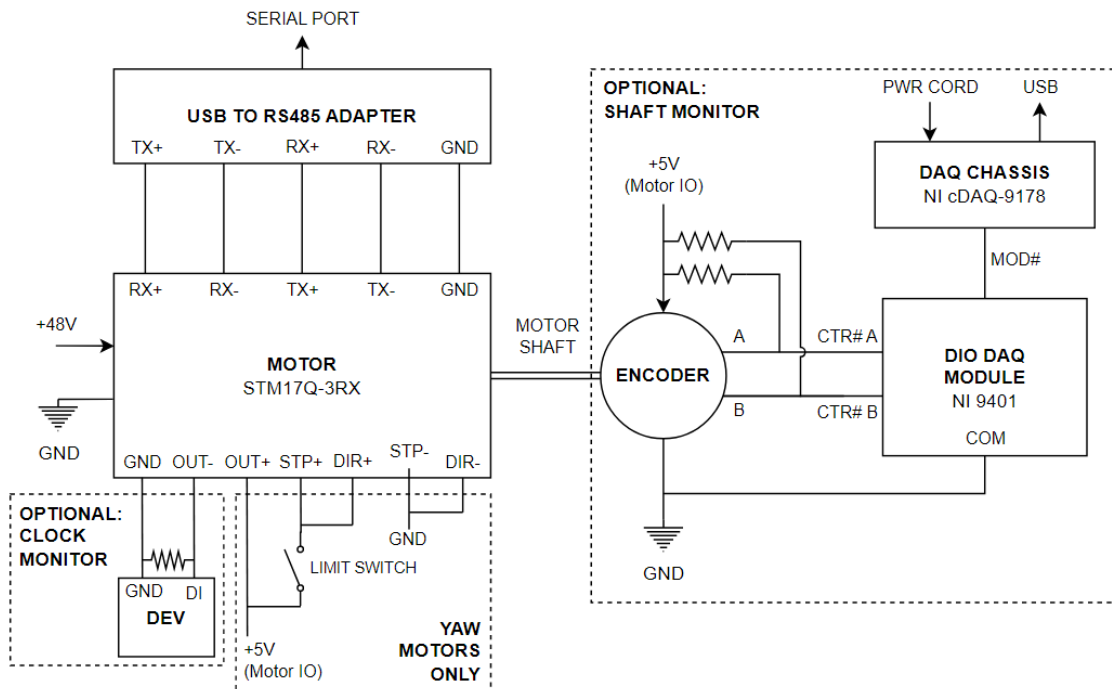


Figure C.1: General electrical diagrams for a single motor with optional connections.

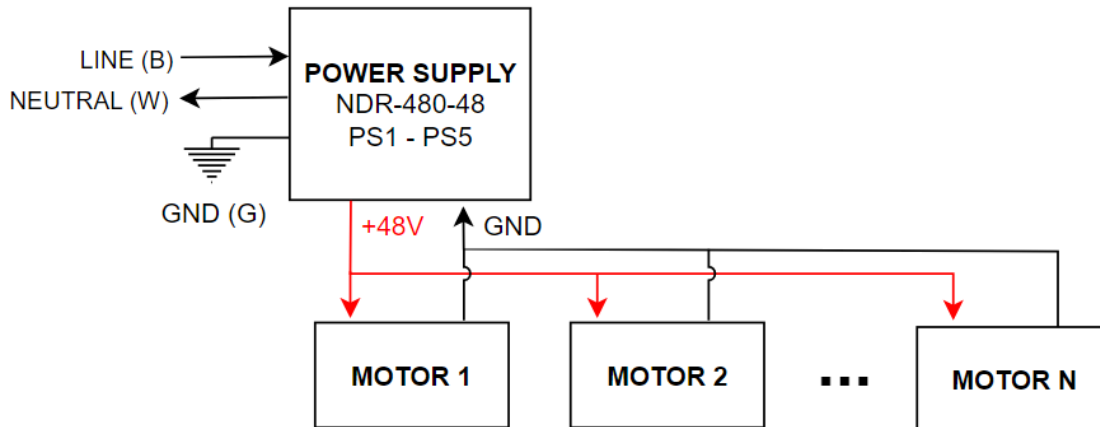
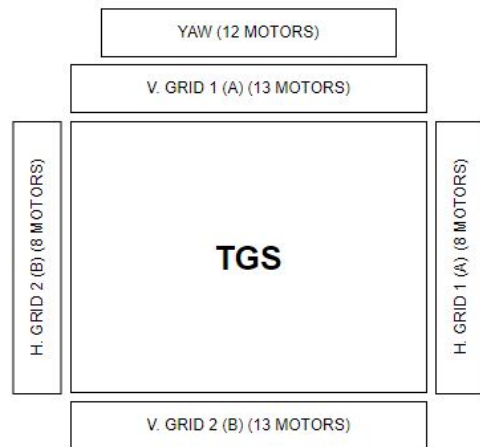


Figure C.2: Power supply daisy chain diagram.



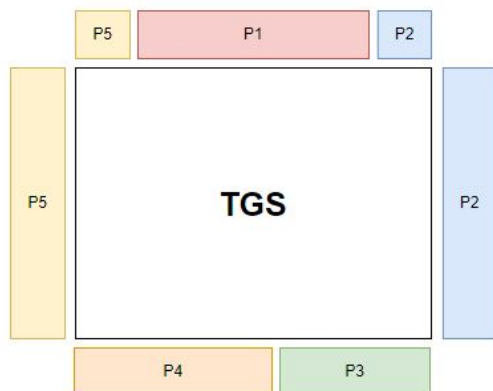
**COM ASSIGNMENTS**

**2 COM PORTS (MAX 32 MOTORS/COM)**

**COM A:** H. GRID 1 + V. GRID 1 = 21 MOTORS

**COM B:** H. GRID 2 + V. GRID 2 = 21 MOTORS

**[NOTE]** The YAW motors will use COM A



**PWR ASSIGNMENTS**

**5 PWR DAISY CHAINS (MAX 10 MOTORS/CHAIN)**

**P1:** V. GRID 1 (9) = 9 MOTORS

**P2:** H. GRID 1 (8) + V. GRID 1 (2) = 10 MOTORS

**P3:** V. GRID 2 (6) = 6 MOTORS

**P4:** V. GRID 2 (7) = 7 MOTORS

**P5:** H. GRID 2 (8) + V. GRID 1 (2) = 10 MOTORS

**[NOTE]** The YAW motors will use the same PWR harness P1, P2 & P5

Figure C.3: Motor power supply and COM line assignments divided by groups.

## D Select Codes

As discussed previously in this thesis, a pre-loading method was applied to the motors to get around several issues concerning the feasibility of individually controlling over 50 motors with time-based commands using a single control system. Figure D.1 and D.2 shows the working principle of the motor control system. The timing diagram, as shown in Fig. D.1, was used to obtain the angular velocity and acceleration equations presented in Section 3.6.2. These equations were derived using the ratio of time a certain action is performed in a single move or half a cycle; for example, the fraction of time stopped,  $R_s$ , can be calculated with  $R_s = t_s/(1/2T)$ . Afterwards, these ratios can be used with equations for total shaft displacement and angular velocity to obtain the aforementioned equations. Therefore, these equations make it possible to calculate the exact angular velocity and acceleration to perform any of the motion cases described in this thesis.

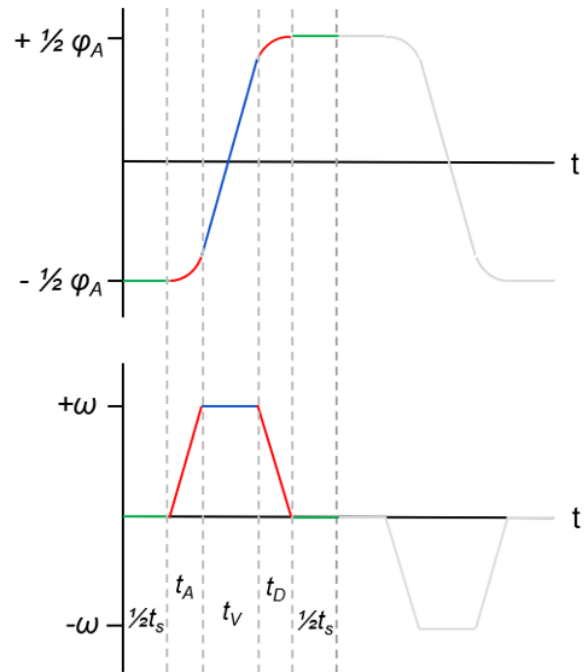


Figure D.1: Timing diagram of half a motor oscillation cycle. The time subscripts refer to time stopped (S), time accelerating (A), time moving at constant velocity (V) and time decelerating (D) within half a cycle.

In order to achieve full motion functionality, Q-Programming was used to supply the motors with the

correct position and timing values. MATLAB is used to load motor registers with the appropriate values that are then used within the same set of Q-Programs for each motor. It is important to note that motors contain different values within their registers depending on what motion they are set to run but have the exact same Q-Program set. In other words, Q-Programs act like internal functions that take in register variables and output a specific type of motion such as oscillations at specific amplitudes or frequencies, shaft rotation, and holding static shaft positions. Afterwards, a start Q-Program command is sent to all motors. Therefore, this method of pre-loading motors with the appropriate motion values to perform a variety of functions while leaving MATLAB open for data acquisition.

A description of all motor registers used in the current control system is given in Table D.1. Meanwhile, a full breakdown of Q-Program 1 is provided in Table D.2. Q-Program 1 contains all of the required commands to hold static shaft positions and dynamic motion cases such as rotations and oscillations. Other Q-Programs (2 and 3) are loaded into each motor but are omitted for brevity.

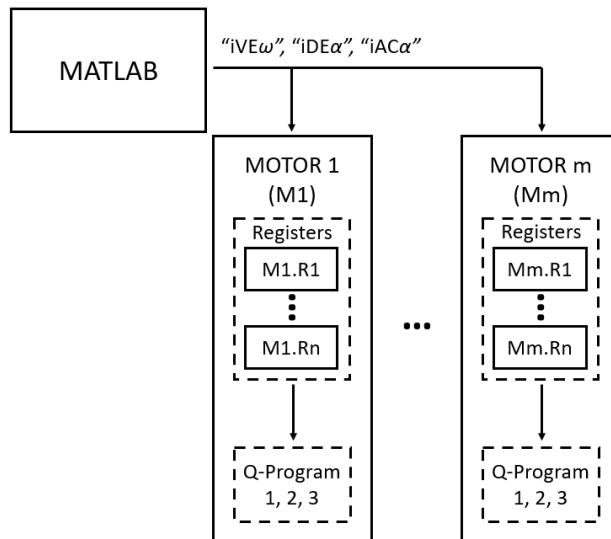


Figure D.2: Diagram of the MATLAB and motor interface. MATLAB is used to send angular velocity (VE), deceleration (DE), acceleration (AC) and other commands (timing and positioning) to each motor with addresses 1 to m. Each command is preceded by an address character,  $i = 1$  to m, indicating which motor to send the command. Each command is succeeded by its value (i.e.  $VE = \omega$ ,  $DE = AC = \alpha$ ). Each motor contains registers R1 to Rn in which data from MATLAB can be stored. Registers are then used as an input for each Q-Program.

Table D.1: Description of internal motor registers used for Q-programs.

Register #	Description (units)
1	Absolute position of $+1/2\phi_A$ (steps).
2	Absolute position of $-1/2\phi_A$ (steps).
3	Pause time related to $R_s$ and is equal to $1/2t_s$ (s).
4	Lag time before any motor action (s).
5	Amplitude ( $\phi_A$ ), rotation (360) or static pos. (0) ( $^\circ$ ).
6	Reserved register for Q-Program 2 (Homing function).
7	Reserved register for Q-Program 3 (Frequency scanning).
8	
9	

Table D.2: Full breakdown of Q-Program 1.

Line #	Label	CMD	Param. 1	Param. 2	Comment
1		TR	5	360	Check R5 and compare it to 360.
2		QJ	E	#LABEL1	If the previous line is equal (E) jump to LABEL1 (rotation case). Otherwise, continue to line 3.
3		TR	5	0	Check R5 and compare it to 0.
4		QJ	R	#LABEL2	If the previous line is equal (E) jump to LABEL2 (static position case). Otherwise, continue to line 5 (oscillation case).
5		WD	4		Wait for the lag time stored in R4.
6	LABEL3	WD	3		Wait for the stop time stored in R3 equal to $1/2t_s$ .
7		RM	2	D	Set the next move to the value in R2.
8		FP			Execute move.
9		WD	3		Wait for the stop time stored in R3 equal to $1/2t_s$ .
10		WD	3		Wait for the stop time stored in R3 equal to $1/2t_s$ .
11		RM	1	D	Set the next move to the value in R1.
12		FP			Execute move.
13		WD	3		Wait for the stop time stored in R3 equal to $1/2t_s$ .
14		QG	#LABEL3		Go back to LABEL 3 (start oscillation again).
15	LABEL2	QK			Kill/exit queue. Hold a static position.
16	LABEL1	WD	4		Wait for the lag time stored in R4.
17		CJ			Start rotation/Commence jog.